Investigation of Electron-Induced Radiation Damage to a TRISTAN Silicon Drift Detector

Master's Thesis

Verena Wallner

03713093

Course of studies:

Nuclear, Particle and Astrophysics

at

Technical University of Munich

Primary Reviewer:	Prof. Dr. Susanne Mertens
Secondary Reviewer:	Prof. Dr. Bastian Märkisch
Supervisor:	Dr. Korbinian Urban
	Dr. Daniel Siegmann

15 November 2024

Abstract

Sterile neutrinos are a theoretical type of neutrino that would naturally extend the Standard Model (SM) of particle physics. With a mass in the keV-scale, they are a promising candidate for Dark Matter (DM) and could help resolve open questions in neutrino physics and cosmology. Unlike active neutrinos, sterile neutrinos do not interact via the weak force, making them sterile. However, through a possible mixing with the active neutrino flavor, they would be nonetheless experimentally accessible. One possibility to measure sterile neutrinos is in single β-decay experiments, where the active-to-sterile mixing would cause a small, kink-like distortion in the electron energy spectrum.

Currently, the KArlsruhe TRItium Neutrino experiment (KATRIN) aims to directly measure the neutrino mass with unprecedented precision. To achieve this, the experiment focuses on the endpoint region of the electron spectrum from tritium β-decay, where the neutrino mass would be evident. Once the neutrino mass campaign is concluded, the experimental setup will be updated to search for sterile neutrinos with a targeted sensitivity on the parts-per-million (ppm) level. In contrast to the neutrino mass signature, the small imprint of the sterile neutrino could be located anywhere in the spectrum. Therefore, the entire spectrum needs to be scanned, leading to significantly higher electron rates at the detector. To meet the new requirements, the TRISTAN detector system is currently under development. It is designed to handle the envisioned high electron rate of 100 kcps while providing an excellent energy resolution of less than 300 eV (FWHM) at 20 keV. To achieve this, the TRISTAN detector features a modular, multi-pixel design based on Silicon Drift Detector (SDD) technology.

Although SDDs provide exceptional energy resolution, they were originally developed for X-ray spectroscopy, where interactions differ fundamentally from those in electron spectroscopy. Irradiating the detector with electrons leads to surface damage in the entrance window region, impacting the Charge Collection Efficiency (CCE) and thereby reducing energy resolution. However, maintaining high energy resolution throughout the entire sterile neutrino search with KATRIN is crucial for detecting the subtle imprint of sterile neutrinos. Therefore, the goal of this thesis was the investigation of electron-induced radiation damage to the TRISTAN SDDs to estimate its potential impact on the planned sterile neutrino search.

To understand the damage electrons can cause to the TRISTAN detector, one side of a detector module was irradiated with 15 keV electrons. In this irradiation, an exposure equivalent to about one year of sterile neutrino search was delivered within

a short time interval of less than ten hours. A dedicated experimental setup containing a custom-designed electron gun with steering coils and a copper plate for rate monitoring was developed. The irradiation was divided into five phases, with performance check measurements conducted before and after each phase to assess radiation damage as a function of electron exposure. It was investigated whether the electron and X-ray performance of the detector had changed and if the leakage current was increased.

The measurements revealed a degradation in electron performance, with energy resolution decreasing by $14\,\%$ for $15\,\mathrm{keV}$ electrons during the first irradiation phases. After an electron exposure equivalent to around four months of sterile neutrino search with KATRIN ($\approx 1.13 \cdot 10^{12}$ electrons), a saturation of the damage was found. The observed spectral features are characteristic of surface damage and appeared consistently across all irradiated pixels. While the electron performance was degraded, the X-ray performance remained unaffected, confirming that the damage is limited to the detector surface. Additionally, no increase in leakage current was found for a cooled detector to $-35\,^\circ\mathrm{C}$. All these findings regarding the detector performance after irradiation align well with the theoretical expectations.

Finally, a stability analysis regarding the possible recovery of the damage was conducted. Here, the effect of heating the detector to $37\,^\circ\mathrm{C}$ overnight and leaving the detector to rest for two months was investigated. Both approaches did not significantly recover the damage, suggesting that the damage stays stable for the given conditions in the sterile neutrino search with KATRIN. This again aligns well with the theoretical expectation of the physical cause and impact of electron-induced radiation damage to an SDD.

Contents

1. Neutrino Physics

In 1930, Wolfgang Pauli postulated a new particle, later called the neutrino, as a possible explanation for the observed continuous β-decay spectrum [1]. At that time, physicists were investigating the energy of an electron released in a radioactive β-decay where a neutron is converted into a proton and an electron. Since this decay would underly the kinematics of a two-body decay, they expected to detect mono-energetic electrons. Against their expectation, the measurements showed a continuous electron energy spectrum ranging from zero kinetic energy to nearly the maximum possible energy. Pauli recognized that the laws of conservation of energy and momentum are only fulfilled in radioactive β-decay if there is also a third particle created, which common particle detectors could not see at that time. This way, the electron would need to share the energy released in the decay with this third particle, leading to a continuous electron energy spectrum and solving the puzzle. This new particle, the neutrino, would need to be electrically neutral to preserve charge conservation, have a spin of $1/2$ to maintain angular momentum conservation, and be very light, as the highest energy observed for the beta electron nearly matched the theoretical energy limit.

This chapter gives an introduction to neutrino physics, starting with the neutrino's properties in the Standard Model of particle physics (SM) in Section 1.1, followed by their final discovery in 1956 in chapter 1.2. Interesting behavior of the neutrinos, like neutrino oscillations, are questioning their SM properties and are discussed in Section 1.3. The impact of neutrino oscillation on the neutrino's mass is discussed in Section 1.4. Finally, in Section 1.5, the possible existence of a sterile neutrino, which is of particular interest for the work presented in this thesis, will be introduced.

1.1. Neutrinos in the Standard Model

Neutrinos are electrically neutral fermions with spin $1/2$ and come in three different flavors (ν_e, ν_μ and ν_τ) according to their charged leptonic partners: electron, muon, and tau. In the SM, neutrinos play a unique role since they solely interact through weak interaction which only couples to left-handed particles. Hence, a possible right-handed version of the electrically neutral neutrinos would not interact via any SM interaction. Therefore, and since only left-handed neutrinos were detected to this point, the neutrino was introduced in the SM solely left-handed, laking a right-handed counterpart.

Another interesting property of the neutrino is its mass. In the SM, the mass generation of a particle via Yukawa coupling with the Higgs field is only possible with a right-handed partner. Therefore, the neutrino was introduced as massless in the SM.

New insights regarding the behavior of neutrinos, such as neutrino oscillation, conflict with a massless neutrino and will be discussed in Section 1.3 and 1.4.

1.2. The Discovery of Neutrinos

Twenty-six years after the postulation of the neutrino by Wolfgang Pauli, it was finally discovered by Frederick Reines and Clyde Cowan in the project Poltergeist [2]. They used the Savannah River Power Plant in South Carolina as a strong source of electron antineutrinos $\bar{\nu}_e$. The idea was to detect those neutrinos indirectly via inverse β-decay where an electron antineutrino induces the decay of a proton p into a neutron n and a positron e^+:

$$\bar{\nu}_e + p \rightarrow n + e^+. \tag{1.1}$$

Large water tanks with dissolved cadmium chloride ($CdCl_2$) in front of the power plant served as target material. This way, neutrinos can be detected by observing the decay products, the neutron and positron, using scintillators. The characteristic signal of two photons from electron-positron annihilation, followed by another photon a few microseconds later originating from the capture of the neutron on the cadmium, proved the existence of the electron antineutrino.

As mentioned in Section 1.1, there are also two other neutrino flavors in addition to the electron neutrino. L. Lederman, M. Schwarz and J. Steinberger found the muon neutrino ν_μ in 1962 at the Alternating Gradient Synchrotron (AGS) neutrino experiment at Brookhaven National Laboratory (BNL) [3]. A proton beam was shot onto a beryllium target, producing charged pions. When those pions decay, neutrinos are produced. A steel shield stopped all particles in front of the detector, a spark chamber, except for the neutrinos, due to their very low interaction rate. Those neutrinos interact with the atoms in the spark chamber, creating muons that leave long muon tracks in the detector. At the same time, nearly no electron signals were found. This proved the existence of a second neutrino flavor ν_μ.

The third neutrino flavor ν_τ was found in 2001 by the Direct Observation of Nu Tau (DONUT) experiment at Fermilab [4]. The measurement principle was similar, again using an accelerated proton beam producing charmed mesons, which decay into tau neutrinos. By stopping all particles but the neutrino, a characteristic kink-like signal could be observed originating from the short lifetime of the tau produced by a tau neutrino after the shielding. With this, all three neutrino flavors were found. Those three neutrinos are considered as the completion of the leptonic part of the SM as studies of the decay width of the Z boson at the Large Electron-Positron (LEP) collider limit the total number of light active neutrinos to $N = 2.9840 \pm 0.0082$ [5].

1.3. Neutrino Oscillations

In the 1960s, the Homestake experiment by Ray Davis observed a deficit of a factor of three in the electron neutrino flux coming from the sun with respect to predictions. In the following years, several other experiments like GALLEX [6], GNO [7], SAGE [8], and Borexino [9] confirmed this discrepancy, reducing the likelihood of a measurement error and increasingly pointing towards the need for physics beyond the SM.

A possible solution was proposed in 1957 by Pontecorvo: neutrino oscillations [10]. The idea is that neutrinos can change their flavor eigenstate, meaning the missing electron neutrinos in the Homestake experiment have oscillated into muon and tau neutrinos on their way to Earth, leading to a deficit in the electron neutrino flux. The theory states that the three flavor eigenstates (ν_e, ν_μ, ν_τ) are a superposition of three mass eigenstates (ν_1, ν_2, ν_3). In this picture, neutrinos propagate in a quantum-mechanical superposition of mass eigenstates but interact in flavor eigenstates. Both states are related via the Pontecorvo-Maki-Nakagawa-Sakata (PMNS) matrix:

$$\begin{pmatrix} \nu_e \\ \nu_\mu \\ \nu_\tau \end{pmatrix} = \begin{pmatrix} U_{e1} & U_{e2} & U_{e3} \\ U_{\mu1} & U_{\mu2} & U_{\mu3} \\ U_{\tau1} & U_{\tau2} & U_{\tau3} \end{pmatrix} \begin{pmatrix} \nu_1 \\ \nu_2 \\ \nu_3 \end{pmatrix} \tag{1.2}$$

The PMNS matrix for three neutrinos can be parameterized with three mixing angles (Θ_{12}, Θ_{13}, Θ_{23}), which determine the mixing amplitudes, and a Charge conjugation Parity (CP) violating complex Dirac phase δ_{CP}. If neutrinos are Majorana particles, two additional Majorana phases α and β are introduced. In the simplified case of only two neutrinos, the oscillation probability of one neutrino ν_a into a different flavored neutrino ν_b is described by [11]:

$$P(\nu_a \rightarrow \nu_b) = \sin^2(2\theta) \sin^2\left(\frac{L}{4E} \Delta m^2 \right). \tag{1.3}$$

Thus, the oscillation probability depends on the mixing angle θ, the propagation length L, the energy E, and the difference of the squared masses $\Delta m^2 = m_1^2 - m_2^2$. Equation 1.3 shows that if neutrinos were massless, their oscillation probability would be zero. Therefore, for a non-vanishing oscillation probability, at least two of the three neutrinos must have a non-zero mass. Nevertheless, neutrino oscillations were observed, as described above, in reactor, atmospheric and accelerator experiments. Therefore, neutrino oscillations give rise to physics beyond the SM in the form of a massive neutrino. However, neutrino oscillation experiments cannot determine the absolute masses of the neutrinos but only the mass squared difference Δm^2. Since the neutrino's absolute mass is a vibrant research topic, several exper-

iments have been conducted to determine the absolute mass of the neutrino. They will be discussed in the following section.

1.4. Neutrino Mass

The observation of neutrino oscillations demonstrates that neutrinos cannot be massless. Despite numerous experiments aimed at measuring the absolute neutrino mass, to this date, no experiment has succeeded. In general, there are three different experimental approaches to set an upper limit to the absolute neutrino mass: cosmological observations, neutrinoless double β-decay, and the kinematics of β-decay.

Cosmological Observations

In cosmology, the absolute mass of neutrinos can be deduced by observing their impact on the evolution of the universe. Neutrinos, being light and abundant, contribute to the cosmological matter density determining the formation of small-scale and large-scale structures in the universe. Since neutrinos were relativistic for a large period in the early universe, a non-zero neutrino mass rather suppresses the growth of cosmic structures on small scales. Observing the structure of the universe via the cosmic microwave background (CMB), galaxy surveys, or the Lyman-alpha forest, an upper limit on the sum of the neutrino masses can be inferred. The current best limit by the Planck collaboration is [12]

$$m_\nu = \sum_i m_i < 0.11 \text{ eV (95\% C.L.)} \tag{1.4}$$

However, this result highly depends on the underlying cosmological model.

Neutrinoless Double β-decay

Less model dependency can be achieved by observing neutrinoless double β-decay ($0\nu\beta\beta$). This hypothetical process could occur if neutrinos are Majorana particles, meaning they are their own antiparticles [13]. In this process, two neutrons would simultaneously decay into two protons and two electrons without emitting any neutrinos, violating lepton number conservation by two units. The experimental signature of $0\nu\beta\beta$ is a mono-energetic peak at the kinematic endpoint of the corresponding continuous ordinary two neutrino double β-decay ($2\nu\beta\beta$). The $0\nu\beta\beta$ has not yet been observed. The observation of $0\nu\beta\beta$ would not only confirm the Majorana nature of neutrinos but also provide a measurement of the coherent superposition of neutrino mass eigenstates $m_{\beta\beta}$

$$m_{\beta\beta}^2 = \left| \sum_i U_{ei}^2 m_i \right|^2. \tag{1.5}$$

This is because the half-life $T_{1/2}^{0\nu}$ of this process depends on $m_{\beta\beta}$. The current best upper limit was achieved by the KamLAND-Zen experiment which found a decay half-life of $T_{1/2}^{0\nu} > 2.3 \cdot 10^{26}$ y corresponding to an effective neutrino mass of $m_{\beta\beta} < 36 - 156$ meV [14]. However, this method relies on the assumption that neutrinos are indeed Majorana particles, and it can only provide a limit range since $m_{\beta\beta}$ depends on the underlying calculation of the nuclear matrix element, which carries significant theoretical uncertainties.

Single β-decay

The most model-independent approach to measure the effective neutrino mass is via single β-decay. These experiments focus on the precise measurement of the energy spectrum of electrons emitted in β-decay processes, such as the decay of tritium. Near the endpoint of the electron energy spectrum, the presence of a non-zero neutrino mass causes a slight distortion that can be used to infer the neutrino mass. This is because the electron needs to share the available energy with the neutrino; if the neutrino has a non-zero mass, the spectrum shifts towards lower energies. Figure 1.1 shows an example of the influence of different neutrino masses on the endpoint of the differential tritium spectrum. Single β-decay experiments directly probe the neutrino mass without relying on specific theoretical models, but they are extremely challenging due to the very small mass differences that need to be detected. The current resolution of such experiments is not yet precise enough to resolve all three mass eigenstates. Therefore, the effective neutrino mass m_β which is the incoherent sum of the neutrino mass eigenstates is introduced:

$$m_\beta = \sqrt{\sum_i m_i^2 |U_{ei}|^2}. \tag{1.6}$$

The KArlsruhe TRItium Neutrino experiment (KATRIN) is currently the leading effort in this field, aiming to determine the neutrino mass with high precision by examining the endpoint region of tritium β-decay. The current upper limit is $m_\beta < 0.45$ eV at 90 % C.L. [15]. A detailed description of KATRIN is provided in section 2.

1.5. Sterile Neutrinos

Sterile neutrinos ν_s are a hypothesized type of neutrino that differs from the three known neutrino flavors ν_e, ν_μ and ν_τ. In the following, these three usual neutrino flavors will be called active neutrinos. Those active neutrinos appear in the SM only as left-handed, while there is no strong reason why they should not also have a right-handed partner like every other lepton. Hence, introducing a right-handed neutrino would be a natural extension of the SM. The only force neutrinos interact with is
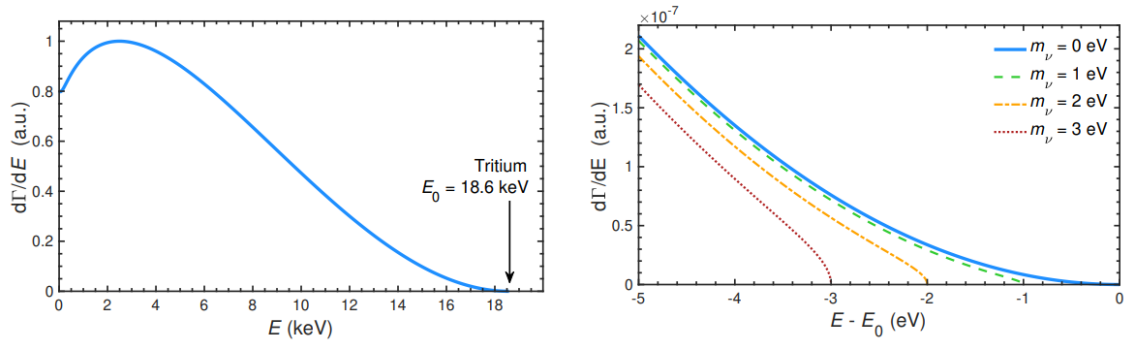
Figure 1.1: **Tritium β-Decay Spectrum and Endpoint Region**
Left: Tritium β-decay spectrum with the endpoint energy $E_0 = 18.6\,\text{keV}$.
Right: Zoom into the endpoint region where a non-zero neutrino mass causes a shift towards lower energies and a shape distortion of the spectrum. The effect is shown for different effective masses m_ν. Plot taken from [16].

the weak interaction which couples only to left-handed particles. Therefore, there would be no SM interaction for the right-handed neutrinos, which gives them the "sterile" designation. Nevertheless, there is the possibility that sterile neutrinos ν_s mix with active neutrinos through their mass eigenstate ν_4 which can be described by extending the PMNS matrix to:

$$
\begin{pmatrix} \nu_e \\ \nu_\mu \\ \nu_\tau \\ \nu_s \end{pmatrix} = \begin{pmatrix} U_{e1} & U_{e2} & U_{e3} & U_{e4} \\ U_{\mu 1} & U_{\mu 2} & U_{\mu 3} & U_{\mu 4} \\ U_{\tau 1} & U_{\tau 2} & U_{\tau 3} & U_{\tau 4} \\ U_{s1} & U_{s2} & U_{s3} & U_{s4} \end{pmatrix} \begin{pmatrix} \nu_1 \\ \nu_2 \\ \nu_3 \\ \nu_4 \end{pmatrix}
\tag{1.7}
$$

This mixing would make it possible to detect signatures of sterile neutrinos in active neutrino experiments.

In addition to being a very natural extension of the SM, sterile neutrinos are also motivated by several theoretical and experimental considerations:

See Saw Mechanism

The introduction of right-handed neutrinos offers, for example, a framework for understanding the mass generation of active neutrinos and additionally provides a potential explanation for their exceptionally small masses. In the Standard Model, active neutrinos are many orders of magnitude lighter than other fermions, with no clear reason for this disparity. Including a right-handed neutrino enables the implementation of the so-called See-Saw mechanism. The mechanism gets its name from the idea of a "see-saw," where the smallness of one quantity is balanced by the largeness of another. More precisely, the smallness of the active neutrino mass could be explained by a GeV-scale and, thereby, a rather heavy, sterile neutrino. A condition for the mechanism is that the neutrino is a Majorana particle. Then,

the right-handed neutrinos can have a very large Majorana mass M_R, which is not constrained by the Higgs mechanism that gives mass to other particles. The mass term for neutrinos in this extended model can be written as

$$\mathcal{M} = \begin{pmatrix} 0 & m_D \\ m_D & M_R \end{pmatrix} \tag{1.8}$$

where m_D is the Dirac mass term generated by the usual Higgs mechanism. The eigenvalues of the mass matrix $\mathcal{M}$ give the masses of the physical neutrino states m_ν and m_N, and we obtain

$$m_\nu \approx \frac{m_D^2}{M_R}, \quad m_N \approx M_R. \tag{1.9}$$

If we assume M_R to be in the order of GeV or higher, the light neutrino mass m_ν naturally becomes very small.

Experimental Anomalies

There have been several experimental anomalies that suggest the possible existence of sterile neutrinos. For instance, short-baseline neutrino oscillation experiments like the Liquid Scintillator Neutrino Detector (LSND) [17] and the Mini Booster Neutrino Experiment (MiniBooNE) [18] observed excess events that could be explained by the presence of a light sterile neutrino with a mass in the eV-scale. Additionally, the Gallium Experiment (GALLEX) [19] and the Soviet-American Gallium Experiment (SAGE) [20] found anomalies in their calibration process. Both experiments aim to measure the solar neutrino flux using inverse β-decay in ^{71}Ga. When calibrating their experiments using strong ^{51}Cr and ^{51}Ar electron neutrino sources, they measured a decreased rate which could be explained by a light sterile neutrino in the eV-range. However, despite these hints, the existence of eV-scale sterile neutrinos remains controversial. Other experiments, such as the KATRIN experiment, can directly search for a sterile neutrino in the eV-scale, but until now, no sterile neutrino signal has been observed.

Dark Matter Candidate

Finally, if the sterile neutrino would be in the keV-mass range, it is a suitable candidate for Dark Matter (DM). They are neutral, massive, and, provided the active-sterile mixing angle is sufficiently small, they also have a lifetime longer than the age of the universe. DM is typically categorized into three types: hot dark matter (HDM), cold dark matter (CDM), and intermediate warm dark matter (WDM), based on the particles' velocities and the time of their creation. Depending on their creation mechanism, keV-scale sterile neutrinos would belong to CDM or WDM [21]. In both cases, sterile neutrinos could explain cosmological observations.

Since sterile neutrinos couple to active neutrinos, there is a decay mode where a sterile neutrino decays into an active neutrino by emitting a mono-energetic photon. Therefore, sterile neutrino DM leads to potentially observable X-ray emission. Hints for such a decay have been found by the X-ray Multi-Mirror (XMM)-Newton telescope [22]. In 2014, the telescope found an unidentified X-ray line near 3.55 keV, which could, in principle, originate from a radiative decay of a 7 keV sterile neutrino. However, the current resolution of X-ray telescopes is not yet sufficient to conclusively rule out alternative explanations for this line, such as atomic physics effects.

The above-mentioned motivations for the sterile neutrino show that depending on the mass range of the sterile neutrino, it could solve numerous open questions from particle physics and astronomy. The most important mass range for this thesis is the keV sterile neutrino. This mass range can be directly probed by the KATRIN experiment with the new detector update TRISTAN. Using tritium β-decay allows probing the sterile neutrino parameter space up to 18.6 keV and mixing amplitudes of $\sin^2\Theta < 10^{-6}$ [23].

2. The KATRIN Experiment

The KArlsruhe TRItium Neutrino experiment (KATRIN) is a single β-decay neutrino mass experiment. It can directly probe the effective electron antineutrino mass using molecular tritium (cf. Equation 2.1).

$$T_2 \rightarrow{}^3 HeT^+ + e^- + \bar{\nu}_e. \tag{2.1}$$

KATRIN holds the current best upper limit on the neutrino mass in direct neutrino mass experiments of $m_\beta < 0.45\,eV$ at $90\,\%$ C.L. [15] and aims to improve this limit even to a sensitivity close to $0.2\,eV$ with $90\,\%$ C. L. [24]. The signature of a massive neutrino in single β-decay experiments is a local spectral distortion as described in Section 1.4. This distortion is statistically significant only in a region close to the spectral endpoint. Therefore, solely a narrow region close to the endpoint is analyzed. Only a fraction of $2 \cdot 10^{-13}$ falls into the last $1\,eV$ below the endpoint, demanding high source strength to ensure adequate statistics [24]. Tritium is particularly advantageous for neutrino mass investigations due to its low kinematic endpoint energy of $E_0 = 18.6\,keV$ and short half-life of $t_{1/2} = 12.3\,a$ [23]. These characteristics enhance the fraction of β-decay in the endpoint region. To achieve its goal of a high neutrino mass sensitivity, KATRIN combines a high luminosity Windowless Gaseous Tritium Source (WGTS) with a high precision electron spectrometer based on Magnetic Adiabatic Collimation combined with an Electrostatic filter (MAC-E).

In the following, an overview of the experimental setup of KATRIN will be provided in Section 2.1. The neutrino mass measurement campaign of KATRIN is succeeded by the search for sterile neutrinos in the keV-mass range with the KATRIN experimental setup that will be discussed in Section 2.2.

2.1. Experimental Setup of KATRIN

Figure 2.1 shows the $70\,m$-long KATRIN beamline divided into six components. The most important parts will be discussed in the following based on the KATRIN design report [24].

Windowless Gaseous Tritium Source (WGTS)

The Windowless Gaseous Tritium Source (WGTS) acts as the β-electron source of KATRIN and offers high luminosity (tritium decay rate: $1.7 \cdot 10^{11}\,Bq$) and small systematic uncertainties ($\pm 1\,\%$). It consists of a $10\,m$-long stainless steel tube with a diameter of $9\,cm$. The molecular tritium gas is continuously injected in the center and streams towards both sides. Superconducting magnets guide the electrons
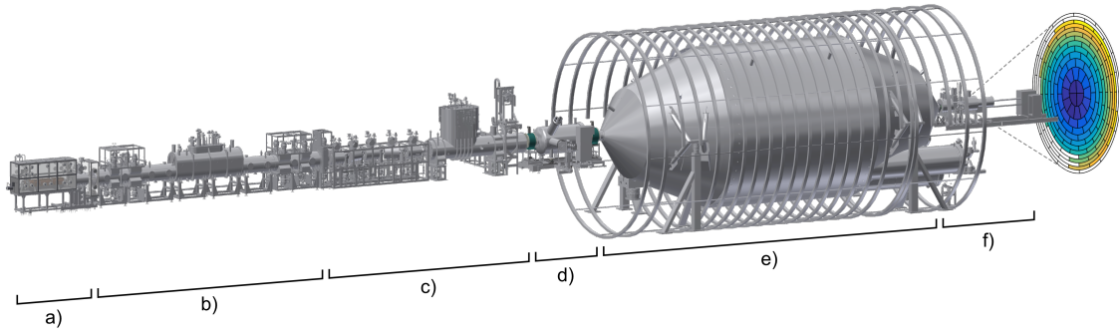
Figure 2.1: **Schematic Overview of KATRIN**
The KATRIN experimental setup consists of the following sections:
a) Rear section, b) Windowless Gaseous Tritium Source (WGTS), c) Transport section, d) Pre-spectrometer, e) Main-spectrometer, f) Focal Plane Detector (FPD). Figure taken from [25]

emitted in the β-decay of the tritium molecules along the beam tube towards the transport section. A closed-loop system ensures that the 40 g/d tritium throughput stays at a purity of more than 95 %.

Transport Section

The transport section connects the WGTS with the spectrometer section and is designed to solely transport the β-electrons. To prevent tritium from entering the spectrometer and detector sections, where it would increase the background, the transport section is built in a chicane configuration, eliminating any direct line of sight from the tritium source to the detector. The transport section is divided into the Differential Pumping Section (DPS) and the Cryogenic Pumping Section (CPS). The DPS uses four turbo-molecular pumps to reduce the tritium flow by five orders of magnitude. The CPS traps the remaining tritium on an argon frost layer at temperatures below 4 K, reducing tritium levels by an additional nine orders of magnitude. Combined, these sections decrease the tritium flux by over 14 orders of magnitude. Throughout this process, β-electrons are magnetically guided to the spectrometer without energy loss, ensuring accurate measurements.

Spectrometer Section

The spectrometer section consists of the pre-spectrometer and the main-spectrometer. Both are based on the MAC-E filter principle which is depicted in Figure 2.2. Superconducting magnets at the front and rear end of the spectrometer vessel create a magnetic field that guides the electrons from the source magnetic field B_{src} to the maximum magnetic field B_{max}. The electrons perform cyclotronic motion caused by the Lorentz force along the field lines. At the analyzing plane, the magnetic field drops by four orders of magnitude to a minimum B_{min}. At the same time, a retarding potential is applied, which finds its maximum at the analyzing plane.
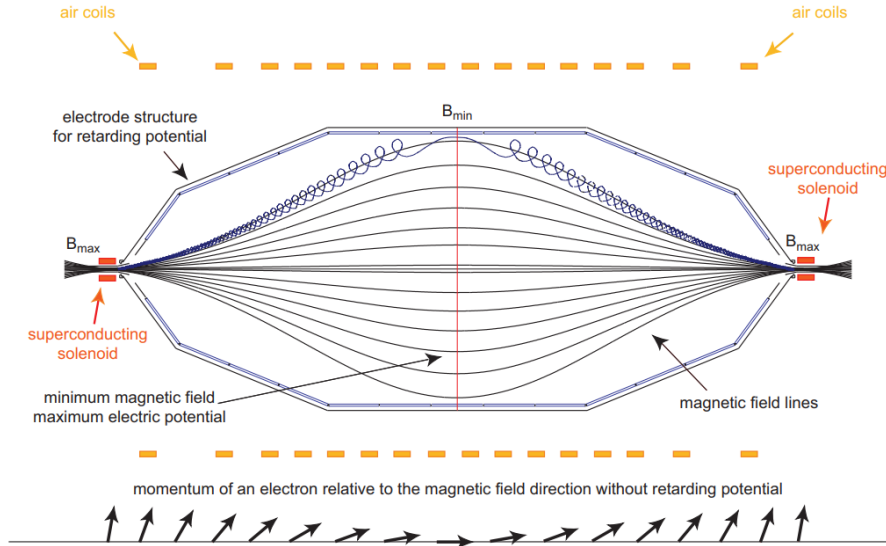
10

Figure 2.2: **Schematic Drawing of the KATRIN Main-Spectrometer**
The main-spectrometer is based on the MAC-E filter principle. Electrons (blue trajectory) are guided in cyclotron motion along the field lines (black) inside the vessel. The magnetic field is high at the front and rear end, while it becomes minimal at the analyzing plane (red line). This allows for magnetic adiabatic transformation of the electron's transverse momentum into a longitudinal momentum (black arrows on the bottom). At the analyzing plane, a retarding electric potential qU is applied, which acts as an electrostatic barrier for electrons with energies below qU. Figure taken from [26].

With this, the spectrometer acts as a high-pass filter. Only electrons with an energy higher than the retarding potential U can overcome this electrostatic barrier and are re-accelerated and collimated onto a detector. If the energy of the electron is insufficient to overcome the barrier, it is reflected.

The special magnetic field configuration of a high magnetic field at the front and rear end and a low magnetic field at the analyzing plane is needed to ensure high sensitivity. This is because the retarding potential is applied perpendicular to the direction of the magnetic field guiding the electrons. Therefore, the filter is only sensitive to the longitudinal component $E_\parallel$ of the electron energy $E = E_\parallel + E_\perp$ and its sensitivity is defined by the remaining transversal component $E_\perp$. Minimizing $E_\perp$ is achieved by magnetic adiabatic collimation: The transversal momentum $p_\perp$ of the electron is adiabatically transformed into a longitudinal one, keeping the electron magnetic moment μ constant:

$$\mu = \frac{E_\perp}{B} \propto \frac{p_\perp^2}{B} = \text{const.} \tag{2.2}$$

This leads to an energy resolution ΔE of the spectrometer depending on the remaining $E_\perp$, i.e. the fraction of B_{min} to B_{max}:

$$\Delta E = E \cdot \frac{B_{\mathrm{min}}}{B_{\mathrm{max}}} \, . \tag{2.3}$$

This way, the KATRIN main-spectrometer achieves a design spectrometer resolution of $\Delta E = 0.93\,\mathrm{eV}$ Full Width at Half Maximum (FWHM) with $E = 18.574\,\mathrm{keV}$, $B_{\mathrm{min}} = 3 \cdot 10^{-4}\,\mathrm{T}$, and $B_{\mathrm{max}} = 6\,\mathrm{T}$. The β-spectrum near the endpoint is achieved by measuring the rate of electrons reaching the FPD for different retarding energies eU, leading to an integral spectrum according to

$$\Gamma(eU, m_\beta) = \int_{eU}^{E_0} dE \frac{d\Gamma(eU, m_\beta)}{dE} \, . \tag{2.4}$$

In front of the main-spectrometer, there is a smaller pre-spectrometer based on the same principle. The main purpose of this pre-spectrometer is to reject most of the low-energy electrons. This way, only the relevant electrons with energies close to the endpoint enter the main-spectrometer. However, the combination of both spectrometers leads to a Penning trap between them. Therefore, the pre-spectrometer was switched off after the fourth measurement campaign [27].

Focal Plane Detector (FPD)

Those electrons that overcome the potential barrier of the main-spectrometer are accelerated onto the Focal Plane Detector, where they are counted. The acceleration with additional $10\,\mathrm{kV}$ leads to a lower intrinsic detector background in the region of interest. The detector consists of a silicon PIN (positive-intrinsic-negative) diode segmented into 148 pixels of equal area. The segments are arranged in a ring-wise structure, allowing the investigation of radial and azimuthal effects. Since the detector is designed to only count the electrons, an energy resolution of about $1.5\,\mathrm{keV}$ (FWHM) at $18.6\,\mathrm{keV}$ is sufficient. Furthermore, for neutrino mass analysis, only electrons near the endpoint are of interest where the flux is rather low. Therefore, the detector can handle count rates in the order of tens of kcps [28].

2.2. keV-scale Sterile Neutrino Search with KATRIN

The KATRIN experimental setup, as described above, was designed to measure an integral tritium spectrum near the endpoint to search for distortions caused by a non-zero neutrino mass. Besides the neutrino mass search, the measured β-decay spectrum can be analyzed regarding an imprint of hypothetical sterile neutrinos. If a sterile neutrino exists, the resulting tritium spectrum would be a superposition of

active neutrino and sterile neutrino components:

$$\frac{d\Gamma}{dE} = \underbrace{\cos^2 \theta_s \frac{d\Gamma(m_\beta)}{dE}}_{\text{Active Term}} + \underbrace{\sin^2 \theta_s \frac{d\Gamma(m_4)}{dE}}_{\text{Sterile Term}} . \qquad (2.5)$$

This would manifest itself as a kink-like signature and a broad distortion in the spectrum depending on the mixing angle θ_s, the effective electron anti-neutrino mass m_β, and the fourth mass eigenstate m_4. Figure 2.3 depicts an exemplary sterile neutrino signal in the tritium spectrum. The position of the kink depends on the mass of the sterile neutrino (here: $m_4 = 10 \, \text{keV}$) and the mixing angle determines the strength of the distortion of the spectrum.
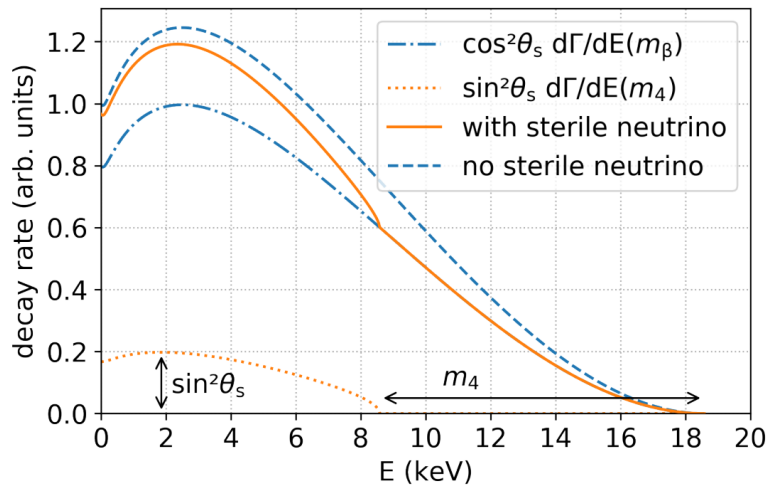
Figure 2.3: **Tritium β-Decay Spectrum with Sterile Neutrino Imprint**
The measured spectrum including the sterile neutrino imprint (orange line) is a superposition of the active (blue dash-dotted line) and sterile neutrino (orange dotted line) part. Here, the generated sterile neutrino has a mass of $m_4 = 10 \, \text{keV}$ and an exaggerated large mixing amplitude $\sin^2(\theta_s) = 0.2$. For comparison, the blue dashed line shows the spectrum for the case where no sterile neutrino exists. Figure taken from [29].

During the commissioning phase of KATRIN in 2018, the collaboration was able to set an exclusion limit on the sterile-to-active mixing amplitude for sterile neutrinos with a mass up to $1.6 \, \text{keV}$. The new limit of $\sin^2(\theta_s) < 5 \cdot 10^{-4}$ (95% C.L) improved current laboratory-based bounds in the sterile-neutrino mass range between 0.1 and $1.0 \, \text{keV}$ [30].

Since the mass of the sterile neutrino is unknown, the kink-like signature of a sterile neutrino could be located anywhere in the spectrum. Therefore, scanning the entire spectrum would allow searching for sterile neutrinos up to $18.6 \, \text{keV}$ and mixing angles $\sin^2(\theta_s) < 10^{-6}$ [23]. To scan the entire spectrum, the retarding potential will be set to significantly lower values or zero leading to much higher count rates up to 10^8 cps [23]. The KATRIN FPD is not designed to handle these high count rates

and is planned to be replaced after the neutrino mass campaign is finished. A novel multi-pixel silicon drift detector array named TRISTAN is currently under development and will be described in Section 3. The energy resolution of the TRISTAN detector is targeted to be less than 300 eV FWHM for 20 keV electrons to be able to resolve a distortion in the ppm-level [31]. With this, measuring differential spectra becomes possible in addition to the integral spectrum. Consequently, a potential positive signal on a sterile neutrino can be verified independently.

3. The TRISTAN Detector

The TRISTAN detector is based on the Silicon Drift Detector (SDD) technology. Those semiconductor detectors are well suited for the keV sterile neutrino search with KATRIN due to their good energy resolution at high count rates in the keV range. This chapter gives an overview of the working principle of the TRISTAN detector. It starts with an introduction to semiconductor detectors in Section 3.1, followed by the working principle of SDDs in Section 3.2. In Section 3.3 and 3.4, the design of the TRISTAN detector and its response to electrons is presented, respectively.

3.1. Semiconductor Detectors

The valence band is the highest occupied energy level inside a solid, whereas the conduction band is the lowest unoccupied energy level. In conductor materials, the valence and conduction band overlap so that electrons can move freely. In contrast, insulators have a large energy gap, known as the band gap, between the two bands, which prevents electrons from moving between them. In semiconductors, this band gap is small enough to lift a valence electron into the conduction band if it gains enough thermal energy. Figure 3.1 illustrates the band structure for all three materials. The conductivity of semiconductors is temperature-dependent. At $T = 0\,\mathrm{K}$, the conduction band is empty, and the semiconductor acts as an insulator. Increasing the temperature increases a valence electron's probability of gaining enough energy to overcome the band gap and be excited into the conduction band.
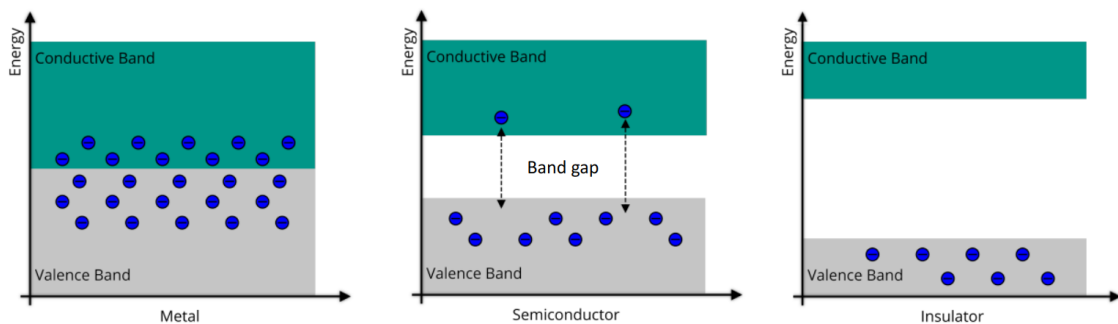

Figure 3.1: **Band Structure for Metals, Semiconductors and Insulators**
Metals have no band gap, allowing the electrons to move freely between valence and conductive band. In semiconductors the band gap is small enough so that some electrons can be excited into the conductive band. Insulators have a large band gap that electrons can not overcome. Figure adapted from [32].

The TRISTAN detector uses silicon as semiconductor material. The band gap of silicon is rather low with $E_g = 1.12\,\mathrm{eV}$ at room temperature $T = 300\,\mathrm{K}$ [33]. As a result, many electron-hole pairs are created when energy is deposited in the material which leads to a good energy resolution.
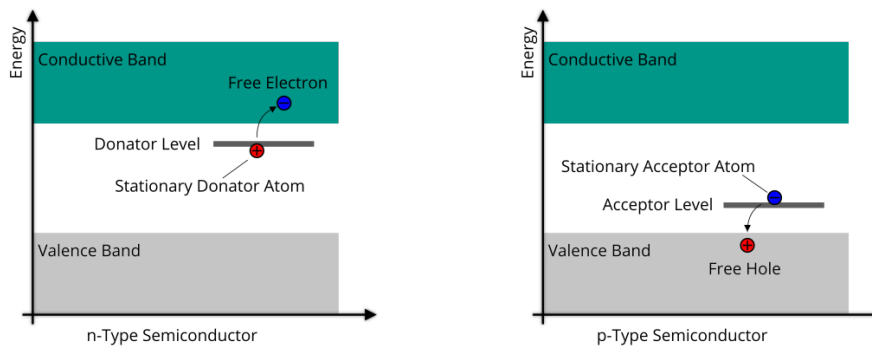
Figure 3.2: **Band Structure for Doped Semiconductors**
Left: Band structure of a n-type doped semiconductor. An additional energy level is created close to the conduction band, and a free electron is donated to the conduction band.
Right: Band structure of a p-type doped semiconductor. An additional energy level is created close to the valence band, and a free hole is added to the valence band. Figure taken from [32].

Additionally, the conductivity can be modified by a process called doping as illustrated in Figure 3.2. Doping means placing small fractions of other materials into the crystal structure of the semiconductor. This adds additional states in the forbidden energy region of the band gap between the valence and conduction band, acting as stepping stones for electrons to overcome the barrier. There are two kinds of doping: n-type and p-type doping. N-type doping adds additional energy levels very close to the conduction band. In silicon (four valence electrons), this is most commonly realized by doping with phosphorus (five valence electrons), which acts as an electron donor. Since the phosphorus will only be bound with four of its five valence electrons to the silicon, it donates its fifth valence electron. This fifth electron acts as a free charge carrier and requires much lower energy to be excited into the conduction band than electrons that cause the intrinsic conductivity of silicon. Complementary, p-type doping introduces energy levels very close to the valence band. A typical p-type dopant is boron (three valence electrons), which acts as an electron acceptor. Similar to the free electrons through n-type doping, it creates free holes in the valence band. In both cases, the created free charge carriers increase the conductivity of the semiconductor. [34]

The principle of doping can be exploited to produce a so-called p-n junction. This effect was discovered in 1940 by Russell and is the underlying principle of semiconductor detectors [35]. A p-n junction is obtained if a p-type material is brought together with a n-type material. In the interface region, there are no free charge carriers since the free electrons of the n-doped area will recombine with the free holes of the p-doped area. Therefore, a so-called depletion zone is obtained. When the surplus charge carriers move to the oppositely doped region to recombine, fixed-
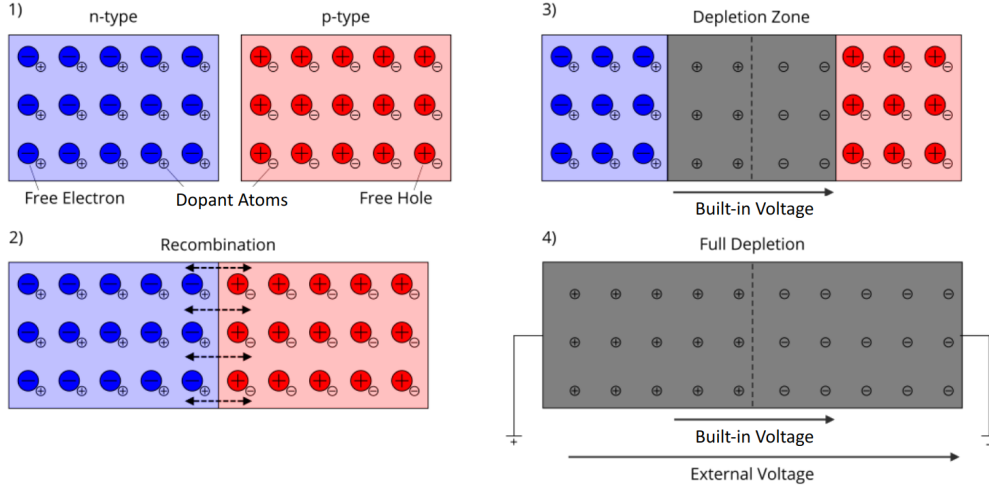
Figure 3.3: **Reverse Bias P-N Junction**
Picture 1) shows a n-doped and a p-doped semiconductor. The dopant atoms with their remaining charge are depicted with small symbols and their free charge carriers with the larger symbols. In picture 2), the two materials are brought together so that the free electrons from the n-doped area recombine with the free holes of the p-doped area. This creates a depletion zone which is illustrated in gray in picture 3). The remaining charged dopant atoms build up a voltage called built-in voltage. Applying an additional external current in the same direction as the built-in voltage further increases the depletion zone, as shown in picture 4). Figure adapted from [32].

charged dopant atoms are left behind. This results in a voltage difference between the two regions called the diffusion voltage U_{diff}. The more charge carriers recombine, the greater the depletion zone. With this, also U_{diff} increases until the voltage difference brings the recombination to a halt. The depleted volume can be further increased by applying an additional external voltage U_{bias} in the same direction as U_{diff}. This is called a reverse bias p-n junction. Figure 3.3 illustrates the process of creating a reverse bias p-n junction. The p-n junction acts as a diode since it allows electric current in one direction and blocks it in the opposite direction.

A p-n junction can be used to detect particles. When incoming particles interact within the depleted volume of the doped semiconductor, a charge cloud of electron-hole pairs is created. In the picture of the band structure, valence electrons are excited into the conduction band, leaving an equal number of holes in the valence band. The created signal electrons drift against the electric field towards the n-doped region, which now acts as the anode. Simultaneously, the holes drift in the opposite direction towards the p-doped region, acting as the cathode. The number of electron-hole pairs N created by the incoming particle equals the energy of the incoming particle E divided by the average energy ω required to generate one electron-hole pair ($N = E/\omega$). Hence, collecting the charge at either side (anode or cathode) is a measure of the energy of the incoming particle. For silicon, the average energy is $\omega_{\text{Si}} = 3.62\,\text{eV}$ at room temperature $T = 300\,\text{K}$ [33]. This average energy ω

is larger than the band gap because phonons are also generated in the process and dissipated as thermal energy, which can not be measured. [34]

3.2. SDD Working Principle

The SDD is a special type of semiconductor detector based on the technique of sidewards depletion by E. Gatti [36]. Instead of equally large anode and cathode areas, SDDs have a very small anode relative to the sensitive volume. This leads to an improved energy resolution compared to common diodes since the read-out capacitance is reduced significantly. To maintain complete charge collection, p-doped rings are implanted around the anode as illustrated in Figure 3.4. They create an electric field with a strong component parallel to the surface. This is achieved by applying decreasing negative potentials from the outside to the inside rings. Signal electrons created anywhere in the depleted volume drift towards the anode in the center where they are collected.

To take full advantage of the small anode capacitance, a n-channel Junction-gate Field Effect Transistor (JFET) has been integrated into the center of the anode of the TRISTAN SDD [37]. This minimizes stray capacitances between the anode and the subsequent amplification circuit. The JFET needs to be shielded from the silicon bulk to prevent the loss of signal charges. This is realized by a so-called Inner Guard Ring (IGR) between the JFET and the anode, ensuring that the signal electrons can only enter the JFET through the anode. The voltage applied to this p-doped ring creates an electric field that shields the JFET and guides the electrons to the anode.

The entrance window side is the opposite side of the anode where the p-doped Back Contact (BC) is located that acts as the cathode. Further discussion of the entrance window is provided in Section 3.4 and 4.2. The silicon bulk between the cathode and anode is fully depleted by an applied reverse bias and serves as the sensitive detection volume for ionizing radiation.

3.3. TRISTAN Detector Design

The TRISTAN Detector is a multi-pixel SDD array fabricated by the Max-Planck Semiconductor Laboratory (HLL) from a silicon wafer with a thickness of $450\,\mu m$ [39]. Figure 3.5a shows a photograph of a TRISTAN detector module. The main part of a module is the $38 \times 40\,mm^2$ large detector chip hosting 166 hexagonally shaped SDD pixels. The small pixel size of $3\,mm$ minimizes charge-sharing effects and pixel change after backscattering and backreflection [40]. The TRISTAN detector system will consist of 9 modules arranged in a 3×3 grid as shown in Figure 3.5b. This
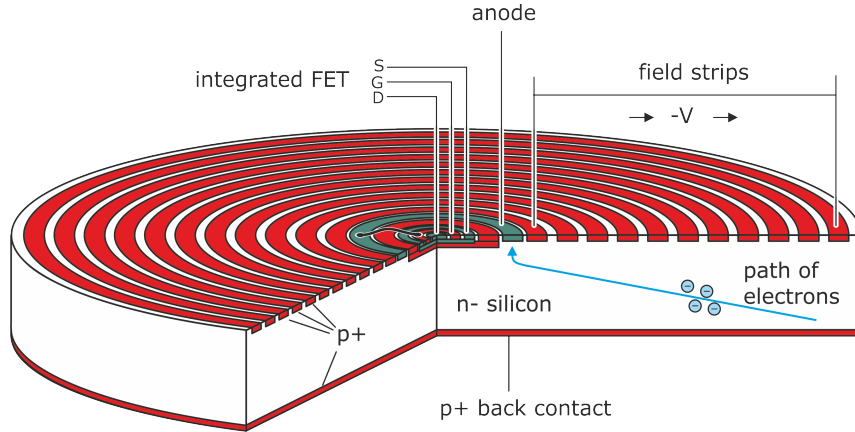
Figure 3.4: **Schematic View of an SDD**
The small n-doped anode (green) in the center ensures low read-out capacity. P-doped rings (red) around the anode create an electric field that guides signal electrons toward the anode, ensuring high charge-collection efficiency. The opposite p-doped side is called back contact and acts as the cathode. An integrated Field Effect Transistor (FET) in the center of the anode pre-amplifies the signal immediately to further maximize energy resolution. The IGR (red ring between the integrated FET and the anode) shields the FET from the silicon bulk. Figure taken from [38].

(a) Photograph of a TRISTAN Module

(b) TRISTAN Detector System Render
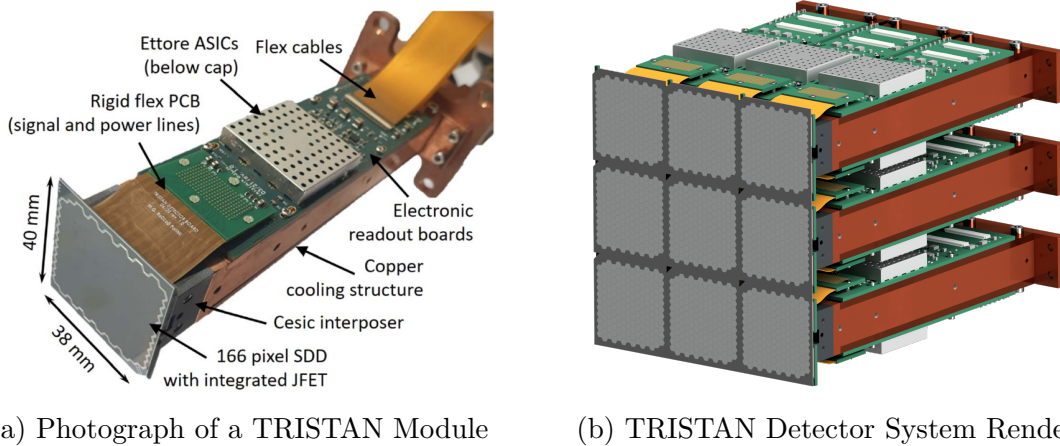
Figure 3.5: **Photograph of TRISTAN Module and Rendering of Detector System**
(a): Photograph of a TRISAN module. The detector chip in the front hosts 166 hexagonally shaped SDD pixels. It is glued onto a Cesic block connected to a copper cooling structure. The copper structure also hosts the readout electronics on the top and bottom surfaces. The SDDs are connected to the electronic readout boards via rigid-flex PCBs, allowing for 90° bending. The ASIC, called Ettore, amplifies the signal.
(b): Rendering of the TRISTAN detector system. Nine modules will be placed nearly seamlessly next to each other in a 3×3 grid. Figures taken from [39].

leads to a detector system comprising over 1000 pixels, enabling it to handle the high rates required for the sterile neutrino search. The detector chip is glued onto a Cesic interposer, a special silicon ceramic composite with a similar heat expansion coefficient as the silicon chip. The Cesic interposer is connected to a copper support structure hosting the readout electronics. The on-module electronics is mounted in the plane perpendicular to the detector chip, allowing a nearly seamless arrangement of the detectors next to each other. This minimizes the insensitive area of the detector system. To reduce electronic noise, the copper structure is also used to cool the detectors to temperatures around $-35\,°C$. The SDD pixels are electrically connected to the electronic readout boards via two rigid-flex printed circuit boards (PCBs). An application-specific integrated circuit (ASIC) called ETTORE amplifies the signal [38]. A more detailed discussion of the electronic readout chain used in the experimental setup of this thesis will be given in Section 5.

3.4. Detecting Electrons with TRISTAN

SDDs are typically used for X-ray measurements. However, the TRISTAN detector will be installed in the KATRIN beamline for high-precision electron spectroscopy. The energy deposition profile is different for electrons than for photons. Figure 3.6 illustrates the absorption mechanisms for the two types of particles. The dominant interaction for X-rays in the energy range of a few ten keV is the photoelectric effect. Thereby, the photon is completely absorbed and deposits all its energy. Hence, the energy deposition of photons in the detector material starts at the position of the photoelectric effect. For photons with energies above $5\,keV$, this happens statistically well inside the detector active volume [41]. In contrast, electrons directly start interacting with the detector material at the entrance window and continuously lose energy along their path. This way, electrons do not penetrate as far into the material as photons and deposit their energy much closer to the detector's surface.

The TRISTAN detector is passivated with a $10\,nm$ thin silicon dioxide (SiO_2) layer, which is an insulator. Charge carriers created in this region can not reach the anode. Additionally, the finite depth of the p-doping leads to an electric field that can guide the electrons away from the anode. As a result, the passivation layer and the finite depth of the p-doping lead to a around $100\,nm$ thick layer with reduced Charge Collection Efficiency (CCE), which is denoted as the entrance window region in the following.

A successful model describing the CCE of a TRISTAN module was developed in [42] and [43]. The CCE model reflects the structure of the SDD: it starts with the oxide layer at the surface with thickness t and a constant signal formation probability p_0. Since no signal electrons generated in the oxide layer can be collected by the anode,
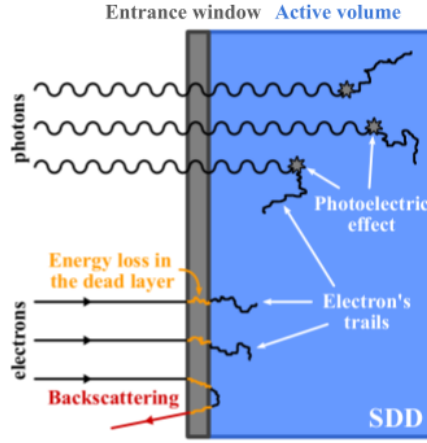
Figure 3.6: **X-ray and Electron Absorption Inside the Detector**
X-rays are absorbed mainly via the photoelectric effect and deposit their energy
well inside the detector. In contrast, electrons begin interacting immediately when
they enter the detector, losing energy as they pass through the entrance window and
are absorbed near the surface of the detector. Furthermore, there is the possibility
of backscattering, where electrons deposit only a part of their energy in the active
volume before they scatter out of the detector. Figure adapted from [41].

this probability is set to zero ($p_0 = 0$). Further into the material, charge collection
is active but reduced due to the p-doping. This area is modeled with a formation
probability starting from a value p_1 gradually approaching a unitary value with an
exponential behavior with scale parameter λ. Consequently, the CCE, depending
on the depth z, can be written as:

$$CCE(z; t, p_0, p_1, \lambda) = \begin{cases} p_0, & z < t \\ 1 + (p_1 - 1) \cdot \exp\left\{-\frac{z-t}{\lambda}\right\}, & z > t \end{cases} \qquad (3.1)$$

Figure 3.7 shows an exemplary representation of the CCE as a function of depth
based on a Monte Carlo simulation.

The response of the detector to electrons holds characteristic features that differ
from the response to X-rays since electrons lose a significant amount of their energy
within the entrance window region with reduced CCE. Figure 3.8 shows an exem-
plary mono-energetic 10 keV electron spectrum measured with a TRISTAN detector.
An ^{55}Fe source with its two main peaks $K_\alpha = 5.9$ keV and $K_\beta = 6.5$ keV is used to
calibrate the spectrum [44]. The most prominent features of the electron spectrum
are explained in the following.

Main Peak and Low-Energy Tail

Most of the electron's energy will be deposited in the sensitive area of the detector,
creating a main peak, here at 10 keV. However, electrons will always lose a fraction
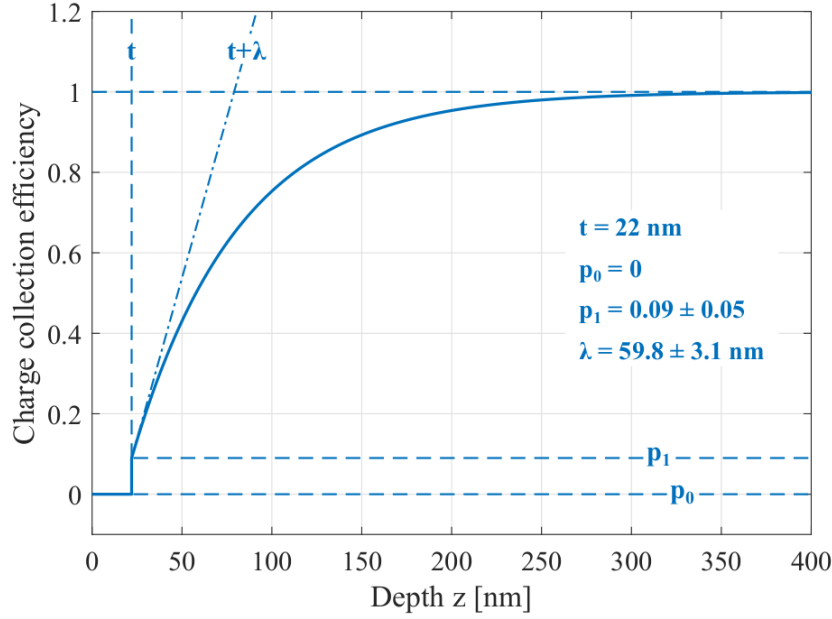of their energy in the entrance window region, where CCE is significantly reduced.

Figure 3.7: **Modeled Charge Collection Efficiency**
The CCE is a function of the depth z in the device. The parameters' values and uncertainties are the best fit values obtained from a Monte Carlo simulation for a previous TRISTAN prototype detector module with 47 pixels. Figure taken from [41].
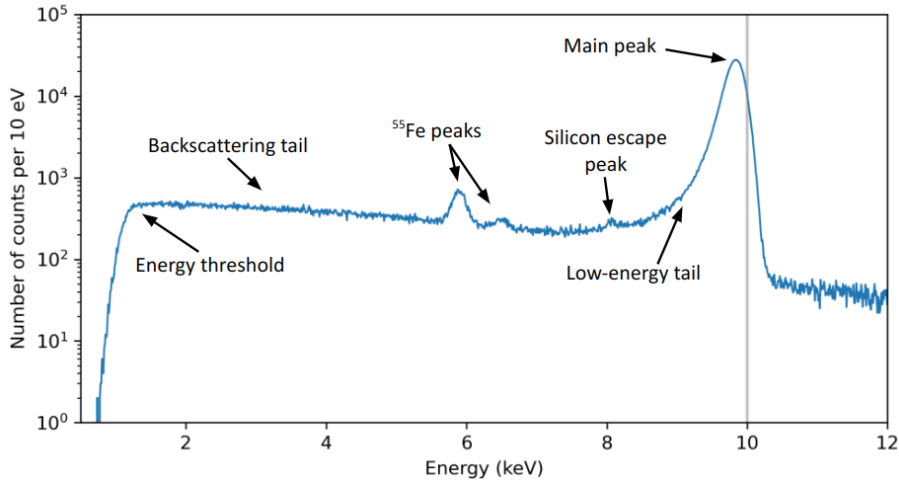

Figure 3.8: **Detector Response to Electrons**
Exemplary electron spectrum of $10\,\mathrm{keV}$ monoenergetic electrons measured with a TRISTAN detector. For calibration, an ^{55}Fe source was used in parallel. The main peak at $10\,\mathrm{keV}$ is slightly shifted towards lower energies due to charge loss in the entrance window region. This also leads to a prominent low-energy tail of the main peak. When electrons ionize the silicon atoms, characteristic X-rays are created, which can leave the detector forming the silicon escape peak next to the main peak. Electrons scattering back from the detector surface lead to a large backscattering tail in the spectrum. The energy threshold terminates the spectrum. Below this energy, the detector can not distinguish between noise and physics events.

In the spectrum, this leads to a slight shift of the main peak towards lower energies, and the main peak becomes asymmetric with a pronounced low-energy tail. Since the energy deposition profile depends on the electron's energy (higher energy electrons penetrate further into the material), the entrance window effect decreases for higher electron energies [31]. Irradiating the detector with ionizing radiation can further enhance the reduction of the CCE in the entrance window region and will be discussed in Section 4. The Full Width at Half Maximum (FWHM) of this main peak will be used as the value for the energy resolution of the detector throughout this thesis.

Silicon Escape Peak

Incoming electrons can ionize the silicon atoms, creating characteristic X-rays with $\Delta E_{\mathrm{esc}} = 1.74\,\mathrm{keV}$. If those X-rays leave the detector, the detected energy of the electron is reduced by ΔE_{esc}, which leads to a so-called silicon escape peak [31].

Backscattering Tail

The spectrum between the silicon escape peak and the detection threshold is dominated by the backscattering tail. Primary and secondary electrons can scatter back from the detector surface or escape the detector before complete energy deposition. For a more detailed description refere to [45].

4.   Theory of Radiation Damage

The performance of electron measurements using SDDs is significantly influenced by the SDD's entrance window (cf. Section 3.4). In the technology used for the fabrication of TRISTAN SDDs, there are two possibilities to terminate silicon: aluminum and SiO_2. The advantage of aluminum is that it proves to be significantly harder to radiation than oxide entrance windows [46]. However, passivation with aluminum can not be realized in as thin layers as oxide passivation allows. Therefore, an SiO_2 entrance window was chosen for the TRISTAN detector. This decision presents the challenge of addressing potential radiation damage induced by those very electrons that the detector is designed to measure. Incoming electrons ionize atoms in the SiO_2 layer, leading to trapped charges in the SiO_2-Si interface [46]. This damage influences the charge collection of the SDD and is thereby critical for the energy resolution of the TRISTAN detector. Therefore, electron-induced radiation damage will be investigated in the scope of this thesis.

This chapter provides an overview of the damage expected from theoretical considerations, serving as a basis for comparison with the experimental results obtained in the scope of this thesis. It starts with an overview of possible interactions of electrons in silicon in Section 4.1. In Section 4.2, the role of ionization within the SiO_2 entrance window is discussed. Finally, in Section 4.4, possible recovery mechanisms are described.

4.1.   Interaction of Electrons in Silicon

In general, collisions of the incoming electrons with the electrons or with the nuclei of the silicon atoms have to be considered. Both collisions can happen elastically, which would cause no damage. Inelastic collision with the silicon nuclei would produce a primary knock-on atom (PKA). This is an atom that is displaced from its lattice due to irradiation and would influence the detector performance drastically. However, electrons measured within the sterile neutrino search with KATRIN will have energies ranging from 0 to $40\,\text{keV}$ [1] at most while the threshold to produce a PKA is $260\,\text{keV}$ [47]. Therefore, no damage through PKAs is expected. The only remaining interaction that could potentially cause damage is inelastic collision with the electrons of the silicon atoms, i.e., ionization.

Ionization of the silicon atoms can happen in the silicon bulk of the SDD or in the SiO_2 entrance window. In the bulk, ionization is the underlying detection principle

---

[1]For the sterile neutrino search with KATRIN, a post acceleration of $E_{\text{PA}} = 20\,\text{keV}$ is planned. Therefore, the tritium endpoint $E_0 = 18.6\,\text{keV}$ plus the post acceleration gives electron energies of roughly $38.6\,\text{keV}$ at most.

of semiconductor detectors. The process is completely reversible due to the electrical conductivity of silicon and does not produce any damage. Therefore, only ionization within the SiO_2 passivation layer and the SiO_2/Si interface is of relevance.

4.2. Ionization within the SiO_2 Entrance Window

At the surface of the silicon wafer, the periodical crystal structure cannot be continued. Silicon atoms near the surface are only partly surrounded by neighboring silicon atoms, leading to dangling bonds. Therefore, the surface is highly chemical and electrical reactive and needs to be passivated. Silicon naturally grows a SiO_2 passivation layer, saturating the dangling bonds with oxygen. When this naturally ongoing process is performed in a controlled manner within a pure oxygen atmosphere (so-called dry oxidation), an electrically and chemically stable and much more homogeneous surface is created. The process takes place at $900\,°C$ to $1200\,°C$ [46].

The obtained interface between the silicon and the SiO_2 consists of the last monocrystalline silicon layer followed by a monolayer of incompletely oxidized silicon SiO_x, a distorted SiO_2-transition layer and a subsequent distortion-free SiO_2 layer. Due to this imperfect interface and potential impurities in the oxide, various defects arise that can act as traps for electrons and holes. Figure 4.1 shows the bonding conditions at the interface with possible defects. The two main defects relevant for radiation damage investigations are oxygen vacancies leading to positive oxide charges and silicon valences called interface states creating interface trapped charges (cf. defect (3) and (1) in Figure 4.1 respectively) [46].

4.2.1. Positive Oxide Charges

In the oxidation process, several precursors for positive oxide charges are created, like oxygen vacancies. Oxygen vacancies are weak Si-Si bonds missing an oxygen atom [48]. They appear in a distance up to $3\,nm$ from the Si/SiO_2 interface [46]. Since SiO_2 is an insulator, not all electron-hole pairs created in this material will recombine, but some can get separated. Electrons prove to be rather mobile in SiO_2 and escape into the silicon bulk quickly within a typical time of around $100\,ps$ [49]. In contrast, holes have low effective mobility and travel through the oxide in a time span in the order of seconds via a complicated stochastic trap-hopping process [46, 50]. Therefore, they have enough time to get trapped by breaking up the weak Si-Si bonds of oxygen vacancies [48]. These trapped oxide charges are not mobile and are located near the interface to silicon. They lead to a net positive charge influencing the electric field distribution of the SDD and thereby impact the CCE. A saturation of the oxide charge buildup has been experimentally observed by [51] and [52] and is explained by a limited number of traps in the oxide.
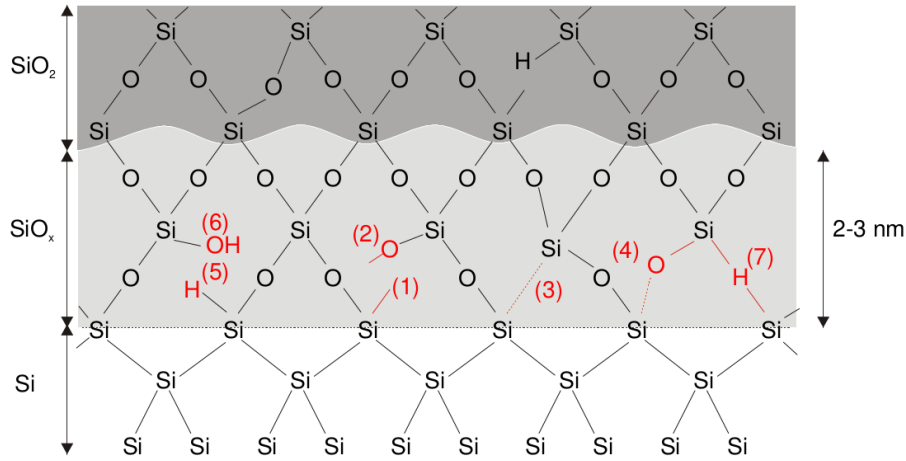
Figure 4.1: **Bonding Conditions at Si/SiO₂ Interface**
The crystalline silicon is followed by a monolayer of incompletely oxidized silicon SiO_x and the subsequent silicon dioxide layer. In the transition layer, several defects can occur: (1) silicon valences, (2) oxygen valences, (3) oxygen vacancies, (4) stretched Si-O bonds, (5) hydrogen-saturated valences, (6) hydroxyl groups, and (7) hydrogen-saturated oxygen vacancies. The most important defects regarding radiation damage investigations are silicon valences and oxygen vacancies. Figure taken from [46].

4.2.2. Charged Interface States

Unsaturated silicon atoms at the interface form electrically active defects. These defects act as centers of recombination for electrons and holes, resulting in charged interface states. Hydrogen annealing at $500\,°C$ is used in the fabrication process of the SDD to neutralize a high fraction of those charged interface states. The hydrogen atoms react with the dangling bonds of the silicon, deactivating the interface states. However, irradiating the material with ionizing radiation can break the weak Si-H bond, forming unsaturated silicon atoms again. These irradiation-induced interface states act as generation and recombination centers and potentially cause both an increase of leakage current and the loss of signal electrons [46].

4.3. X-rays and Radiation Damage

The damaging effect occurs not only for irradiation with electrons but could be created by any type of ionizing irradiation, e.g. X-rays. However, since X-rays penetrate further into the material and deposit less energy within the entrance window compared to electrons, the damage caused by X-rays is significantly smaller. For the same reasons, X-rays are additionally less affected by already-caused radiation damage of the type described above. Therefore, a potential decrease in energy resolution is only expected for electrons and not for X-rays in the scope of this thesis. An increased leakage current, however, would influence the detector performance in general, independent of the type of radiation.

4.4. Recovery Mechanisms

For the sterile neutrino search with KATRIN it is crucial to understand the detector response with high precision. This requires accounting not only for potential degradation of the detector's performance due to radiation damage but also for any recovery during measurement pauses. Positive oxide charges generated by electron radiation on the oxide structures may gradually heal over time. Two main processes contribute to this recovery: thermal healing and healing through tunneling. In the thermal healing process, thermally created electrons can recombine with the trapped holes. However, this process is significant only at temperatures above $100\,°\text{C}$ and is, therefore, not expected and not realizable within the TRISTAN detector application. Consequently, only healing through tunneling is of concern. In this mechanism, electrons from the silicon bulk tunnel into the oxide and recombine with the trapped holes. Pahlke demonstrated in [46] that this process follows a logarithmic time dependence. Additionally, charged interface states can be neutralized by hydrogen re-saturation. However, since this reaction requires temperatures exceeding $400\,°\text{C}$, it is also not applicable to the TRISTAN detector [46].

5. Experimental Setup for Radiation Investigation
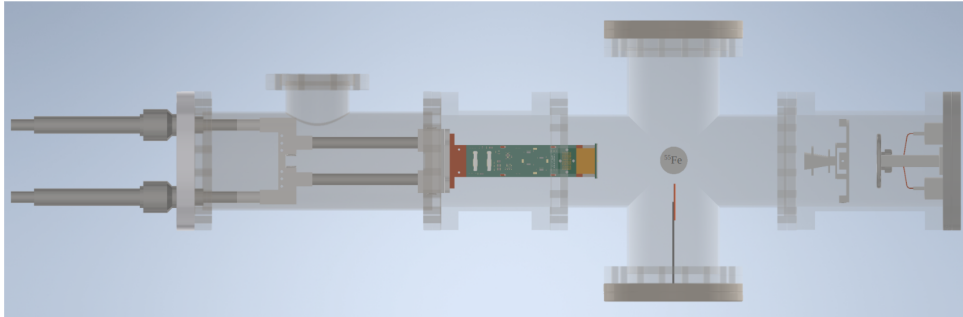
(a) Rendering of the Vacuum Setup
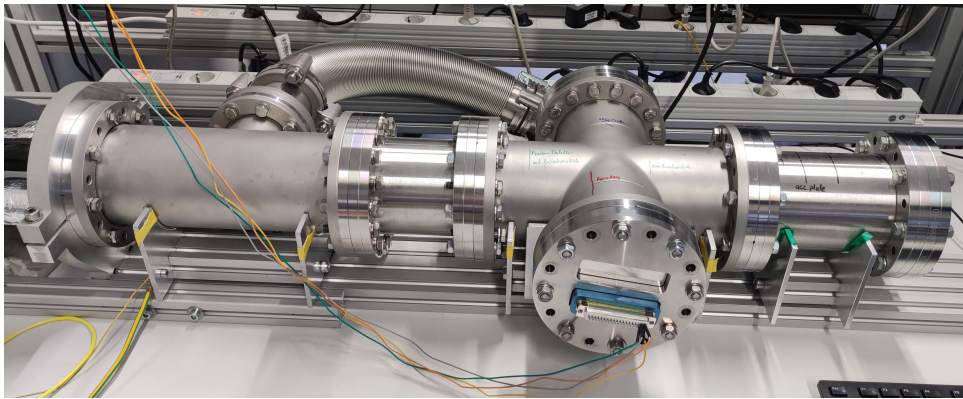
(b) Photograph of the Vacuum Setup

Figure 5.1: **Rendering and Photograph of the Experimental Setup**
(a): Rendering of the experimental setup used to investigate electron-induced radiation damage to a TRISTAN module. The cross-shaped vacuum chamber hosts a 166-pixel TRISTAN module and a custom-designed electron gun with steering coils. Perpendicular to the beam direction of the electron gun, a copper plate is installed in one arm of the vacuum cross for rate monitoring. An ^{55}Fe source is placed for calibration in the middle of the cross.
(b): Photograph of the vacuum setup installed on rails.

The experimental setup to investigate electron-induced radiation damage to a TRISTAN module developed as part of this thesis is shown in Figure 5.1a. The setup consists of a 86 cm long, cross-shaped vacuum chamber housing a 166-pixel TRISTAN module and a custom-designed electron gun. The electron gun produces a high-rate electron beam and was used to irradiate the module to study electron-induced radiation damage. The individual parts of the vacuum chamber are installed on a rail to easily open and close the setup (cf. Figure 5.1b). A vacuum pressure of 10^{-6} to 10^{-7} mbar can be reached with a TURBOLAB Core turbomolecular pump from Leybold[2].

---

[2]Leybold GmbH, Bonner Str. 498, D-50968 Köln, Germany
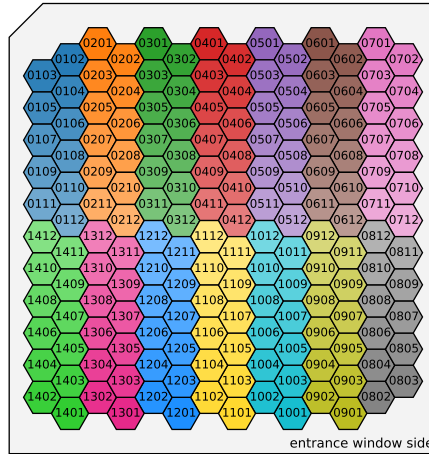
Figure 5.2: **Pixel Map Representing the Naming Scheme**
Pixel map showing the general naming scheme based on reset groups.

This chapter provides a detailed overview of the TRISTAN detector module and electron gun used in the radiation damage tests. Section 5.1, details the detector module covering its electronic readout chain, the calibration process, and the effect of an increased entrance window. Section 5.2 focuses on the electron gun developed for this experiment; discussing its design, the rate monitoring using a copper plate, beam deflection via steering coils, and the commissioning of the electron gun.

5.1. TRISTAN Module

The TRISTAN module used for every measurement in this thesis is a 166-pixel detector named S0-166-6. The detector design is described in detail in Section 3.3. Figure 5.2 presents a pixel map illustrating the naming scheme applied to the 166 pixels. According to this scheme, the Cell ID is based on the reset groups, which will be explained in Section 5.1.1. The first two digits represent the reset group, while the last two digits number the twelve pixels within the reset group. To increase sensitivity, the detector can be cooled down to around $-35\,°C$ at the detector chip with a Julabo[3] F81 refrigerated circulator. For this, the copper structure hosting the detector chip and the on-module electronics is mounted onto the heat exchange block of the cooling interface pipes containing a silicon-based cooling liquid (cf. Figure 5.3). The interface pipes are electrically and thermally insulated at the position of the feedthrough flange.

5.1.1. Electronic Readout Chain

Figure 5.4 shows a schematic of the electronic readout chain of a TRISTAN SDD pixel. The on-module electronics consists of two identical Printed Circuit Boards (PCBs), each with 7 ETTORE ASICs to amplify the signal. The ETTORE ASICs

---

[3]JULABO GmbH, Gerhard-Juchheim-Strasse 1, 77960 Seelbach, Germany
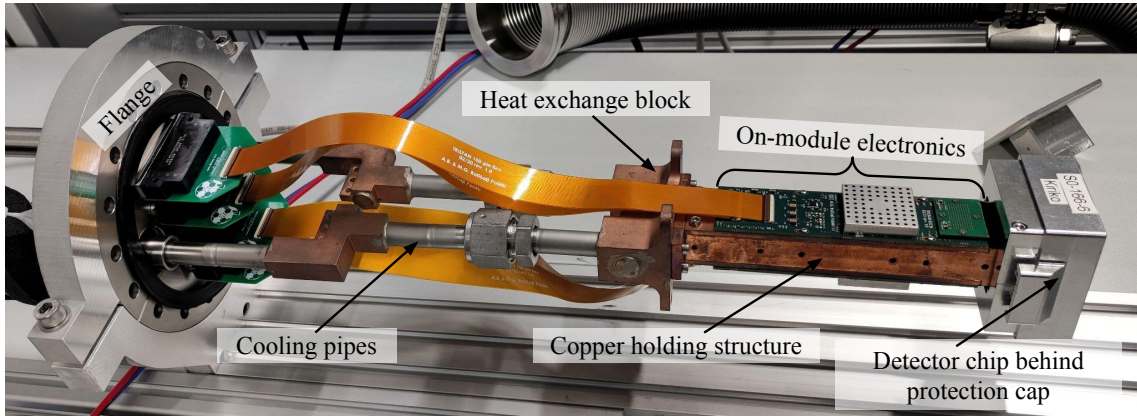
Figure 5.3: **Photograph of the Cooling Structure**
The detector chip is glued onto a Cesic block which is screwed onto a copper structure for good heat transfer. The cooling is realized with a cooling liquid guided into the vacuum in pipes ending in a heat exchange block onto which the copper structure is screwed.
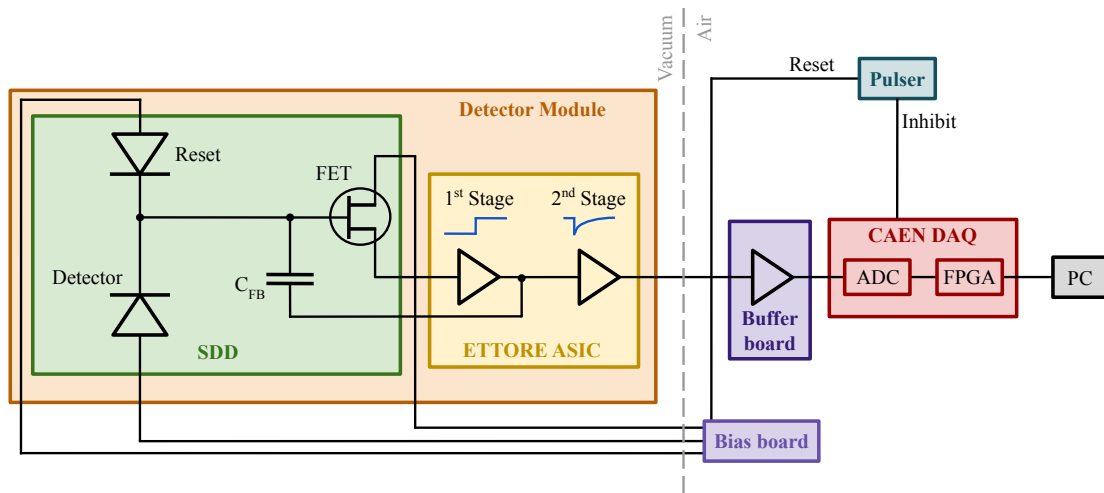

Figure 5.4: **Schematic of the Electronic Readout Chain**
The bias board supplies the necessary voltages to the SDD. The electric signal collected at the feedback capacitance C_{FB} of an SDD pixel is processed by the ET-TORE ASIC, where two different amplification stages can be chosen. Subsequently, the buffer board amplifies the signal further before it reaches the CAEN DAQ where and ADC digitizes the signal and an FPGA performs the energy reconstruction. A pulser periodically triggers a reset of the feedback capacitor via a signal routed through the bias board to the SDD. Simultaneously, another signal called inhibit disables the ASIC during the reset process.

provide two different amplification stages. A subsequent buffer board further amplifies the signal. After the buffer board, the signal is digitized and the energy is reconstructed in the Data Acquisition (DAQ) unit before a LAN connection passes the output to the PC. A bias board provides the needed supply voltages, controls ETTORE settings, and distributes the signals from a pulser to reset the feedback capacitor. In the following paragraphs, the individual parts of the electronic readout chain are explained in more detail.

On-Module Electronics

As described in Section 3.2, an incoming electron creates electron-hole pairs in the depleted volume of the SDD. The electrons are guided towards the anode, where they are collected. To read the signal from the anode, a Charge Sensitive Amplifier (CSA) is used. It consists of the integrated JFET connected to the anode and the first amplification stage of the ETTORE ASIC [53]. The CSA integrates the collected charge and converts it into a voltage step proportional to the energy deposited in the detector. Leakage current continuously charges the feedback capacitor. To prevent saturation, the feedback capacitor has to be drained by a periodical external reset through an additional circuit. Figure 5.5a presents a typical signal from the first amplification stage, where an event appears as a step in the voltage ramp created by leakage current. The reset pulses are visible as steep decreases every 2 ms.

The second stage amplification of the ETTORE ASIC adds an RC-circuit to the CSA principle. Due to the addition of the resistor R, the capacitor C continuously discharges over time. The events appear as pulses now with a characteristic decay time of 15 µs introduced by the RC-circuit [53]. With this, the second stage acts as a high-pass filter, only keeping fast signals like the events and filtering out slower signals like leakage current. This enables an amplification of the first stage signal by a factor of 5 to 10. Figure 5.5b shows a typical output for this stage.

Bias Board

The SDD needs several supply voltages and currents for operation, which are provided by the XGlab[4] biasing and control board. The bias board was specifically built to supply and control the TRISTAN detector modules for first characterization measurements. Therefore, smaller modifications to the factory design were performed, which are discussed in [54]. Furthermore, the bias board manages the different settings of the ETTORE ASICs and receives a periodic reset signal from a pulser, which it distributes to the SDD to reset the feedback capacitor.

---

[4]XGLab S.R.L., Via Conte Rosso 23, I-20134 Milano, Italy

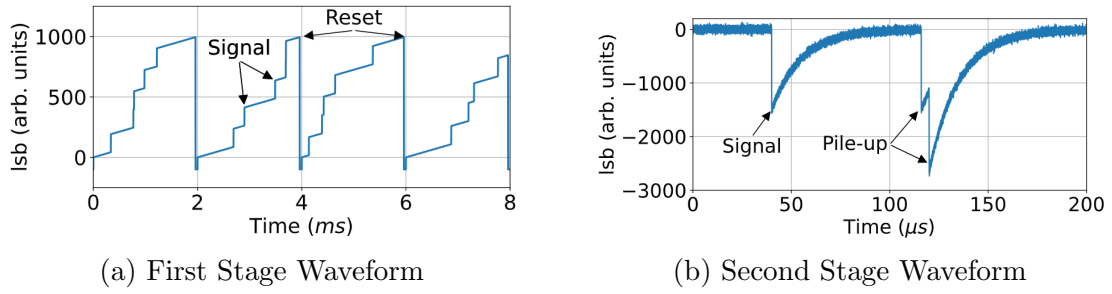(a) First Stage Waveform

(b) Second Stage Waveform

Figure 5.5: **Exemplary Signal Output for Both ETTORE ASIC Stages**
(a): The first stage waveform consists of a ramp created by leakage current with superimposed steps corresponding to signal events. The accumulated charge at the anode is drained every 2 ms leading to steep reset decreases in the waveform.
(b): Second stage amplification inverts the pulse direction and introduces a decay constant of 15 μs. It acts as a high-pass filter, therefore the slow leakage current ramp is filtered out. If two events happen shortly after each other, the second event can still lie on the decaying shoulder of the first event, leading to a pile-up event. Both figures taken from [54].

Buffer Board

After the signal is amplified by the ETTORE ASIC, a feedthrough guides the signal out of the vacuum to the XGLab buffer boards. Here, the signal is further amplified by a factor of two, and the baseline voltage and signal output can be adjusted.

DAQ System

The output waveform of the buffer board is forwarded to the CAEN[5] DAQ system, which consists of 3 CAEN VX2740B digitizers. Here, the signal is digitized via their integrated 16-bit Analog-to-Digital Converter (ADC) with a sampling rate of 125 MHz. Each digitizer card can handle 64 channels in parallel [55].

Subsequently, Field Programmable Gate Arrays (FPGAs) reconstruct the energies of the detected events using a trapezoidal filter with an exponential baseline correction. The accuracy of the energy reconstruction is dependent on the signal being step-like. Therefore, the second stage waveform is first deconvolved with an Infinite Impulse Response (IIR) filter to remove the exponential decay. The resulting waveform is shown in Figure 5.6a. The energy is reconstructed by averaging the waveform in two windows with the rise time length t_{rise}, which are separated by the gap time t_{gap}. Those two windows are swept over the entire waveform while the averages are subtracted from each other. This leads to a trapezoidal-shaped output as shown in Figure 5.6b. The height of the trapezoid corresponds to the height of the step signal in the waveform. The gap time needs to be larger than the pulse rise time of the signal to ensure that averaging is performed over the flat regions before and after the signal [54]. For the sterile neutrino search with KATRIN a rise time

---

[5]CAEN S.p.A., CAEN Group, Via Vetraia 11, 55049 Viareggio, Italy

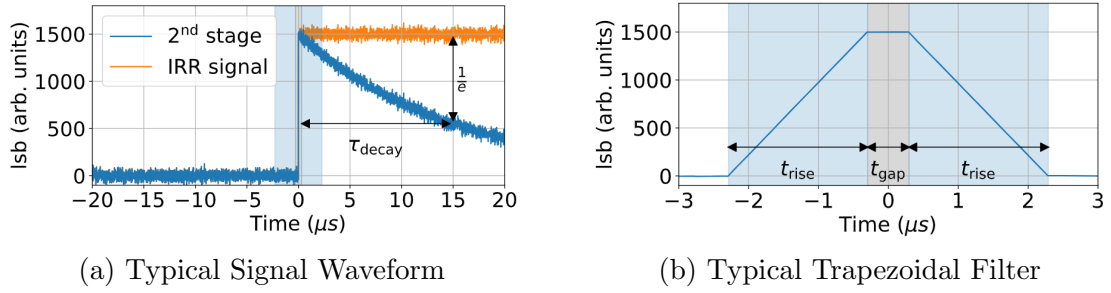(a) Typical Signal Waveform

(b) Typical Trapezoidal Filter

Figure 5.6: **Illustration of the IIR and Trapezoidal Filter**
(a): The blue waveform is a typical second stage amplification waveform with the decay time $\tau_{\mathrm{decay}} = 15\,\mu s$. The orange waveform is obtained after deconvolving the blue waveform with an IIR filter. The shaded areas represent the trapezoidal filter. (b): Typical trapezoidal filter response to a waveform pulse for a IIR filtered waveform with $t_{\mathrm{rise}} = 2\,\mu s$ and $t_{\mathrm{gap}} = 0.5\,\mu s$. Both figures taken from [54].

of $t_{\mathrm{rise}} = 1\,\mu s$ is targeted. Due to expected higher rates, the measurements in this thesis were performed with a shorter filter rise time of $t_{\mathrm{rise}} = 800\,\mathrm{ns}$ and a gap time $t_{\mathrm{gap}} = 400\,\mathrm{ns}$ to reduce pile-up.

The data can be recorded in different acquisition modes differing in their amount and type of data. The most detailed information can be obtained with the waveform data acquisition mode. Here, the raw digitized waveform of each channel is saved in 8 ns increments. Due to the large amount of data created in this mode, only short datasets in the order of 100 ms can be recorded. Waveform mode was used in this thesis to measure the leakage current of the detector. The most commonly used readout mode in this thesis is the list mode data acquisition. Here, only the timestamp and the already reconstructed energy of a triggered event above a certain threshold are saved. This reduces the amount of data significantly and is suitable for longer measurements as performed in the scope of this thesis. Further reduction of data can be achieved with the spectrum data acquisition mode, where the reconstructed energies are already processed into a histogram. The list wave readout mode provides a compromise between the waveform and list mode acquisition. It operates the same as list mode but saves an additional snippet of the corresponding waveform with a length of up to 20 μs. While this provides the ability to check the filter performance by looking at the saved waveforms, it still produces a lot of data and is unsuitable for longer measurements.

Pulser

The pulser periodically sends a reset signal to the bias board, which passes it on to the SDD chip. A reset signal is needed to drain the anode and feedback capacitor of the SDD pixels to prevent saturation. Simultaneously, an inhibit signal is sent to the CAEN DAQ system to disable the ASICs, preventing further readout during the reset process. The entire SDD chip is reset with one synchronous signal to avoid

crosstalk between pixels. To this end, the pulsed signal is simultaneously distributed to reset groups of twelve pixels per reset line. The naming scheme used for the pixels throughout this thesis is derived from the structure of those reset groups (cf. figure 5.2). The reset pulse for the measurements in this thesis was set by a Keysight[6] 33500B Waveform Generator with a period of 500 µs and a pulse width of 1 µs. Simultaneously, the inhibit was set with the same device and the same period and a pulse width of 100 µs.

5.1.2. Calibration

The DAQ system digitizes the signal in units of least significant bits (lsb), a unit that reflects the resolution of the ADC. Each lsb corresponds to a specific voltage range, which must be calibrated to convert it to collected energy in the detector in eV. To convert the digitized signal into energy values, a ^{55}Fe X-ray calibration source is used. The spectrum of this source is well-known and has prominent $K_\alpha = 5.9\,\text{keV}$ and $K_\beta = 6.5\,\text{keV}$ peaks in the relevant energy range [56]. In the calibration process, both peaks are fitted with a Gaussian function to obtain a linear calibration curve going through the peak positions with a slope s and offset o:

$$E[\text{eV}] = s[\text{eV/lsb}] \cdot E[\text{lsb}] + o[\text{eV}]. \tag{5.1}$$

To this end, a disk-like ^{55}Fe source with 3.944 MBq activity is placed in the middle of the cross-shaped vacuum chamber (cf. Figure 5.7a). The number of events counted by each pixel of the detector in this configuration over a measurement time of 30 min is shown in Figure 5.7b. On average, 50 kilocounts per pixel are detected. There are six non-functioning pixels that did not detect any events, likely due to a connection issue, marked in white. Otherwise, the detector shows a homogenous performance. Since the source is positioned on the ground of the vacuum chamber in front of the detector, the X-ray flux reaching the upper hemisphere of the detector is reduced compared to the lower hemisphere. A more detailed discussion of the detector performance with X-rays from the ^{55}Fe source will follow in Section 6.2 where the initial detector performance with respect to electrons, X-rays, and leakage current is presented.

5.1.3. Increased Entrance Window Effect

During the preparation process for the radiation damage studies following in the next chapter, an increased entrance window effect occurring in electron measurements was observed. Figure 5.8 shows in blue the spectrum of one pixel of an electron measurement where 15 keV electrons were shot onto the detector homogeneously. It was performed directly after cooling the detector with the chiller set to $-50\,°\text{C}$.

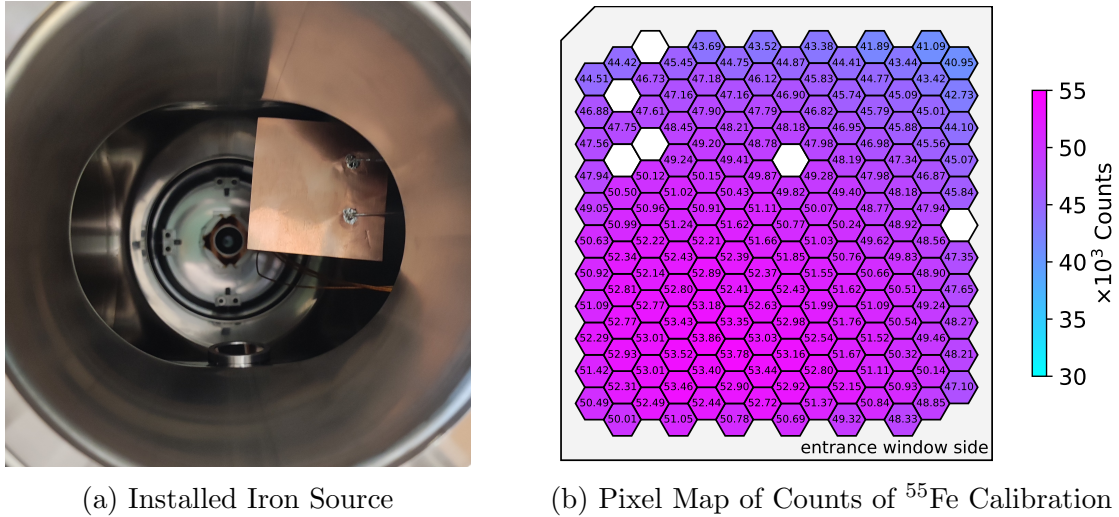[6]Keysight Technologies, 1400 Fountain grove Parkway, Santa Rose, CA, 95403-1738

(a) Installed Iron Source

(b) Pixel Map of Counts of ^{55}Fe Calibration

Figure 5.7: **Photograph of Installed ^{55}Fe Source and Pixel Map of Counts**
(a): Photograph of the ^{55}Fe Source installed in the middle of the cross-shaped vacuum setup.
(b): Pixel map showing the number of counts coming from the ^{55}Fe calibration source during a 30 min long calibration measurement. The white pixels are non-functional.
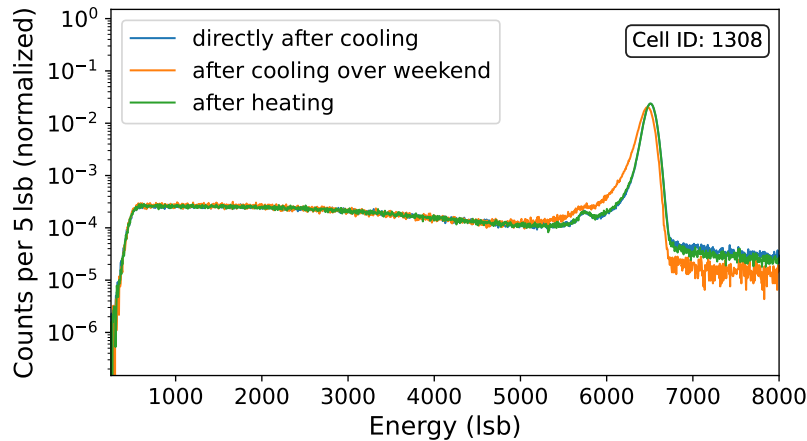

Figure 5.8: **Spectra Revealing an Increased Entrance Window Effect**
Spectra of a 15 keV electron measurement normalized to the total number of counts demonstrating that energy resolution deteriorates with longer cooling times (orange vs. blue line). The peak shift to lower energies and the prominent low-energy shoulder indicate an increase in the entrance window thickness. The effect can be reversed by heating the detector (green line). During those measurements, no ^{55}Fe source was installed. Since calibrating the spectra with the 15 keV electron peak would swallow the observed peak shift, no calibration was applied.

A mean energy resolution over all pixels of 325 eV (FWHM) was achieved. Then, the setup was left in the cooled state for 3 days, and the same measurement was performed again. The resulting spectrum for the same pixel (orange line) shows a significantly worse energy resolution than the first spectrum. The peak is shifted to lower energies, and the low-energy shoulder is pronounced. The mean energy resolution worsened by 40 eV to 365 eV (FWHM). This kind of degradation resembles an increased entrance window effect. When the entrance window region, where CCE is decreased as described in Section 3.4, is extended, electrons lose more energy in an insensitive region, leading to the observed peak shift and low-energy shoulder. It is likely that a frost layer accumulates at the entrance window of the detector, extending the insensitive entrance window region.

A possible explanation for this frost layer is that the cooling structure is not completely tight. The longer it cools, the more cooling liquid freezes onto the detector's surface, creating an additional layer. This hypothesis was tested by heating the detector again to evaporate the additional frost layer from the detector surface. Then, the detector was cooled down again, and a measurement was taken directly when the chiller reached the set $-50\,°C$. The resulting green spectrum in Figure 5.8 shows that the spectral distortions vanished, and the energy resolution was restored. This behavior supports the hypothesis of an additional frost layer freezing onto the detector while cooling. Further tests revealed that the effect consistently occurs when the detector is cooled and, hence, must be considered in radiation damage studies.

5.2. Electron Gun

The design of the electron gun developed for this setup is driven by three key requirements. First, the electron gun must produce monoenergetic electrons with kinetic energies up to 15 keV to lie within the relevant energy range of 0 to 40 keV. Second, it needs to allow for electron rates in the order of 10^9 cps and a stable operation over about 5 hours to test for radiation damage in reasonable timespans. Finally, the electron beam must produce a sufficiently large spot size to easily irradiate the SDD chip ($38 \times 40\,mm^2$). To this end, additional steering coils were developed to deflect and shape the electron beam. Rate monitoring of the electron beam is performed via a copper plate connected to a multimeter. Figure 5.9 shows a schematic of the electron gun, including the steering coils and the copper plate for rate monitoring.

5.2.1. Electron Gun Design

Electron beams can be generated by thermionic, high field, and photoemission effects [57]. For this setup, a thermionic electron gun based on the design in [58] was chosen due to its simplicity and capability to deliver nearly unlimited electron rates. In thermionic electron guns, a thin filament is heated to high temperatures
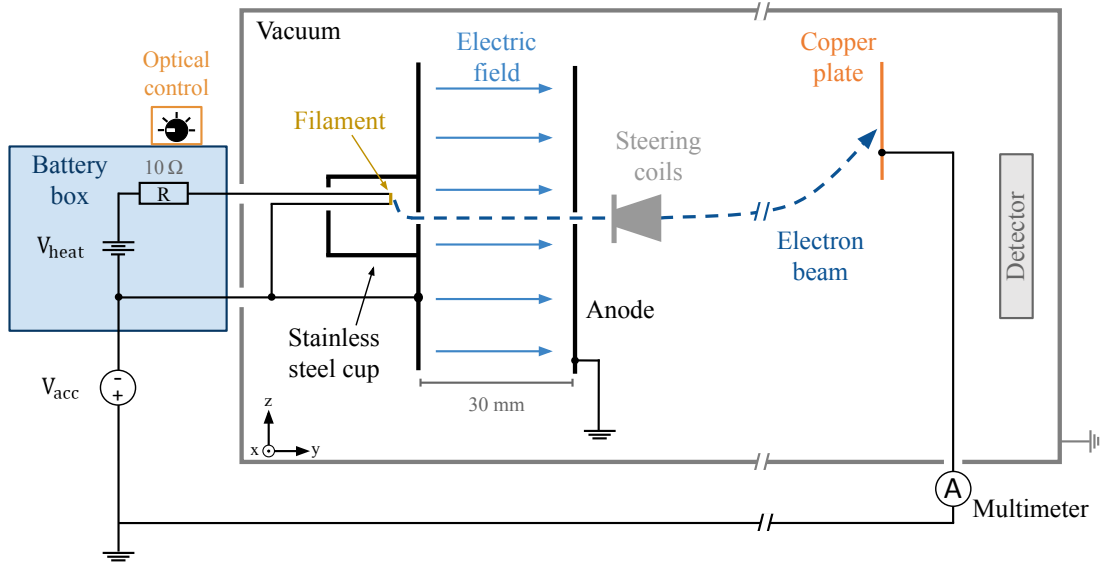
Figure 5.9: **Schematic of the Electron Gun**
The filament is placed inside a stainless steel cup. The heating voltage U_heat is supplied by a battery via a $10\,\Omega$ resistor to the filament. It can be controlled through an optical control circuit sitting inside a battery box. The cup is mounted onto a top plate with a $3\,\mathrm{mm}$ guiding hole through which the electrons can escape. The cup is put on negative high voltage while the anode is grounded. This creates an electric field that accelerates the generated electrons towards the anode. A pair of steering coils can be used to guide the beam onto a copper plate connected to a multimeter for rate monitoring. The schematic is not to scale.

whereby the electrons gain enough thermal energy to overcome the work function E_W of the material and escape the surface [57]. The work function is the minimal required energy for an electron to escape from the surface. To reduce the light output of the filament (which worsens the energy resolution of the SDD) the filament needs to be operated at comparably low temperatures T. To still reach high electron rates, a low work function is required. This can be achieved with an approximately $5\,\mathrm{mm}$ long and $25\,\mathrm{\mu m}$ thin tantalum (Ta) filament with a low work function of $E_\mathrm{W} = 4.25\,\mathrm{eV}$ [59]. The current density J emitted in thermionic emission follows Richardson's law:

$$J = AT^2 \exp\left(-\frac{E_\mathrm{W}}{k_\mathrm{B}T}\right) \tag{5.2}$$

where A denotes a constant $A \approx 1.2 \cdot 10^6\,\mathrm{Am^{-2}K^{-2}}$ and k_B the Boltzmann constant [57].

To heat the filament it is squeezed between two wires (cf. Figure 5.10a) which are connected to a battery via a series resistor of $10\,\Omega$ and two high voltage vacuum feedthroughs from Lemo[7]. The heating voltage U_heat can be precisely set with

---
[7]High Voltage Connectors, Lemo, Chemin des Champs Courbes 28, 1024 Ecublens, Switzerland

a high-voltage optocoupler circuit. The filament sits inside a stainless steel cup, which is set on negative high voltage and electrically connected to the negative side of the filament. The cup is mounted onto a stainless steel top plate with a guiding hole of 3 mm diameter, which also sits on negative high voltage. This configuration repels any electrons emitted to the side of the filament toward the guiding hole. The top plate is screwed via two ceramic insulators directly onto a flange of the vacuum chamber. This on-flange design ensures practical installation inside the vacuum cross. Figure 5.10b shows a photograph of the assembled electron gun.

In 30 mm distance from the top plate, another stainless steel plate with an 8 mm guiding hole is installed. This plate is grounded and, therefore, acts as the anode. Between the top plate on negative high voltage and the anode on ground builds up an electric field that accelerates the electrons towards the anode. The acceleration voltage, i.e., the negative voltage applied to the stainless steel cup, top plate, and filament, is provided by an adjustable precision high voltage supply with negative polarity from Heinzinger[8] and can be set up to 20 kV.

When the tantalum wire is heated, not only electrons escape the surface, but also photons are created, leading to a photocurrent on the detector. This photocurrent adds to the leakage current of the detector and, therefore, worsens the energy resolution. The stainless steel cup and top plate shield most of the light produced by the glowing filament. Nevertheless, light can escape through the rather large guiding hole needed to reach high electron rates. To reduce the amount of light reaching the detector, the filament is placed off-axis so there is no direct line of sight from the filament through the guiding hole to the detector.

5.2.2. Steering Coils

A pair of steering coils is used to deflect the electron beam via magnetic fields in the x- and z-direction (cf. Figure 5.9). Figure 5.11 shows a photograph of the steering coils. An enameled copper wire with 0.3 nm diameter is wound around a coil body made of stainless steel with a hole in the middle to guide the electron beam. Two independent coils with 80 windings per coil are wound. The coil body is screwed with 10 mm thick interposers directly onto the anode plate of the electron gun. A maximal current of 1 A can be applied to the coils creating a magnetic field perpendicular to the beam of $B_\perp = 2.8 \, \text{mT}$ which is sufficient to deflect the electrons across the entire detector and the copper plate for rate monitoring. Homogenous irradiation of the detector can be simulated by applying ramp signals with a high frequency to the steering coils with an arbitrary waveform generator[9]. The signal is

---

[8]Heinzinger electronic GmbH, Anton-Jakob-Strasse 4, D - 83026, Rosenheim
[9]Keysight 33500B Waveform Generator

(a) Close-up of the Filament
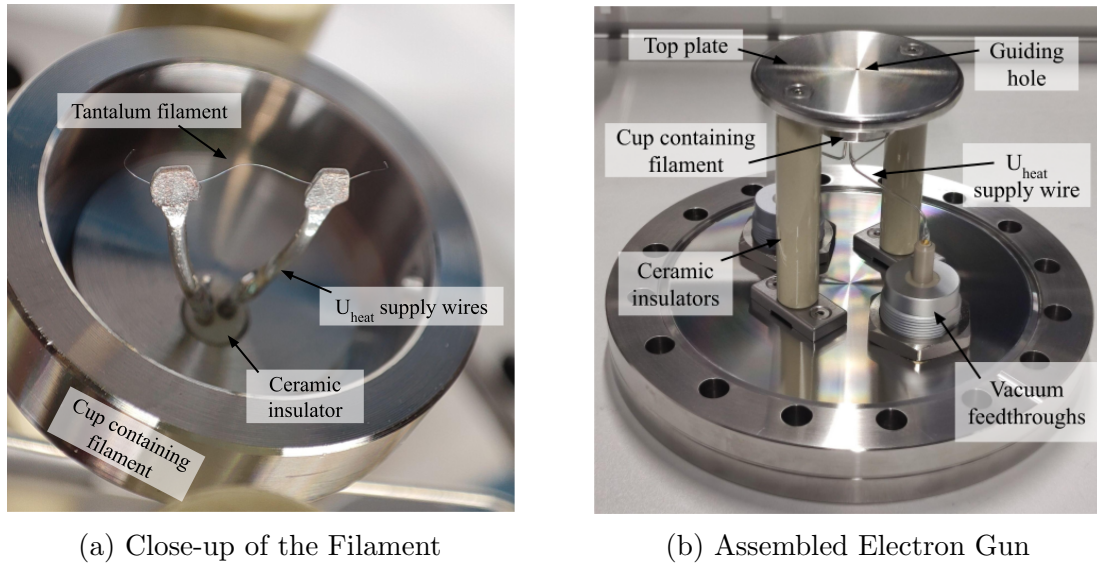

(b) Assembled Electron Gun

Figure 5.10: **Photographs of the Electron Gun Components**
(a): Close-up of the filament squeezed between two wires. The wires supply a heating current to the filament allowing electrons inside the filament to gain enough thermal energy to overcome the work function of tantalum and escape from the surface. The wires are guided inside the stainless steel cup through a ceramic insulator.
(b): Photograph of the assembled electron gun. The filament sits within a stainless steel cup screwed onto the top plate. The heating current is forwarded to the filament by high-voltage vacuum feedthroughs and the supply wires. Generated electrons leave the cup via a 3 mm large guiding hole. The electron gun is installed on a flange and isolated against the vacuum chamber via ceramic insulators.
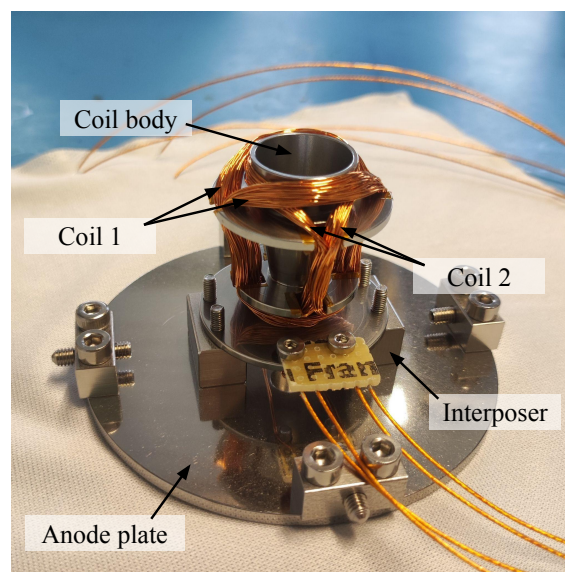
Figure 5.11: **Photograph of the Steering Coils**
Two independent copper coils are wound around a stainless steel coil body to guide the beam in x- and z-direction. The coils are installed on top of the anode plate.

processed with a custom-designed dual-channel power amplifier and guided inside the vacuum via a D-Sub connector.

5.2.3. Rate Monitoring

Radiation damage studies in this thesis will be performed with total beam electron rates on the order of $10^9\,\mathrm{e^-/s}$. These rates are too high to be resolved by the TRIS-TAN module itself. Therefore, rate monitoring is realized with a 0.03 mm thick $70 \times 70\,\mathrm{mm}^2$ copper plate. It is installed in the arm of the vacuum cross to the left of the detector seen from the electron gun (cf. figure 5.12), partially covering the upper left edge. Consequently, the pixels behind are shielded and, therefore, excluded from the analysis.
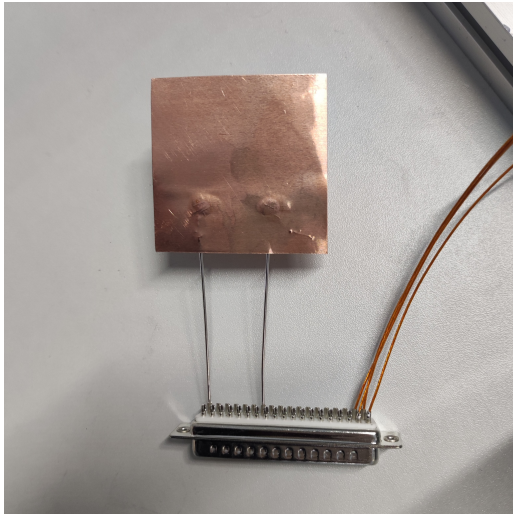
(a) Photograph of Copper Plate   (b) Position of Copper Plate
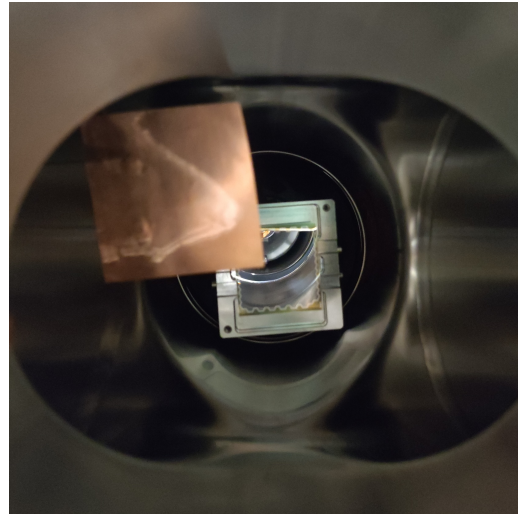
Figure 5.12: **Photographs of the Copper Plate for Rate Monitoring**
(a): Photograph of the copper plate with soldered wires inside a D-Sub connector.
(b): Photograph of the copper plate installed in the left arm of the vacuum cross next to the detector. The angle of view is from the perspective of the electron gun. The copper plate covers the left upper edge of the detector.

The steering coils can be used to deflect the beam onto the copper plate during the radiation damage measurements, where it generates a current I_{CP} that is proportional to the number of incoming electrons. The current is drained from the copper plate via two wires soldered onto the plate and guided outside of the vacuum via a D-Sub connector. There, it is read out with a Keithley multimeter[10] with a minimal current sensitivity of 0.1 nA. The current is correlated to the electron rate in counts per second (cps) of the beam via the elementary charge $e \approx 1.6 \cdot 10^{-19}\,\mathrm{As}$:

$$1\,\mathrm{A} = 1/e \ \mathrm{cps} = 6.25 \cdot 10^{18}\,\mathrm{cps}, \tag{5.3}$$

---

[10]Keithley DMM6500 6.5 Digit Multimeter

leading to a minimal detectable rate of 625 Mcps. It is assumed that approximately 30 % of the incoming electrons scatter back from the plate's surface [60]. Therefore, the rate inferred from the current read out at the multimeter is smaller than the true electron rate from the beam.

5.2.4. Electron Gun Comissioning

Several commissioning measurements were performed to characterize the electron gun, comprising a voltage-current curve, an electron rate scan, and rate stability tests.

Voltage-Current Curve

As a first test, the voltage-current curve of the filament was measured. To this end, the filament's heating voltage supply wires are directly connected to a power supply via the vacuum feedthroughs. With this setup, the heating current I_{heat} through the filament can be varied with the power supply, and the corresponding heating voltage was recorded. This process was repeated three times to check for consistency. Figure 5.13a shows the resulting voltage-current curves. Increasing the heating current leads to higher power dissipation through the filament and an increase in filament temperature. The observed non-linear behavior is expected due to the temperature dependency of the resistance of the tantalum filament. The different curves largely overlap, demonstrating that the resistance of the filament changes consistently with temperature and proving stable conditions between the measurements. This provides a good basis for stable electron gun operation.

Electron Rate Scan

A systematic electron rate scan has been performed to measure the correlation between the heating current and the electron rate. Therefore, the current induced on the copper plate is measured for varying heating voltages and converted into the corresponding electron rate R (corrected for 30 % backscattering). This rate scan is performed for three different acceleration voltages $U_{acc} \in [5\,\text{kV}, 10\,\text{kV}, 15\,\text{kV}]$. To check for consistency, the rate was scanned by increasing the heating voltage from 0 to 2.1 V and subsequently decreasing it from 2.1 V downwards again. Figure 5.13b shows the resulting curves. The x-axis is given in terms of U_{bat} since the heating voltage is now set via the battery box, which introduces a $10\,\Omega$ resistance between the filament and the voltage supply. Therefore, U_{bat} is related to U_{heat} via $U_{bat} = (U_{heat}/I_{heat} + 10\,\Omega) \cdot U_{heat}$. As expected, increasing the heating voltage leads to an exponential increase in electron emission according to Richardson's law (cf. Equation 5.2). Additionally, higher acceleration voltages guide more electrons towards the copper plate and accordingly increase the measured current at the

plate I_{CP}. However, between $10\,\text{kV}$ and $15\,\text{kV}$ the rate does not increase anymore. This indicates that all electrons are already guided onto the copper plate with an acceleration voltage of $10\,\text{kV}$. This electron rate scan showed that the desired beam electron rates in the order of $10^9\,\text{e}^-/\text{s}$ can be easily reached with this electron gun.
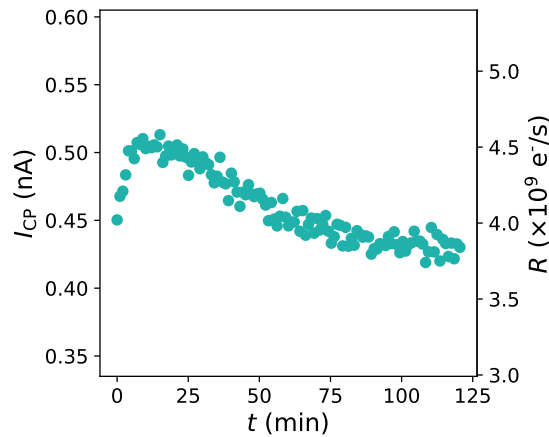
Rate Stability

As a final test, the electron gun was subjected to a rate stability test. In this measurement series, $15\,\text{keV}$ electrons were shot onto the copper plate for two hours. The heating voltage was set to $U_{\text{bat}} = 1.8\,\text{V}$ which leads to a current on the plate of around $I_{CP} = 0.45\,\text{nA}$. The current on the plate was read out once every minute. Figure 5.13c shows the measured current and the corresponding rate R (corrected for $30\,\%$ backscattering) over time t. The electron gun demonstrates a stable performance over two hours at a mean rate of $\overline{R} = 4.1 \cdot 10^9\,\text{e}^-/\text{s}$ with a standard deviation of $\sigma = 0.16 \cdot 10^9\,\text{e}^-/\text{s}$ which corresponds to a coefficient of variation of $CV = 6\,\%$. This stability indicates that monitoring the rate every five minutes during the radiation damage measurements is sufficient.
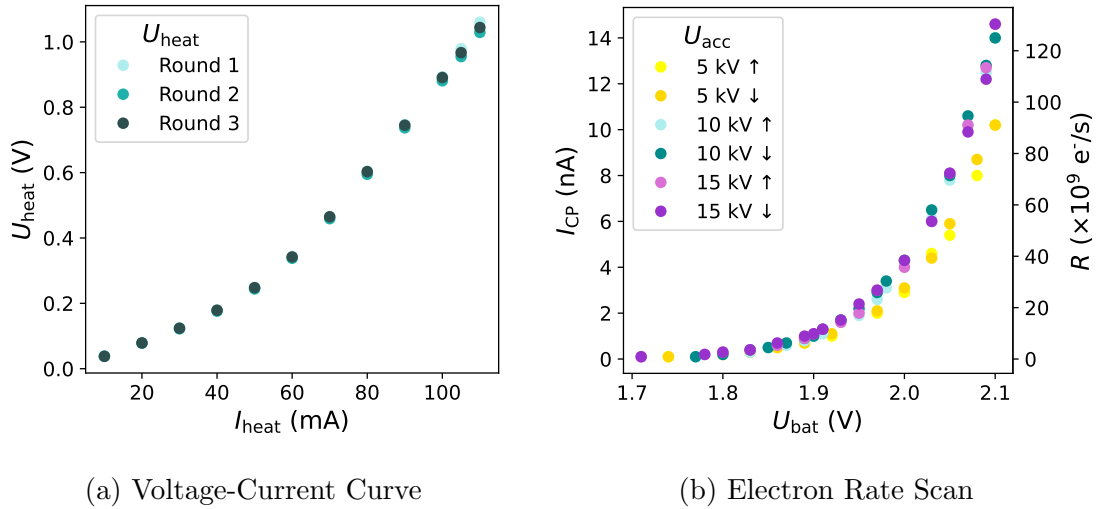
(a) Voltage-Current Curve

(b) Electron Rate Scan

(c) Rate Stability

Figure 5.13: **Electron Gun Commissioning Plots**
(a): Voltage-current curve showing a non-linear behavior of the heating voltage when increasing the heating current due to the temperature dependency of the filament's resistance. Several rounds were performed to check reliability.
(b): Electron rate scan demonstrating an exponential increase of the current on the copper plate for increasing heating voltages. To check consistency, the rate was scanned for increasing (light colors) and decreasing (dark colors) voltages.
(c): Rate stability test over two hours proving a largely stable electron rate with a mean of $\overline{R} = 4.1 \cdot 10^9 \, e^-/s$ for a heating voltage of $U_{bat} = 1.8 \, V$.

6. Radiation Damage Investigation

In this chapter, the findings from the radiation damage investigations conducted in this thesis are discussed. In Section 6.1, the measurement approach is outlined including the detector irradiation, rate monitoring, and three performance control measurements. Following this, the initial detector performance is presented in Section 6.2, which serves as a baseline for evaluating radiation damage. The main experimental results are then presented in Section 6.3, covering the three performance control measurements, i.e., the development of the detector's performance with electrons and X-rays, as well as the leakage current after irradiation. Section 6.4 provides a recovery and consistency analysis to evaluate the stability of the caused damage. Finally, the chapter concludes with a summary of the found damage and its relevance to the sterile neutrino search with KATRIN in Section 6.5.

6.1. Measurement Approach

Investigating electron-induced radiation damage using the experimental setup described in Section 5 comprised three tasks. First, the detector was irradiated with a high number of electrons, while second, the electron rate was monitored using the copper plate. Third, the performance of the detector was checked to assess any degradation caused by irradiation. In the following, the individual tasks will be described in detail.

6.1.1. Detector Irradiation

The sterile neutrino search with KATRIN is planned to operate at an electron rate of 100 kcps per detector pixel [39]. Assuming a runtime of one year, this rate translates to a total of $3.15 \cdot 10^{12}$ electrons reaching each pixel. This large amount of electrons is needed to accumulate statistical sensitivity. To investigate the damage caused by one year runtime within a shorter timeframe, this quantity of electrons per pixel was delivered to the detector in less than ten hours. To analyze how the radiation damage evolves with increasing electron exposure, the irradiation was divided into five phases. After each phase, detector performance checks were performed to gain detailed information on the possible radiation damage after a certain load of electrons.

Irradiation Rate

To assess whether the electron exposure of one year of sterile neutrino search induces radiation damage to the detector in a reasonable time requires a high overall beam electron rate of $3.6 \cdot 10^9 \, \mathrm{e^-/s}$ corresponding to an irradiation rate per pixel in the order of $10^7 \, \mathrm{e^-/s}$. Irradiating the detector with this high rate in less than ten hours

raises the question of comparability with irradiating the detector with a lower rate of 100 kcps per pixel over one year. According to theoretical considerations presented in chapter 4, electron irradiation forms positive oxide charges and interface states in the interface between the entrance window and the silicon bulk of the detector, which influence the CCE. These defects are created by individual electron interactions with the detector material. Therefore, a higher irradiation rate is expected to accelerate the generation of damage but should not influence the severity of the damage for the same exposure. Nevertheless, if there is a relation between the produced damage and the irradiation rate, which leads to more damage for higher rates, this study can be considered conservative, providing an upper-bound estimate of potential radiation damage.

Irradiation Energy

In the sterile neutrino search, electron energies will reach up to the endpoint energy of tritium of $E_0 = 18.6\,\text{keV}$. Additionally, a post-acceleration of $20\,\text{kV}$ is planned, resulting in an energy range from about $20\,\text{keV}$ up to $38.6\,\text{keV}$. However, due to spatial limitations, the electron gun used in the study was designed to provide electrons with energies up to $15\,\text{keV}$ to avoid electric flashover. Thus, the detector was irradiated with monoenergetic $15\,\text{keV}$ electrons. The damage caused by $15\,\text{keV}$ electrons is not expected to differ significantly from damage caused by higher energetic electrons with energies up to $38.6\,\text{keV}$. While higher energies may accelerate damage formation, they remain low enough to induce only surface damage, which will saturate when the limited amount of oxide charges and interface states are created.

Irradiation Pattern

An inhomogeneous irradiation pattern was applied to irradiate only the left side of the detector with the steering coils, allowing for direct comparison between irradiated pixels on the left and non-irradiated pixels on the right. Figure 6.1 presents a pixel map showing the irradiation pattern. Since the upper left quarter of the detector is covered by the copper plate for rate monitoring, only the left lower quarter was irradiated. For simplicity, the electron rate was assumed to be homogeneously distributed across the left lower quarter comprising 40 pixels. For the chosen overall beam electron rate of $3.6 \cdot 10^9\,\text{e}^-/\text{s}$, this leads to an irradiation rate of $9 \cdot 10^7\,\text{e}^-/\text{s}$ per pixel. However, the irradiation pattern is not perfectly homogenous since the pixels in the middle of the irradiated area experience a higher electron rate than those at the border. Additionally, the irradiation pattern is not sharply focused on the irradiation area of the left lower quarter of the detector but extends beyond the 40 pixels. In the following, it is assumed that $30\,\%$ of the electron beam is not focused on the target area. Irradiating the detector pixels in the irradiation area with the total exposure of one year of sterile neutrino search in less than ten hours
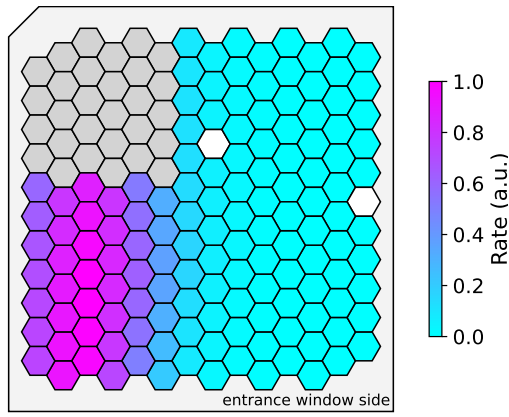
Figure 6.1: **Pixel Map of Irradiation Pattern**
The pixel map displays the irradiation pattern, with count rates represented in arbitrary units. The steering coils were adjusted to irradiate only the left side of the detector. Pixels covered by the copper plate in the upper left corner are marked in grey and excluded from the analysis. The two pixels marked in white were non-functional.

Phase	Correspondence	Total e$^-$	e$^-$ per phase	t (h)
1	1 Week	$8.10 \cdot 10^{10}$	$8.10 \cdot 10^{10}$	0.25
2	1 - 2 Months	$3.24 \cdot 10^{11}$	$2.43 \cdot 10^{11}$	0.75
3	3 - 4 Months	$9.72 \cdot 10^{11}$	$6.48 \cdot 10^{11}$	2
4	7 - 8 Months	$1.94 \cdot 10^{12}$	$9.72 \cdot 10^{11}$	3
5	1 Year	$3.15 \cdot 10^{12}$	$1.21 \cdot 10^{12}$	3.7

Table 6.1: **Irradiation Plan**
The irradiation plan comprises five phases, detailing the correspondence to the sterile neutrino search runtime, the total number of electrons delivered at the detector per pixel, the number of electrons to be irradiated in each phase per pixel, and the corresponding irradiation times at an electron rate of $9 \cdot 10^7 \, \mathrm{e^-/s}$ per pixel.

leads to the irradiation plan shown in Table 6.1. It comprises the exposures of the five irradiation phases and their equivalent runtimes of the sterile neutrino search with KATRIN.

6.1.2. Rate Monitoring

Since the TRISTAN detector is designed for an electron rate of 100 kcps per pixel, the detector readout cannot handle the high electron rates used in these studies. However, accurately tracking the number of electrons directed onto the detector is essential for quantifying the damage. Therefore, rate monitoring was realized with the copper plate described in Section 5.2.3. The electron beam was deflected using the steering coils onto the copper plate for five seconds every five minutes to verify the electron rate. If the rate increased, it was turned down by manually decreasing

the heating voltage of the electron gun within these five seconds. A dedicated script logged the current through the copper plate, measured by a multimeter, once every second to reconstruct the total number of electrons irradiated onto the detector from the five-second snippets where the beam was guided onto the copper plate. Assuming 30% backscattering, the overall beam irradiation rate of $3.6 \cdot 10^9\,\mathrm{e^-/s}$ corresponds to a current of $0.4\,\mathrm{nA}$ on the copper plate.

6.1.3. Performance Control Measurements

The detector performance control measurements conducted after each irradiation phase consist of three checks. All three of them were performed with a cooled detector at $-35\,^\circ\mathrm{C}$.

Electron Performance

The first performance control measurement investigates changes in the electron performance by irradiating the detector homogeneously with $5\,\mathrm{keV}$ and $15\,\mathrm{keV}$ electrons for 15 minutes each. A low electron rate (in the order of $10^3\,\mathrm{e^-/s}$) was chosen during this performance control measurement to mitigate pileup effects on the measured spectrum. The behavior of the electron gun changed throughout the radiation damage measurements, leading to higher rates for the same heating voltages. Therefore, the rate varied between $0.9 \cdot 10^3\,\mathrm{e^-/s}$ and $8 \cdot 10^3\,\mathrm{e^-/s}$. The data is taken in list mode, i.e., only the timestamp, the reconstructed energy of the events, and the respective channel are saved.

As described in Section 4, the expected damage is located near the interface between the entrance window and the silicon bulk of the detector, where signal charges can recombine and thus be lost. The expected consequence of such surface damage on the electron performance would manifest itself in the spectrum of this electron control measurement as a peak shift of the main peak to lower energies and a more pronounced low-energy shoulder. Thereby, $5\,\mathrm{keV}$ electrons are expected to experience a larger impact than $15\,\mathrm{keV}$ electrons since lower-energy electrons will deposit a larger fraction of their total energy closer to the entrance window region where charge collection is incomplete. The energy resolution in FWHM is a good measure for quantifying such damage. Since surface damage leads to an asymmetric main peak, the FWHM cannot be determined by fitting a Gaussian function. Therefore, the FWHM is determined by first identifying the main peak of the spectrum and then performing linear interpolation to achieve finer resolution. The width at half the peak height is measured by locating the points on either side of the peak where the signal drops to half its maximum value.

X-ray Performance

Secondly, the X-ray performance is examined by measuring X-ray events coming from the ^{55}Fe source placed in front of the detector with a mean rate of 26 cps for 30 minutes as list mode data. The electron gun is switched off for these measurements. These datasets are also used to calibrate the electron measurements. The X-ray performance at the 5.9 keV of the K_α peak is not expected to be significantly impacted by surface damage since they deposit their energy deeper in the silicon bulk, far from the insensitive entrance window region. Therefore, the FWHM is determined here by performing a Gaussian fit. Nevertheless, if the leakage current significantly increases, it could be observed as a broadening of the K_α and K_β peak in the ^{55}Fe spectrum.

Leakage Current

As a third performance control measurement, the leakage current of the detector is checked by taking data in the waveform acquisition mode where 10 ms-long first stage waveform snippets are recorded. The leakage current creates ramps that are superimposed by events from the ^{55}Fe source. Its value is inferred from the slope of the ramps, excluding the events. To this end, waveform segments between reset pulses are linearly fitted, and the slope from each fit is extracted. The average slope across all segments parameterizes the leakage current in units of lsb per second. Radiation damage could increase the leakage current, resulting in a steeper slope. To convert the leakage current from lsb per second in amperes, the following conversion is used:

$$I_{\text{Leakage}}\,[\text{A}] = \frac{4 \cdot c_{\text{lsb}\to\text{eV}} \cdot e}{w_{\text{Si}}} \cdot I_{\text{Leakage}}\,[\text{lsb/ms}]. \tag{6.1}$$

The factor 4 stems from the DAQ software binning, $c_{\text{lsb}\to\text{eV}}$ is the conversion factor from lsb to eV derived from the initial X-ray calibration, e is the elementary charge and w_{Si} the average energy required in silicon to generate one electron-hole pair.

Additional Frost Layer

As described in Section 5.1.3, cooling the detector raises the problem of an additional frost layer extending the insensitive entrance window. Since the individual irradiation phases take up to 3.7 hours, the frost layer will occur and cannot be distinguished from surface damage caused by irradiation. Therefore, two sets of control measurements were performed after each irradiation phase. The first set was taken directly after the irradiation phases. Afterward, the detector was heated to 20 °C overnight, and a second set of control measurements was conducted the next morning directly after cooling the detector down again. This way, the additional layer

due to cooling was eliminated, and the degradation shown by those datasets taken after heating can be associated with radiation damage.

6.2. Initial Detector Performance

Prior to the first irradiation phase, initial datasets representing the electron and X-ray performance and the value of the leakage current were obtained. These serve as a reference for the comparison of the detector response after each phase.

6.2.1. Initial Electron Performance

Initially, the detector response to electrons at 5 keV and 15 keV is recorded. The detector's initial energy resolution can be derived from the energy spectra shown in Figure 6.2a and Figure 6.2c as the mean FWHM ($\overline{\text{FWHM}}$)[11] of all pixels. The main peaks are slightly asymmetric since electrons always lose energy in the insensitive entrance window region of the detector. The 5 keV electron peak is significantly shifted to lower energies since lower energy electrons experience higher energy loss in the insensitive entrance window region. Consequently, the peak is noticeably broader, indicating a worse energy resolution compared to 15 keV electrons. The mean energy resolution at 5 keV of 370 eV ($\overline{\text{FWHM}}$) and at 15 keV of 328 eV ($\overline{\text{FWHM}}$) confirm the worse energy resolution for low-energy electrons.

Figure 6.2b and Figure 6.2d present the energy resolution of each pixel in a pixel map for 5 keV and 15 keV respectively. Two pixels are non-functional, likely due to a connection issue. For 5 keV electrons, a worse energy resolution is observed at the border of the detector, deviating from the mean by up to 65 eV. Since this effect is not seen in the 15 keV measurement, it seems to be energy-dependent and might originate from irregularities in the entrance window. However, this has not been finally clarified. To investigate the radiation damage, the difference between the post-irradiation and the initial energy resolution will be taken, eliminating this issue.

The measurement at 15 keV reveals a slight degradation in energy resolution in the bottom right quarter of the detector. Individual pixels deviate by up to 26 eV from the mean energy resolution. This effect possibly arises due to light generated by the electron gun. While the electron beam can be guided and spread across the entire detector area with the steering coils, the photons emitted by the glowing filament of the electron gun cannot be deflected. Hence, they illuminate the detector in this area, resulting in a degraded energy resolution.

---

[11]The energy resolution is extracted for each pixel and then averaged.
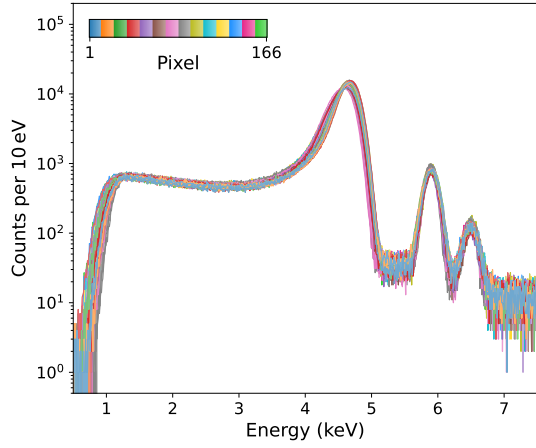
(a) Initial Energy Spectra at 5 keV
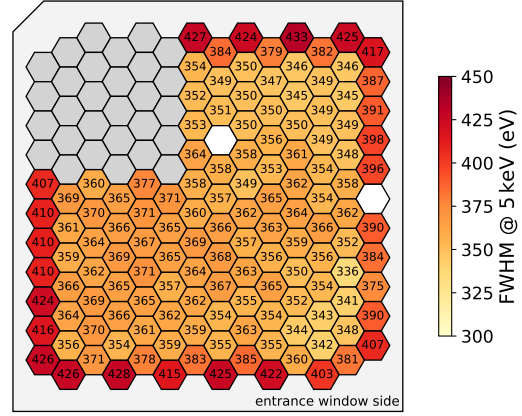
(b) Initial Energy Resolution at 5 keV
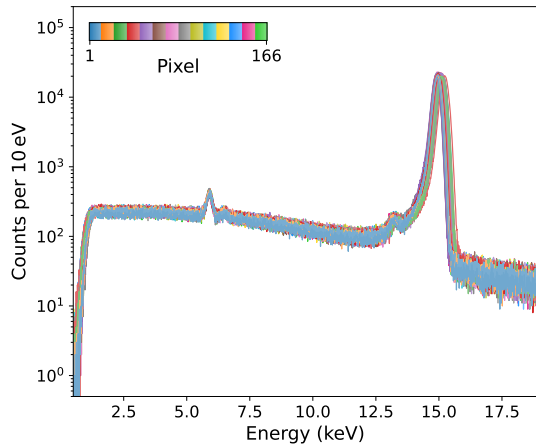
(c) Initial Energy Spectra at 15 keV
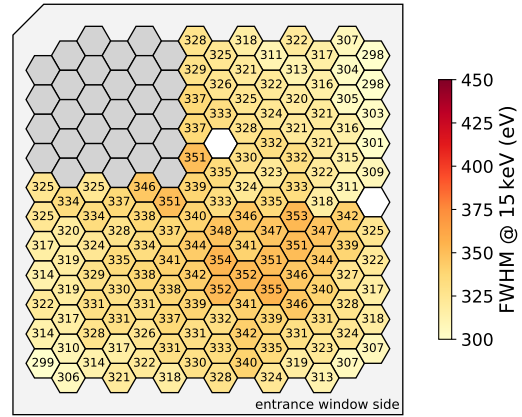
(d) Initial Energy Resolution at 15 keV

Figure 6.2: **Initial Electron Performance**
(a) and (c): Energy spectra for all pixels of the initial electron measurement for 5 keV and 15 keV respectively. The X-ray events from the permanently installed ^{55}Fe source appear in the spectra around 6 keV.

(b) and (d): Corresponding pixel maps of the energy resolution for 5 keV and 15 keV respectively. For 5 keV electrons a significantly degraded energy resolution along the border of the detector is observed. At 15 keV, the right lower quarter of the detector reveals slightly degraded energy resolution. Pixels marked in grey represent the area where the copper plate covers the detector and are excluded from the analysis. The white pixels were non-functional.

6.2.2. Initial X-ray Performance

The energy spectra of the initial detector response to X-rays is shown in Figure 6.3a. The narrow K_α peak of the ^{55}Fe source yields a mean energy resolution of $163\,eV$ ($\overline{FWHM}$). The energy resolution for X-rays is higher than for electrons, as X-rays are unaffected by the insensitive entrance window region. Figure 6.3b demonstrates uniform energy resolution across all pixels in a pixel map representing the energy resolution. This initial X-ray dataset was used to calibrate each subsequent electron dataset to avoid peak shifts due to varying calibration factors.

(a) Initial Energy Spectra of ^{55}Fe

(b) Initial Energy Resolution at K_α-peak
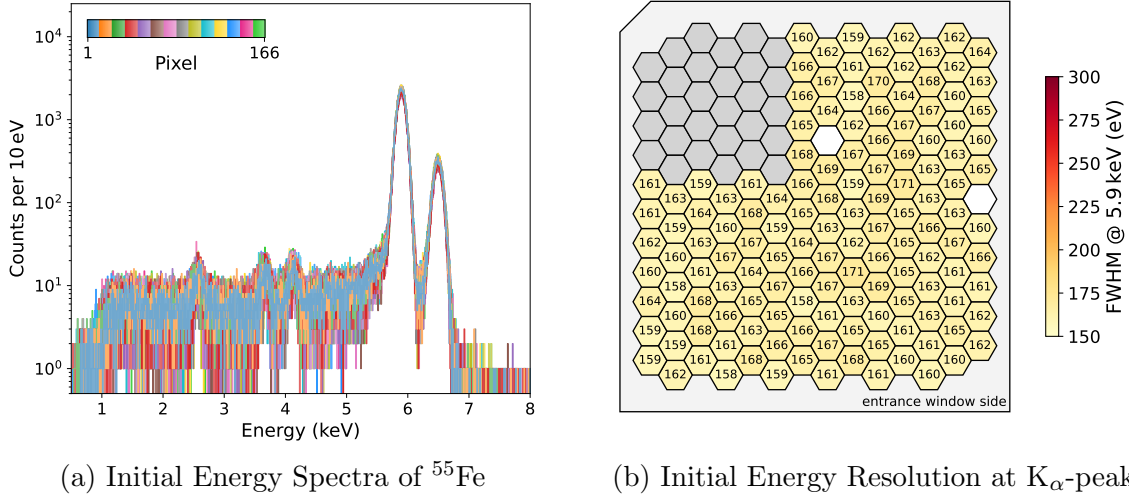
Figure 6.3: **Initial X-ray Performance**
(a): X-ray energy spectrum of all pixels with the prominent K_α and K_β peak at $5.9\,keV$ and $6.5\,keV$ respectively. At lower energies, various fluorescence lines of the source are visible, which are not of interest in this thesis.
(b): Corresponding energy resolution of each pixel at $5.9\,keV$ represented in a pixel map showing a homogenous detector performance. Pixels marked in grey represent the area where the copper plate covers the detector and are excluded from the analysis. The white pixels were non-functional.

6.2.3. Initial Leakage Current

The initial leakage current of the detector is deduced from waveforms from reset group 11 presented in Figure 6.4. Five events from the ^{55}Fe source appear as step-like increases superimposed on the baseline of the waveforms. Calculating the leakage current from the sequences between two reset pulses and excluding the ^{55}Fe events leads to a mean leakage current of $0.027\,pA$ across all pixels from reset group 11 for a cooled detector at $-35\,°C$.
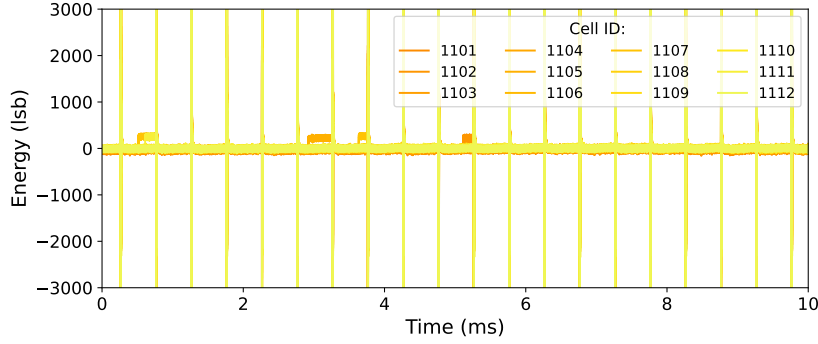
Figure 6.4: **Initial Waveforms from Reset Group 11**
Waveforms of pixels from reset group 11 from the initial dataset acquired before irradiation to determine the initial leakage current. The energy is not calibrated and thus given in lsb. Regular spikes every 0.5 ms correspond to the reset pulses. The slope between consecutive reset pulses indicates the leakage current. Five X-ray events from the ^{55}Fe source are visible as steplike increases along the baseline of the waveforms.

6.3. Results

The left side of the detector was irradiated in five phases according to the irradiation plan shown in Table 6.1. Rate monitoring with the copper plate was used to estimate the number of electrons incident on the detector. Figure 6.5 shows the recorded currents on the copper plate and the corresponding reconstructed electron rate. Each data point corresponds to the mean current measured during the 5-second rate monitoring phase. The larger drops in rate originate from manually turning down the heating voltage. As described in Section 6.1, it is assumed that only 70 % of the beam is delivered in the targeted area. At the same time, 30 % of the electrons scatter back from the copper plate during rate monitoring and are not detected. Therefore, both effects are expected to compensate for each other, and the measured current can be converted into the electron rate via Equation 5.3. Nevertheless, this is only a rough estimation of the rate reaching the irradiation area of the detector.

The rate tended to increase as the filament temperature rose over time. Consequently, the detector was irradiated with more electrons than stated in the irradiation plan. Table 6.2 summarises the reconstructed total number of electrons directed at the detector in each phase and updates the correspondences to the runtime of the sterile neutrino search with KATRIN. The total electron exposure after all five phases was $3.56 \cdot 10^{12}$ electrons, which can be correlated to roughly one year and two months of runtime.
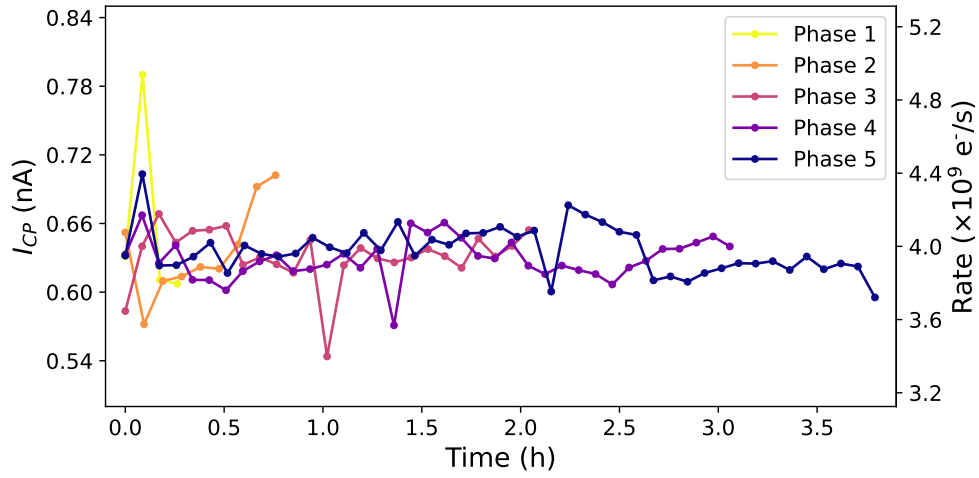
Figure 6.5: **Rate Monitoring of All Phases**
Measured current on the copper plate I_{CP} and corresponding rate during each irradiation phase.

Phase	Reconstructed total e$^-$	Correspondence
1	$1.23 \cdot 10^{11}$	2 Weeks
2	$3.92 \cdot 10^{11}$	1.5 Months
3	$1.13 \cdot 10^{12}$	4 Months
4	$2.22 \cdot 10^{12}$	9 Months
5	$3.56 \cdot 10^{12}$	14 Months

Table 6.2: **Reconstructed Exposure per Phase**
Reconstructed total exposure per pixel for each phase and corresponding equivalent runtime of the sterile neutrino search.

6.3.1. Electron Performance Post Irradiation

Figure 6.6 presents the energy spectra after each phase compared to the initial spectrum for 5 keV and 15 keV electrons. It is important to note that these datasets were taken the day after each irradiation phase. Heating the detector overnight removes the additional frost layer that occurs when the detector is cooled. Differences observed between the datasets taken directly after irradiation and those taken the following day, after heating the detector, can be attributed to the cooling layer. No additional time-dependent irradiation effects were detected. The left plot shows pixel 1308, located in the center of the irradiated left side of the detector. For comparison, the right plot displays pixel 0911 from the non-irradiated right half of the detector (cf. Figure 6.1). The spectra after each individual phase for all pixels can be found in the appendix A (cf. Figure A.1 and Figure A.2). The spectra of the irradiated pixel reveal a peak shift of the main peak towards lower energies, and the low-energy shoulder becomes more prominent for both electron energies after the irradiation. These features are typical for surface damage, consistent with the theory discussed in section 4. In contrast, the spectra of the non-irradiated pixel remain largely unchanged, confirming that this effect is caused by radiation.

The signs of surface damage appear already after the first irradiation phase, corresponding to around two weeks of sterile neutrino search ($\approx 1.23 \cdot 10^{11}$ electrons per pixel). Additionally, the damage saturates after phase 3, equivalent to roughly four months of runtime ($\approx 1.13 \cdot 10^{12}$ electrons per pixel). This saturation aligns with theoretical predictions, as surface damage is confined to the finite interface between the silicon bulk and the SiO_2 entrance window.

Comparing the 5 keV and 15 keV datasets shows that 5 keV electrons are significantly more affected by the surface damage than 15 keV electrons. This is expected since a lower-energy electron loses a higher fraction of its total energy in the surface region where the damage occurs. Table 6.3 summarizes the mean energy resolution of the irradiated area after each phase for both energies. The mean energy resolution in the irradiated area at 5 keV dropped significantly by 666 eV representing a worsening of 174 %. In contrast, at 15 keV it decreased by only 46 eV, corresponding to a much smaller reduction of 14 %. This reduction of energy resolution at 15 keV is an order of magnitude smaller than the degradation observed at 5 keV.

Figure 6.7 illustrates the reduction in energy resolution, calculated as the difference in energy resolution (ΔFWHM) between phase 5 and the initial dataset for each pixel at 5 keV and 15 keV. The absolute energy resolution after each phase for both energies can be found in the appendix A (cf. Figure A.3 and Figure A.4). The pixel maps show that only the irradiated pixels display a degradation in energy resolution,
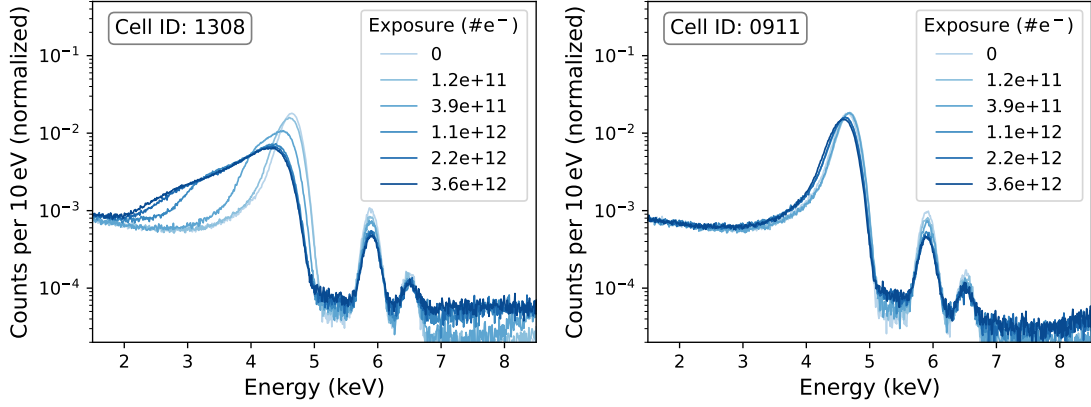
(a) Electron Spectra After Each Phase at $5\,\text{keV}$
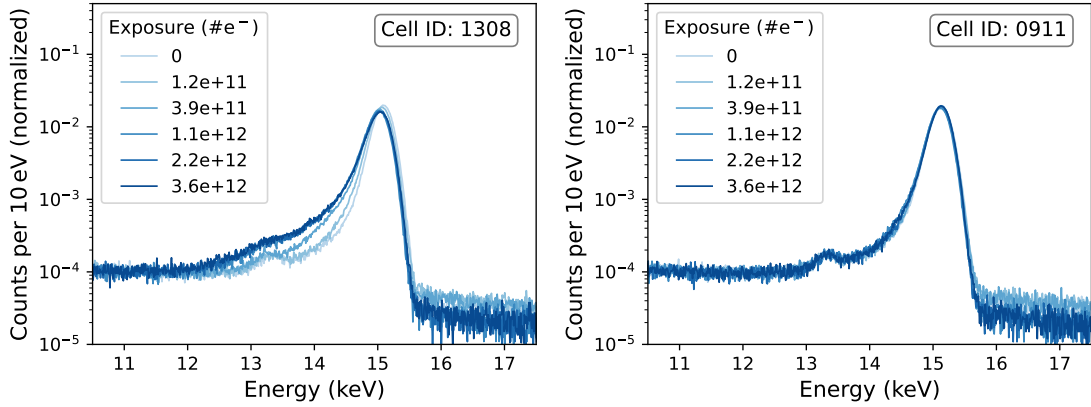
(b) Electron Spectra After Each Phase at $15\,\text{keV}$

Figure 6.6: Electron Spectra After Each Irradiation Phase at $5\,\text{keV}$ and $15\,\text{keV}$

(a) and (b): Electron spectrum at $5\,\text{keV}$ and $15\,\text{keV}$ respectively, after the exposure of each irradiation phase was distributed on the detector. The left plot shows data from an irradiated pixel, while the right plot corresponds to a non-irradiated pixel. For both energies typical signs of surface damage are visible in the spectra of the irradiated pixel, while the spectra in the non-irradiated pixel remain largely unchanged. The impact for $5\,\text{keV}$ electrons is significantly larger than for $15\,\text{keV}$ electrons.

Phase	**0**	**1**	**2**	**3**	**4**	**5**
$\overline{\textbf{FWHM}}$ **@** $5\,\text{keV}$ **(eV)**	383	437	660	1036	1001	1049
$\overline{\textbf{FWHM}}$ **@** $15\,\text{keV}$ **(eV)**	321	332	345	357	360	367

Table 6.3: Mean Energy Resolution After Each Phase

Mean energy resolution of the irradiated area (here defined as pixels from reset groups 13 and 14) after each phase for $5\,\text{keV}$ and $15\,\text{keV}$ electrons. Phase 0 corresponds to the initial dataset taken before irradiation.
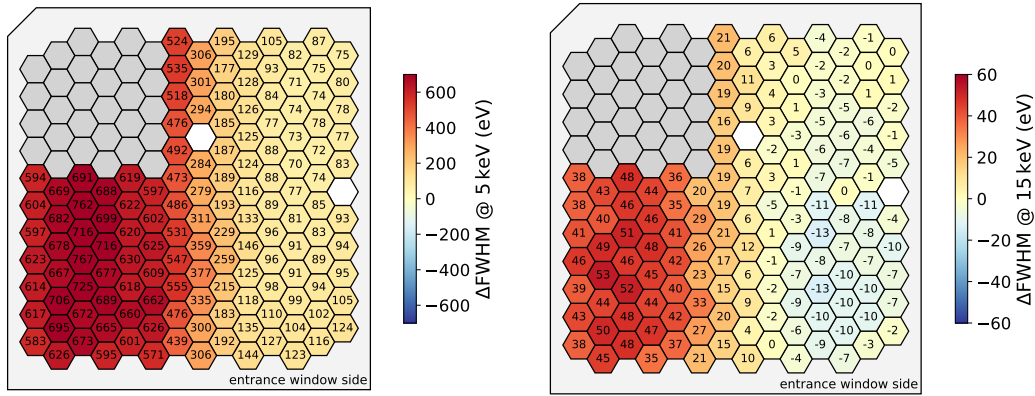
(a) Difference in Energy Resolution for 5 keV Electrons

(b) Difference in Energy Resolution for 15 keV Electrons

Figure 6.7: **Difference in Energy Resolution at** $5\,\text{keV}$ **and** $15\,\text{keV}$
(a) and (b): Pixel map showing the difference in energy resolution between the dataset taken after phase 5 and the initial dataset for the electron measurement at $5\,\text{keV}$ and $15\,\text{keV}$ respectively. Positive values represent a degradation of energy resolution. Pixels marked in grey represent the area where the copper plate covers the detector and are excluded from the analysis. The white pixels were non-functional. Note the different scaling of the color bar.
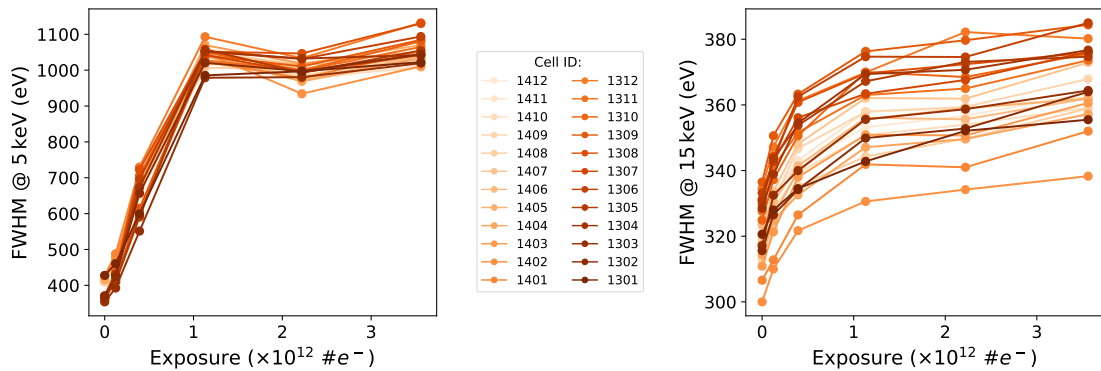
(a) Energy Resolution of Irradiated Pixels for 5 keV Electrons

(b) Energy Resolution of Irradiated Pixels for 15 keV Electrons

Figure 6.8: **Energy Resolution of Irradiated Pixels for** $5\,\text{keV}$ **and** $15\,\text{keV}$
(a) and (b): Energy resolution of irradiated pixels (here defined as reset group 13 and 14) for the electron measurement at $5\,\text{keV}$ and $15\,\text{keV}$ respectively, as a function of electron exposure per pixel. The qualitative response of the pixels to irradiation is uniform.

while non-irradiated pixels largely retain their original resolution or show only a minor decrease. Additionally, the irradiation pattern (cf. Figure 6.1) is represented in the pixel map of the energy resolution. Pixels experiencing more irradiation show a more severe degradation. This further confirms that the observed degradation is a direct result of irradiation. The 15 keV pixel map even reveals an improvement in energy resolution in the bottom right quarter of the detector. This can be explained by the light from the electron gun reaching this area. Throughout the irradiation phases, the performance of the electron gun changed, and with increasing measurement time, less heating voltage was required to achieve the same electron rates. Therefore, the heating voltage was lowered for the later irradiation phases, and consequently, less light was emitted. Since this light worsens the energy resolution, this reduction improved the resolution in the illuminated area during later phases.

To check whether the degradation is uniform across all pixels, Figure 6.8 displays the energy resolution of each irradiated pixel as a function of electron exposure. It shows that all irradiated pixels experience a worsening of the energy resolution during phases 1 to 3, corresponding to an exposure of up to $1.13 \cdot 10^{12}$ electrons, while the degradation saturates after phase 3. The initial datasets already exhibit a spread in energy resolution, likely due to the uneven light distribution from the electron gun. Pixels closer to the middle of the detector experience more light illumination, resulting in poorer energy resolution compared to those near the left edge. Slight variations in the slope of the energy resolution can be explained by the irradiation pattern. Pixels located in the center of the irradiation area experience a greater exposure, resulting in a worse energy resolution than those at the edges. Despite this, the qualitative response of the pixels to irradiation is uniform.

6.3.2. X-ray Performance Post Irradiation

Figure 6.9 presents spectra from X-ray performance check measurements conducted after each irradiation phase, compared to the initial dataset. Unlike electron measurements, X-ray measurements are not impacted by surface damage. The individual spectra after each phase align entirely. This is expected since X-rays penetrate deeper into the detector and deposit their energy in the detector bulk, away from the surface damage. The pixel map in Figure 6.9, showing the difference in energy resolution between the initial and the fifth-phase dataset, confirms that this alignment holds across all pixels and no degradation in energy resolution was caused by irradiation. These results indicate that the observed damage is limited to surface effects, with no impact on the detector bulk. Moreover, the X-ray data suggests that the leakage current did not significantly increase. Otherwise, peak broadening would be evident in the ^{55}Fe spectra. It is likely that the leakage current did increase, but cooling the detector to $-35\,^{\circ}\mathrm{C}$ effectively limits this rise.
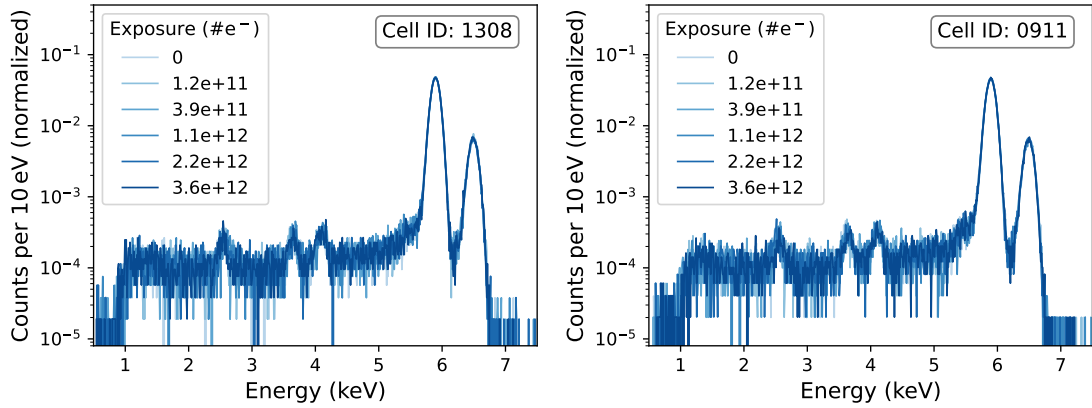
Figure 6.9: Spectra After Each Irradiation Phase of ^{55}Fe
Spectrum of ^{55}Fe after the exposure of each irradiation phase was distributed on the detector. The left plot displays the spectrum of an irradiated pixel, which shows no discernible difference from the spectrum in the right plot of a non-irradiated pixel. The individual irradiation phases are labeled with the respective number of electrons distributed on the detector per pixel.
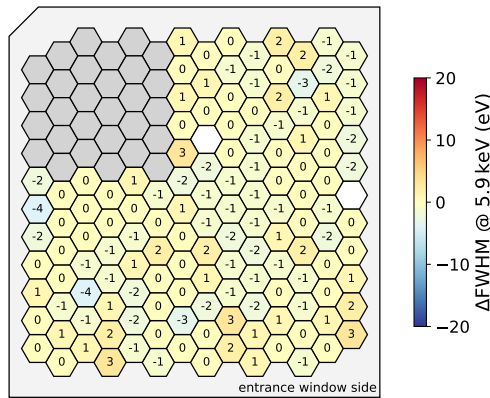
Figure 6.10: Difference in Energy Resolution at K_α Peak
Pixel map showing the difference in energy resolution at the K_α peak for the X-ray measurements, comparing the initial dataset with the dataset collected after phase 5. No degradation in energy resolution across the entire detector is observed. Pixels marked in grey represent the area where the copper plate covers the detector and are excluded from the analysis. The white pixels were non-functional.
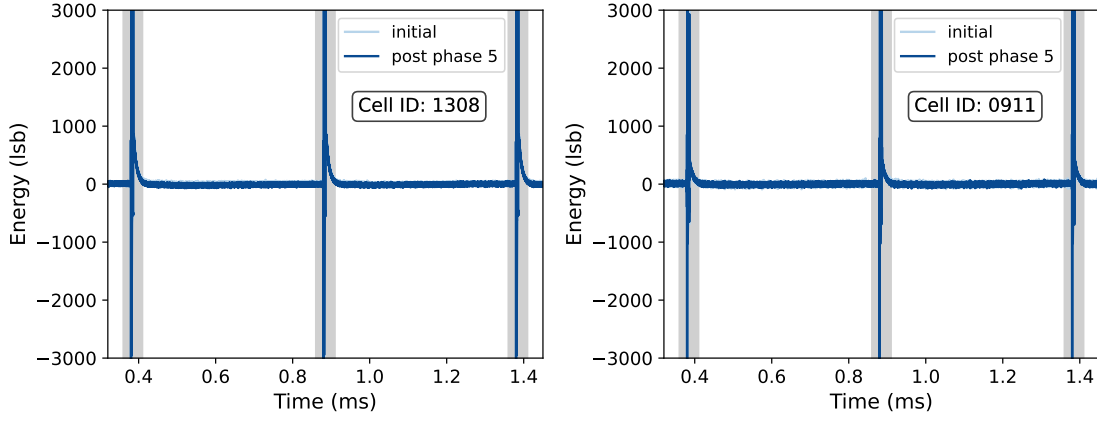
Figure 6.11: **Waveform Before and After Irradiation**
Raw waveform after irradiation phase 5 compared to the waveform of the initial dataset before irradiation. The left plot represents an irradiated pixel, while the pixel in the right plot was not irradiated. The waveforms overlap entirely in both plots. The spikes marked in grey correspond to the reset pulses. The leakage current can be deduced from the slope between two reset pulses.

6.3.3. Leakage Current Post Irradiation

In Figure 6.11, raw waveforms taken after irradiation phase 5 are compared to the initial waveforms before irradiation. The left plot shows an irradiated pixel, while the right plot is from a non-irradiated pixel. The waveforms before and after irradiation completely overlap in both plots. Consequently, no increase in leakage current is observed. This is also confirmed by the reconstructed leakage currents from those waveforms shown in Table 6.4. The slight differences between the values can be explained by the temperature uncertainty at the SDD chip, as it largely influences the leakage current. The temperature differed within the radiation damage measurements by a maximum of $1.5\,°C$. The leakage current investigation shows that even if radiation damage leads to an increase in leakage current, it is completely eliminated by cooling the detector.

Dataset	Irradiated		Non-Irradiated	
	Initial	**Post Phase 5**	**Initial**	**Post Phase 5**
$I_{\textbf{Leakage}}$ **(pA)**	0.020	0.016	0.027	0.024

Table 6.4: **Leakage Current Before and After Irradiation**
Leakage current I_{Leakage} of the initial dataset and after irradiation phase 5 for an irradiated pixel (Cell ID: 1308) and a non-irradiated pixel (Cell ID: 0911).
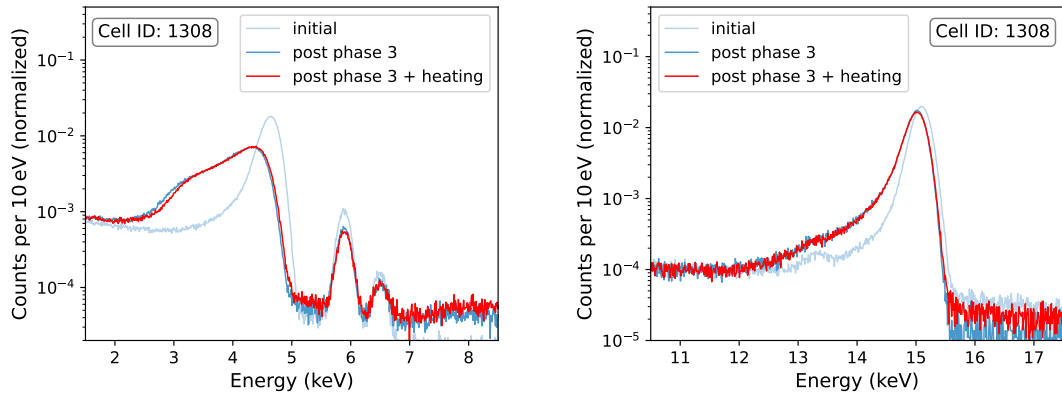
(a) 5 keV Electron Spectra after Heating

(b) 15 keV Electron Spectra after Heating

Figure 6.12: **Electron Spectra After Heating at** 5 keV **and** 15 keV
Energy spectra after heating the detector overnight compared to the spectra before heating and the initial spectra for 5 keV electrons in (a) and 15 keV electrons in (b). In both cases, the shown spectra correspond to an irradiated pixel, but no significant improvement is observed.

6.4. Recovery and Consistency Analysis

As described in Section 4.4, there are recovery mechanisms to restore the detector performance after radiation damage. However, they involve high temperatures and long waiting times, which can not be realized within this thesis. Nevertheless, post-irradiation consistency checks are performed to verify whether recovery effects occur under the given conditions. As significant recovery was not expected due to the limited heating and time constraints, these tests investigate the stability of the observed damage.

In the first consistency check, the detector was heated to its maximum technically possible temperature of 37 °C at the SDD chip overnight. This test was performed between irradiation phases 3 and 4. Figure 6.12 presents the spectrum taken after the heating period compared to those taken directly after the third irradiation phase and the initial dataset. Only a small improvement is observed in the post-heating spectrum of the 5 keV dataset. However, this improvement is likely caused by evaporating the additional frost layer from the detector through heating rather than by recovery from surface damage.

In the second check, the detector was left in air to rest for two months at room temperature. Figures 6.13a and 6.13b show the 5 keV and 15 keV electron spectra taken after the resting period compared to the dataset taken after phase 5 and the initial dataset. The shape of the main peak in the spectrum taken two months after the detector irradiation shows no significant difference from the main peak from the spectrum before the resting period. However, after the resting period,

the 15 keV electron spectrum displays a peak shift. This peak shift might result from a different setting of the acceleration voltage. It is possible, that for this recovery check measurement the high voltage supply was not precisely set to 15 keV but slightly lower resulting in this peak shift of the main peak. Another explanation would be that the environmental conditions in the setup were too different after two months. The K_α and K_β peaks of the ^{55}Fe source used for calibration are located around 6 keV, and therefore the calibration for 15 keV electrons is not as accurate as for 5 keV electrons. Consequently, environmental conditions can have a larger impact on the 15 keV spectra.

To have a more exact determination of changes in the electron performance of the detector independent from peak shifts due to the high-voltage setting or calibration, the difference in energy resolution pre and post-rest is determined. In Figure 6.13c and 6.13d, this difference is represented in a pixel map in percent at 5 keV and 15 keV respectively. While there is nearly no improvement at 15 keV, a minor improvement can be observed for the 5 keV dataset in the irradiated area, which is not present in the non-irradiated area. Therefore, this minor improvement likely stems from a slight recovery of the damage. This recovery only being visible in the 5 keV dataset is expected since lower-energy electrons are more affected by surface damage and, therefore, also more sensitive to the reduction of surface damage. Overall, the improvement after two months of rest is limited to a maximum of 10 % at 5 keV and 3 % at 15 keV. Due to these only minor improvements, it can be assumed that radiation damage stays mostly stable for the given conditions.

6.5. Impact on the Sterile Neutrino Search with KATRIN

The investigations conducted in this thesis demonstrate that the TRISTAN detector module experiences measurable radiation damage when exposed to electron irradiation. Electron performance check measurements revealed a degradation in energy resolution correlated to increased electron exposure. The damage is evident in the electron spectra as a shift of the main peak towards lower energies and a more pronounced low-energy shoulder, both characteristic indicators of surface damage. In irradiated pixels, the energy resolution for 15 keV electrons degrades by 14 % from 321 eV to 367 eV. The irradiated pixels show qualitatively similar responses to the irradiation, which is crucial for accurately considering the damage in the analysis. Since the damage is already observed after two to three weeks of sterile neutrino search with KATRIN, frequent (for example weekly) calibrations will be necessary to precisely track performance changes. Additionally, an important finding is the saturation of the damage appearing after the third irradiation phase, equivalent to approximately five months of sterile neutrino search with KATRIN. This saturation effect could potentially be exploited to achieve a more stable detector performance.
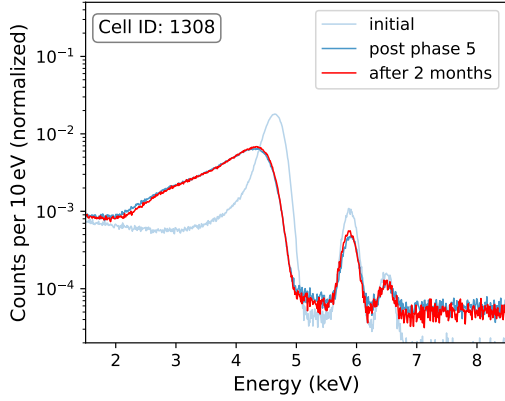
(a) Electron Spectra after Resting for 2 Months at 5 keV
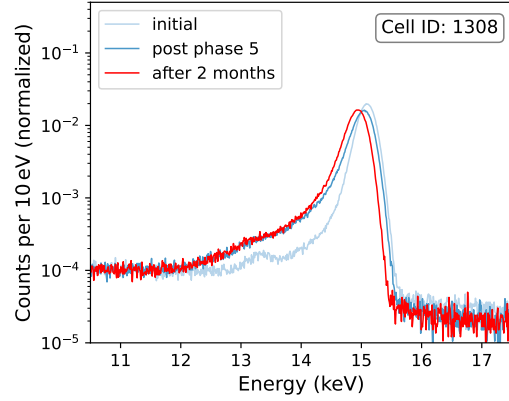
(b) Electron Spectra after Resting for 2 Months at 15 keV
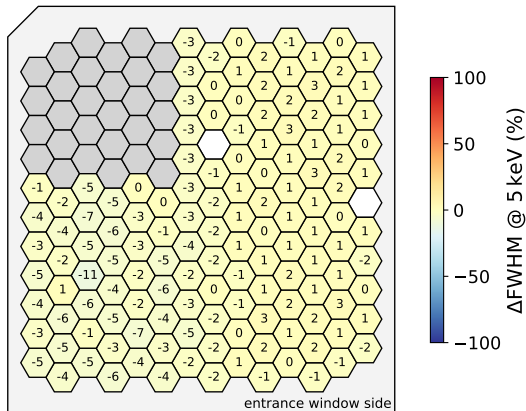
(c) Difference in Energy Resolution at 5 keV After Resting for 2 Months
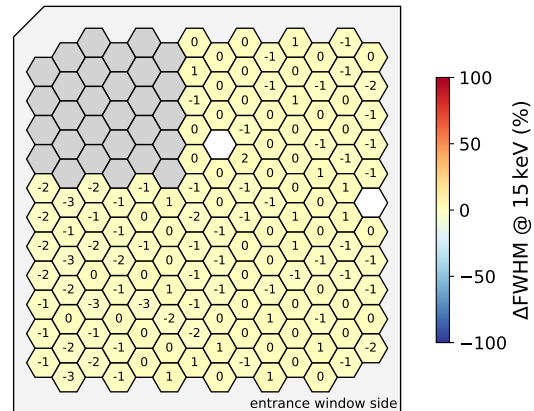
(d) Difference in Energy Resolution at 15 keV After Resting for 2 Months

Figure 6.13: **Electron Performance after Resting for Two Months**
(a) and (b): Electron spectra after resting, compared to spectra taken following irradiation phase 5 and the initial measurement, for 5 keV and 15 keV, respectively. No significant improvement is observed. At 15 keV a peak shift occurs due to different conditions in the vacuum setup after two months.
(c) and (d): Percentage change in energy resolution between the post-rest and pre-rest datasets for 5 keV and 15 keV, respectively. A negative value corresponds to an improvement in energy resolution. The observed improvement is only minor. Pixels marked in grey represent the area where the copper plate covers the detector and are excluded from the analysis. The white pixels were non-functional.

Comparing spectra from 5 keV electrons and 15 keV electrons confirms that higher-energy electrons are significantly less affected by surface damage. The damage in the 5 keV electron measurements seems severe. However, such low electron energies are not relevant to the sterile neutrino search with KATRIN. Nevertheless, using these low-energy electrons for radiation damage studies was reasonable to be most sensitive to surface damage. For the sterile neutrino search, it is important to highlight the planned Post Acceleration (PA) of 20 keV. Between the Main Spectrometer and the TRISTAN detector, the electrons will be accelerated, leading to an energy range of approximately 20 keV to 40 keV. In this energy range, the findings of this thesis strongly suggest that the energy resolution worsens by less than the measured 14 % at 15 keV. However, further measurements should be conducted to fully assess the damage at these higher energies.

While the electron performance is degraded by radiation, the X-ray performance remains unaffected. This confirms that only surface damage is caused. Moreover, the unchanged X-ray performance implies that the leakage current did not significantly increase. The raw waveforms, which allow for a more detailed analysis of leakage current, also show no increase in leakage current when the detector is cooled. Since the TRISTAN detector will be operated in a cooled state during the sterile neutrino search with KATRIN, no degradation from a radiation-induced, increased leakage current is expected.

A recovery analysis was conducted to investigate the stability of the damage. Due to setup limitations, the detector could only be heated to a maximum of 37 °C, where no performance improvement was observed. Furthermore, a two months exposure of the detector to air did not significantly restore the radiation damage effect. In the sterile neutrino search with KATRIN, short pauses in measurement on the timescale of hours or days will be necessary to maintain the setup. However, no significant recovery is expected during these pauses.

The above findings lead to the following approaches for managing radiation damage in the sterile neutrino search with KATRIN. First, the damage seemed to increase linearly before a saturation occurred after an exposure corresponding to five months of sterile neutrino search. These findings align with the expected damage from theoretical considerations. Therefore, simulations modeling the impact of the damage on the charge collection efficiency could allow for compensation of the damage in the analysis. Additional weekly calibration would keep track of changes in the detector performance and verify the consistency with the model. Second, it may be useful to exploit the saturation effect of the damage. By pre-irradiating the detector with the

equivalent exposure of five months of sterile neutrino search, where saturation was observed, the detector's performance could potentially be stabilized before starting the experiment. However, this approach would require to verify whether the energy resolution remains sufficient to achieve the target sensitivity and that the saturation effect continues under even higher electron exposures. Third, if degradation due to radiation damage turns out to be too severe to meet the target sensitivity, it may be necessary to replace the detector modules after the first six months. Thanks to the modular design of the TRISTAN detector, individual modules can be exchanged, allowing the installation of a new set of detector modules to restore the energy resolution.

These approaches attempt to mitigate the influence of radiation damage on the sensitivity of the sterile neutrino search with KATRIN. However, the significant difference between the performance for electrons at $5\,\mathrm{keV}$ and $15\,\mathrm{keV}$ suggests that it is reasonable to assume that radiation damage at the expected electron energies (between $20\,\mathrm{keV}$ and $40\,\mathrm{keV}$) remains small enough to still meet the target sensitivity. The worsening in energy resolution at $15\,\mathrm{keV}$ of $14\,\%$ is already an order of magnitude smaller than the worsening at $5\,\mathrm{keV}$. A worsening in energy resolution of less than $14\,\%$ likely has no major impact on the sensitivity.

7. Conclusion

The KArlsruhe TRItium Neutrino experiment (KATRIN) aims to determine the electron antineutrino mass with unprecedented precision by measuring the tritium β-decay spectrum near its endpoint. The neutrino mass campaign is foreseen to be completed by the end of 2025. Subsequently, the experimental setup of KATRIN will be modified to enable the search for sterile neutrinos. Sterile neutrinos are a minimal extension of the Standard Model (SM) of particle physics and a promising Dark Matter (DM) candidate if their mass lies in the keV range. Due to the active-to-sterile neutrino mixing, sterile neutrinos would leave a small imprint in the spectrum of the tritium β-decay. In contrast to the neutrino mass, the signature of the sterile neutrino could be located anywhere in the tritium spectrum. Hence, the measurement interval needs to be extended deeper into the spectrum, leading to exceedingly higher electron rates. To achieve the targeted sensitivity of the sterile neutrino search on the parts-per-million (ppm) level, an energy resolution below $300\,\mathrm{eV}$ (FWHM) at $20\,\mathrm{keV}$ is crucial. Therefore, a new detector system called TRISTAN is currently under development. It is based on the Silicon Drift Detector (SDD) principle, which provides excellent energy resolution at the expected high count rates of $100\,\mathrm{kcps}$.

SDDs were originally designed for X-ray spectroscopy, where fundamentally different interaction mechanisms are involved compared to electron spectroscopy. Theoretical considerations predict that irradiating SDDs with electrons causes surface damage, which decreases the Charge Collection Efficiency (CCE) and, thereby, the energy resolution of the TRISTAN detector system. However, maintaining a high energy resolution throughout the entire sterile neutrino search is mandatory to search for the small imprint of the sterile neutrino in the β-spectrum. Therefore, this thesis focused on the investigation of electron-induced radiation damage to a TRISTAN detector module.

To this end, a dedicated experimental setup consisting of a custom-designed electron gun with steering coils and a copper plate for rate monitoring was designed to irradiate a TRISTAN detector module with $15\,\mathrm{keV}$ electrons. This irradiation distributed the electron exposure expected from roughly one year of sterile neutrino search on one half of the detector in a much shorter time span of less than ten hours. The irradiation was divided into five phases, providing an overview of the radiation damage as a function of electron exposure. The detector performance was examined before and after each irradiation phase with three different control measurements. In these, the detector's electron performance, the X-ray performance, and the detector leakage current were investigated.

The irradiation of the detector revealed a degradation of the detector response to electrons. The damage manifests itself in the obtained electron spectra as a peak shift of the main energy peak towards lower energies as well as a more pronounced low energy shoulder. These effects are typical signs of irradiation-induced surface damage and were observed consistently across all irradiated pixels. Furthermore, the conducted measurements showed a decrease in energy resolution during the first phases until a saturation effect is observed after an exposure equivalent to around four months of sterile neutrino search ($\approx 1.13 \cdot 10^{12}$ electrons). The electron performance was investigated for $5\,\mathrm{keV}$ and $15\,\mathrm{keV}$ electrons, showing that higher-energy electrons are significantly less affected by surface damage than lower-energy electrons. While the energy resolution for $15\,\mathrm{keV}$ electrons decreased by $14\,\%$, the decrease at $5\,\mathrm{keV}$ was one order of magnitude higher. This emphasizes the importance of the intended Post Acceleration (PA) of $20\,\mathrm{kV}$ that would increase the electron energies in the sterile neutrino search up to $40\,\mathrm{keV}$. At these energies, the findings of this thesis predict a significantly lower impact of radiation damage on the energy resolution.

Validating the detector performance with X-rays showed that the response to photons remains unchanged. This confirms that only surface damage has occurred. Additionally, reconstructing the leakage current from raw waveforms showed no increase in leakage current for a cooled detector.

Measurements investigating the potential recovery of the damage showed that for the conditions in the sterile neutrino search with KATRIN, the damage is expected to remain stable. Nevertheless, it is essential to monitor changes in the detector performance due to radiation damage as well as possible recovery of the damage after measurement pauses with regular calibration.

The findings of this thesis are crucial for understanding the behavior of the TRISTAN detector under electron irradiation. They revealed that electron exposure does introduce surface damage to the SDDs. Understanding the impact of the damage on the CCE is important for accurately modeling the detector response to electrons, which is crucial for managing radiation damage in the sterile neutrino search with KATRIN.

A. Appendix

(a) Initial Electron Spectra

(b) Electron Spectra after Phase 1

(c) Electron Spectra after Phase 2

(d) Electron Spectra after Phase 3

(e) Electron Spectra after Phase 4

(f) Electron Spectra after Phase 5
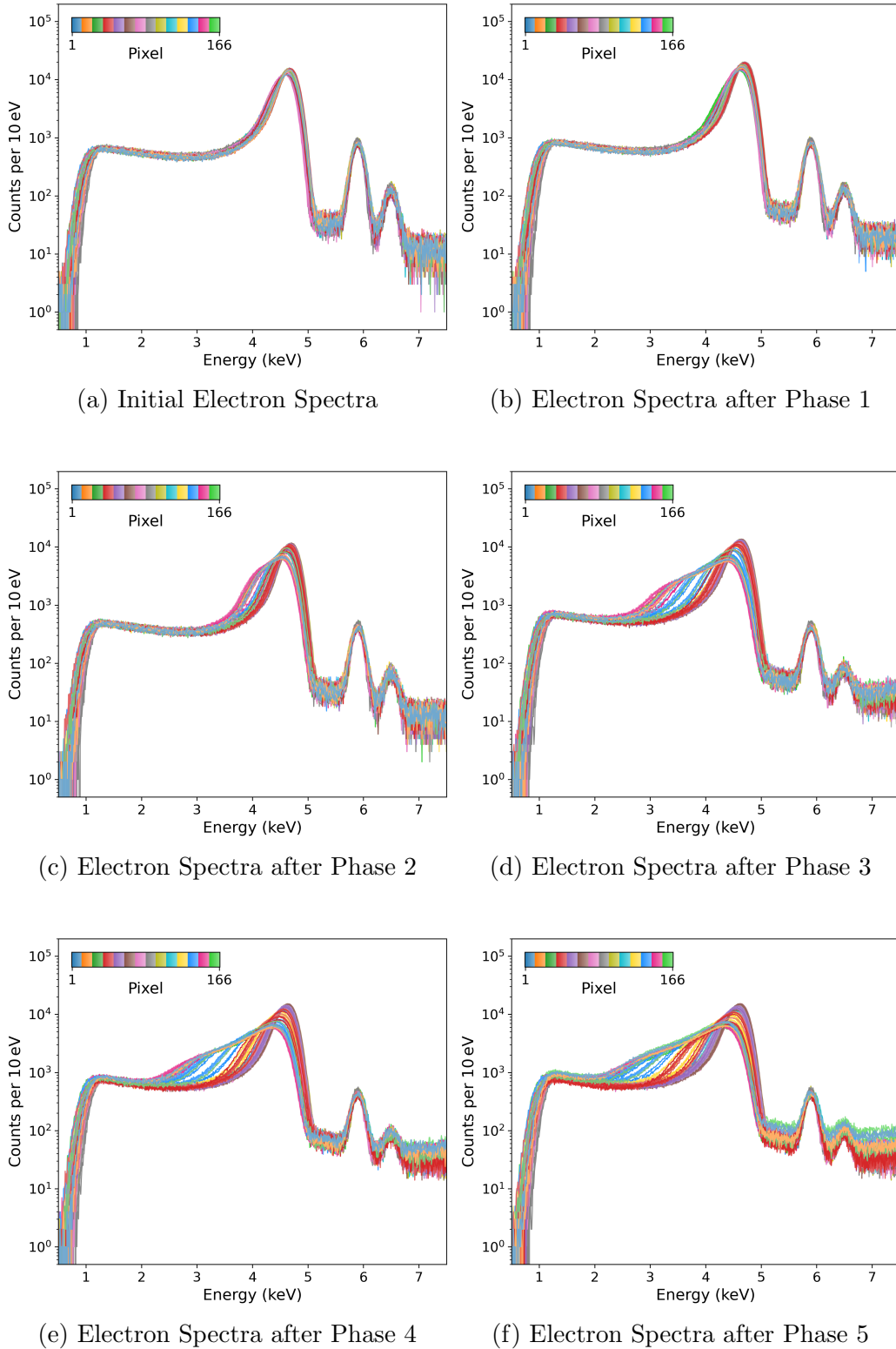
Figure A.1: **Electron Spectra of All Pixels at** $5\,\text{keV}$ **After Each Phase**
(a) to (f): Energy Spectra of $5\,\text{keV}$ electrons for all pixels after each irradiation phase. While irradiated pixels display typical signs of surface damage, non-irradiated pixels retain their original shape. The spectral distortions become more significant with increasing electron exposure.

(a) Initial Electron Spectra

(b) Electron Spectra after Phase 1

(c) Electron Spectra after Phase 2

(d) Electron Spectra after Phase 3

(e) Electron Spectra after Phase 4

(f) Electron Spectra after Phase 5
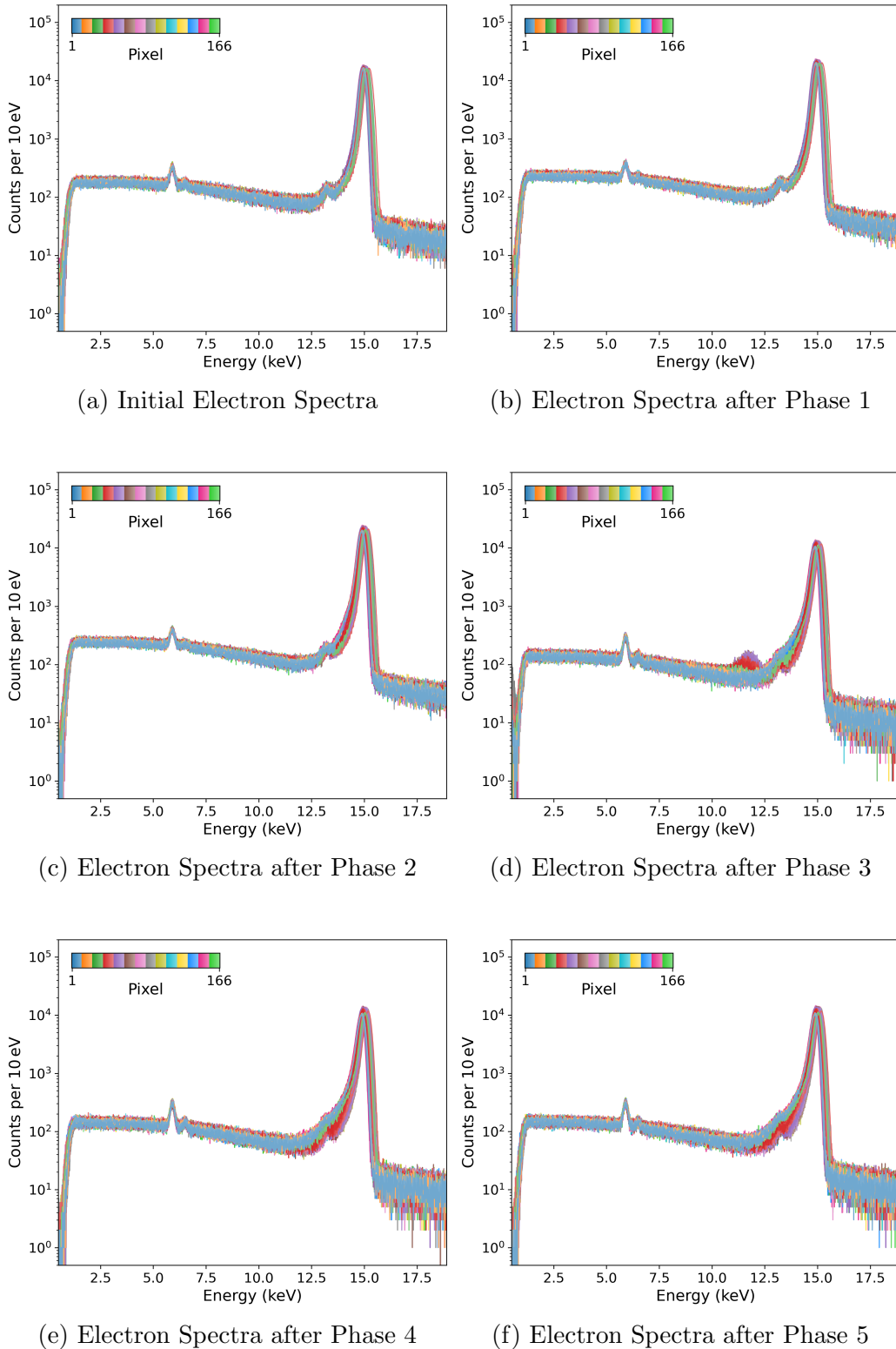
Figure A.2: **Electron Spectra of All Pixels at** $15\,\mathrm{keV}$ **After Each Phase**
(a) to (f): Energy Spectra of $15\,\mathrm{keV}$ electrons for all pixels after each irradiation phase. While irradiated pixels display typical signs of surface damage, non-irradiated pixels retain their original shape. The spectral distortions become more significant with increasing electron exposure.
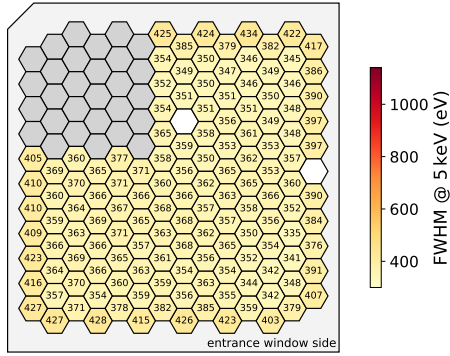
(a) Initial Energy Resolution
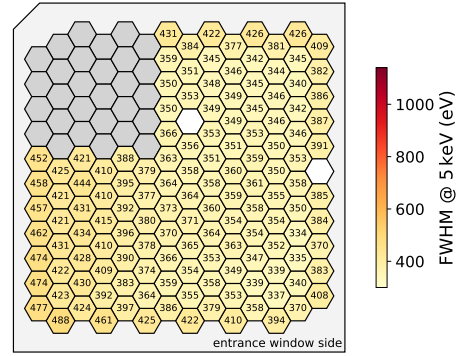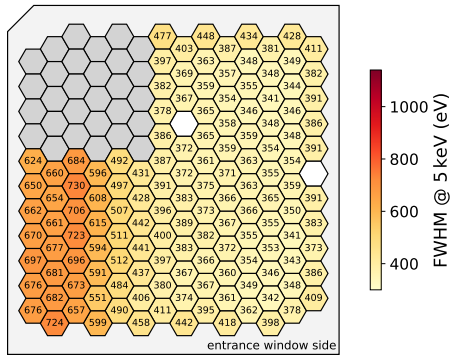
(b) Energy Resolution after Phase 1

(c) Energy Resolution after Phase 2
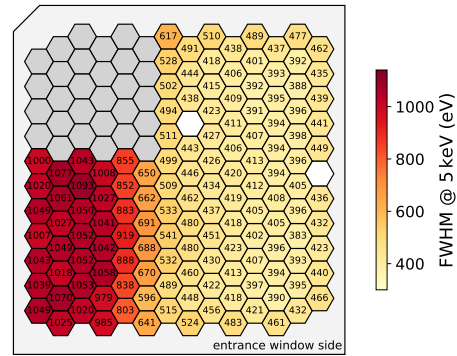
(d) Energy Resolution after Phase 3
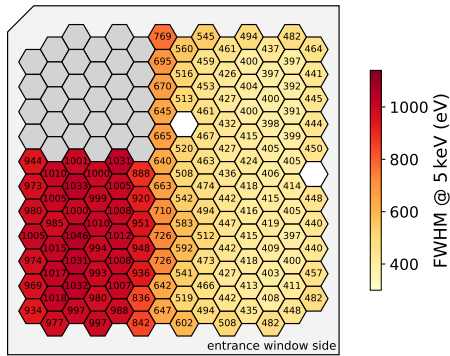
(e) Energy Resolution after Phase 4
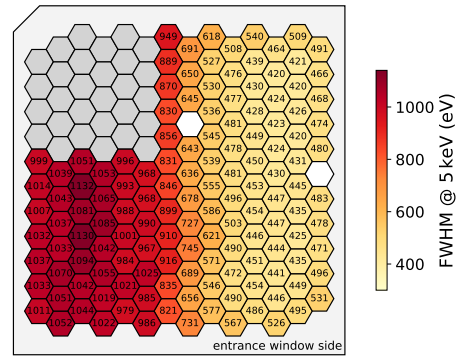
(f) Energy Resolution after Phase 5

Figure A.3: **Energy Resolution at** $5\,\mathrm{keV}$ **After Each Phase**
(a) to (f): Pixel map showing the energy resolution at $5\,\mathrm{keV}$ after each phase. Positive values represent a degradation of energy resolution. Pixels marked in grey represent the area where the copper plate covers the detector and are excluded from the analysis. The white pixels were non-functional.
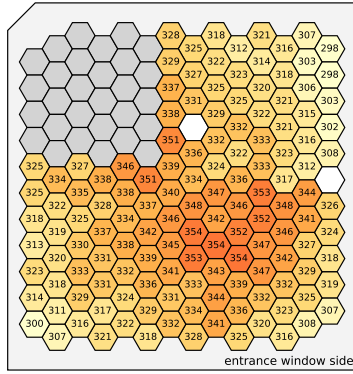
(a) Initial Energy Resolution
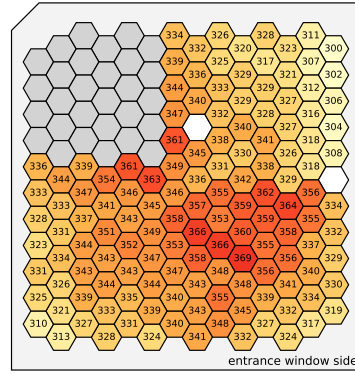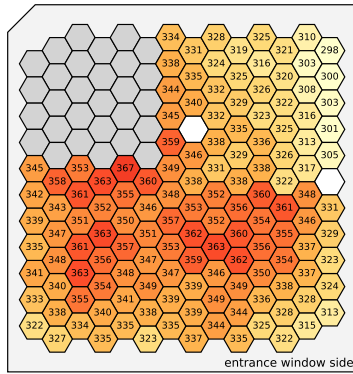
(b) Energy Resolution after Phase 1

(c) Energy Resolution after Phase 2
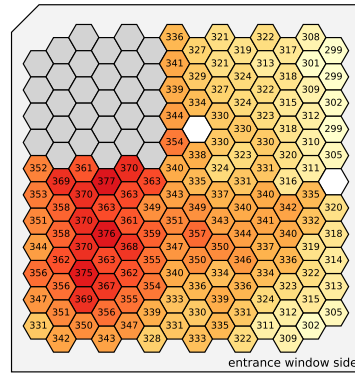
(d) Energy Resolution after Phase 3
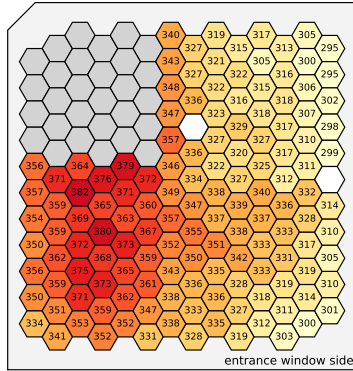
(e) Energy Resolution after Phase 4
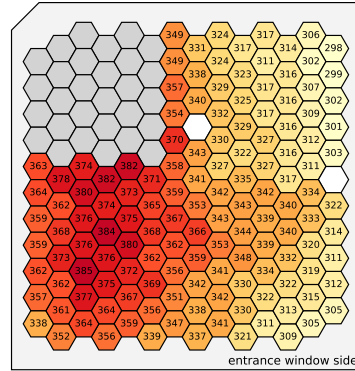
(f) Energy Resolution after Phase 5

Figure A.4: **Energy Resolution at** $15\,\mathrm{keV}$ **After Each Phase**
(a) to (f): Pixel map showing the energy resolution at $15\,\mathrm{keV}$ after each phase. Positive values represent a degradation of energy resolution. Pixels marked in grey represent the area where the copper plate covers the detector and are excluded from the analysis. The white pixels were non-functional.

70

References

[1] W. Pauli. *Offener Brief an die Gruppe der Radioaktiven bei der Gauvereins-Tagung zu Tübingen.* https://cds.cern.ch/record/83282/files/meitner_0393.pdf. 1930.

[2] C. L. Cowan et al. "Detection of the Free Neutrino: a Confirmation". In: *Science* 124.3212 (1956), pp. 103–104. DOI: 10.1126/science.124.3212.103. URL: https://www.science.org/doi/abs/10.1126/science.124.3212.103.

[3] G. Danby et al. "Observation of High-Energy Neutrino Reactions and the Existence of Two Kinds of Neutrinos". In: *Phys. Rev. Lett.* 9 (1 1962), pp. 36–44. DOI: 10.1103/PhysRevLett.9.36. URL: https://link.aps.org/doi/10.1103/PhysRevLett.9.36.

[4] K. Kodama et al. "Observation of tau neutrino interactions". In: *Physics Letters B* 504.3 (2001), pp. 218–224. ISSN: 0370-2693. DOI: https://doi.org/10.1016/S0370-2693(01)00307-0. URL: https://www.sciencedirect.com/science/article/pii/S0370269301003070.

[5] "Precision electroweak measurements on the Z resonance". In: *Physics Reports* 427.5 (2006), pp. 257–454. ISSN: 0370-1573. DOI: https://doi.org/10.1016/j.physrep.2005.12.006. URL: https://www.sciencedirect.com/science/article/pii/S0370157305005119.

[6] P. Anselmann et al. "GALLEX solar neutrino observations: complete results for GALLEX II". In: *Physics Letters B* 357.1 (1995), pp. 237–247. ISSN: 0370-2693. DOI: https://doi.org/10.1016/0370-2693(95)00897-T. URL: https://www.sciencedirect.com/science/article/pii/037026939500897T.

[7] M. Altmann et al. "Complete results for five years of GNO solar neutrino observations". In: *Physics Letters B* 616.3 (2005), pp. 174–190. ISSN: 0370-2693. DOI: https://doi.org/10.1016/j.physletb.2005.04.068. URL: https://www.sciencedirect.com/science/article/pii/S0370269305005149.

[8] A. I. Abazov et al. "Search for neutrinos from the Sun using the reaction $^{71}Ga(\nu_e,e^-)^{71}Ge$". In: *Phys. Rev. Lett.* 67 (24 1991), pp. 3332–3335. DOI: 10.1103/PhysRevLett.67.3332. URL: https://link.aps.org/doi/10.1103/PhysRevLett.67.3332.

[9] C. Arpesella et al. "First real time detection of 7Be solar neutrinos by Borexino". In: *Physics Letters B* 658.4 (2008), pp. 101–108. ISSN: 0370-2693. DOI: https://doi.org/10.1016/j.physletb.2007.09.054. URL: https://www.sciencedirect.com/science/article/pii/S0370269307011732.

[10]   B. Pontecorvo. *Mesonium and Antimesonium*. 1957. URL: http://jetp.ras.ru/cgi-bin/dn/e_006_02_0429.pdf.

[11]   Carlo Giunti. "THEORY OF NEUTRINO OSCILLATIONS". In: *Particle Physics in Laboratory, Space and Universe*. DOI: 10.1142/9789812702074_0005. URL: https://www.worldscientific.com/doi/abs/10.1142/9789812702074_0005.

[12]   M. Tristram et al. "Cosmological parameters derived from the final Planck data release (PR4)". In: *Astronomy & Astrophysics* 682 (2024). ISSN: 1432-0746. DOI: 10.1051/0004-6361/202348015. URL: http://dx.doi.org/10.1051/0004-6361/202348015.

[13]   W. H. Furry. "On Transition Probabilities in Double Beta-Disintegration". In: *Phys. Rev.* 56 (12 1939), pp. 1184–1193. DOI: 10.1103/PhysRev.56.1184. URL: https://link.aps.org/doi/10.1103/PhysRev.56.1184.

[14]   S. et al. Abe. "Search for the Majorana Nature of Neutrinos in the Inverted Mass Ordering Region with KamLAND-Zen". In: *Physical Review Letters* 130.5 (2023). ISSN: 1079-7114. DOI: 10.1103/physrevlett.130.051801. URL: http://dx.doi.org/10.1103/PhysRevLett.130.051801.

[15]   M. Aker et al. *Direct neutrino-mass measurement based on 259 days of KATRIN data*. 2024. arXiv: 2406.13516 [nucl-ex]. URL: https://arxiv.org/abs/2406.13516.

[16]   Lisa Schlüter. "Neutrino-Mass Analysis with sub-eV Sensitivity and Search for Light Sterile Neutrinos with the KATRIN Experiment". en. PhD thesis. Technische Universität München, 2022, p. 211. URL: https://mediatum.ub.tum.de/1661391.

[17]   A. Aguilar et al. "Evidence for neutrino oscillations from the observation of $\overline{\nu}_e$ appearance in a $\overline{\nu}_\mu$ beam". In: *Phys. Rev. D* 64 (11 2001), p. 112007. DOI: 10.1103/PhysRevD.64.112007. URL: https://link.aps.org/doi/10.1103/PhysRevD.64.112007.

[18]   A. A. Aguilar-Arevalo et al. "Significant Excess of Electronlike Events in the MiniBooNE Short-Baseline Neutrino Experiment". In: *Phys. Rev. Lett.* 121 (22 2018), p. 221801. DOI: 10.1103/PhysRevLett.121.221801. URL: https://link.aps.org/doi/10.1103/PhysRevLett.121.221801.

[19]   W Hampel et al. "Final results of the 51Cr neutrino source experiments in GALLEX". In: *Physics Letters B* 420.1 (1998), pp. 114–126. ISSN: 0370-2693. DOI: https://doi.org/10.1016/S0370-2693(97)01562-1. URL: https://www.sciencedirect.com/science/article/pii/S0370269397015621.

[20] J. N. Abdurashitov et al. "The Russian-American Gallium Experiment (SAGE) Cr Neutrino Source Measurement". In: *Phys. Rev. Lett.* 77 (23 1996), pp. 4708–4711. DOI: 10.1103/PhysRevLett.77.4708. URL: https://link.aps.org/doi/10.1103/PhysRevLett.77.4708.

[21] Tilman Plehn Martin Bauer. "Yet Another Introduction to Dark Matter". In: Springer Cham, 2019.

[22] Esra Bulbul et al. "DETECTION OF AN UNIDENTIFIED EMISSION LINE IN THE STACKED X-RAY SPECTRUM OF GALAXY CLUSTERS". In: *The Astrophysical Journal* 789.1 (2014). ISSN: 1538-4357. DOI: 10.1088/0004-637x/789/1/13. URL: http://dx.doi.org/10.1088/0004-637X/789/1/13.

[23] Susanne Mertens et al. "A novel detector system for KATRIN to search for keV-scale sterile neutrinos". In: *Journal of Physics G: Nuclear and Particle Physics* 46.6 (2019), p. 065203. DOI: 10.1088/1361-6471/ab12fe. URL: https://dx.doi.org/10.1088/1361-6471/ab12fe.

[24] KATRIN Collaboration. *KATRIN design report 2004*. Tech. rep. 51.54.01; LK 01. Forschungszentrum Jülich, 2005. 245 pp. DOI: 10.5445/IR/270060419.

[25] Leonard Köllenberger. "Neutrinos wiegen höchstens 0,8 Elektronenvolt". In: *KIT Presseinformation 012/2022* (2022). URL: https://www.kit.edu/kit/pi_2022_012_neutrinos-wiegen-hoechstens-0-8-elektronenvolt.php.

[26] Karen Hugenberg. "Design of the electrode system for the KATRIN main spectrometer". en. PhD thesis. Westfälische Wilhelms-Universität Münster, 2008. URL: https://www.uni-muenster.de/Physik.KP/AGWeinheimer/theses/Diplom_Karen_Hugenberg.pdf.

[27] F M Fränkle et al. "Penning discharge in the KATRIN pre-spectrometer". In: *Journal of Instrumentation* 9.07 (2014), P07028. DOI: 10.1088/1748-0221/9/07/P07028. URL: https://dx.doi.org/10.1088/1748-0221/9/07/P07028.

[28] J.F. Amsbaugh et al. "Focal-plane detector system for the KATRIN experiment". In: *Nuclear Instruments and Methods in Physics Research Section A: Accelerators, Spectrometers, Detectors and Associated Equipment* 778 (2015), pp. 40–60. ISSN: 0168-9002. DOI: https://doi.org/10.1016/j.nima.2014.12.116. URL: https://www.sciencedirect.com/science/article/pii/S0168900215000236.

[29] Tim Brunst. "First generation prototype detectors for the TRISTAN project". en. PhD thesis. Technische Universität München, 2020. URL: https://mediatum.ub.tum.de/?id=1540377.

[30] M. Aker et al. *Search for keV-scale Sterile Neutrinos with first KATRIN Data*. 2022. arXiv: 2207.06337 [nucl-ex]. URL: https://arxiv.org/abs/2207.06337.

[31] S Mertens et al. "Characterization of silicon drift detectors with electrons for the TRISTAN project". In: *Journal of Physics G: Nuclear and Particle Physics* 48.1 (2020), p. 015008. DOI: 10.1088/1361-6471/abc2dc. URL: https://dx.doi.org/10.1088/1361-6471/abc2dc.

[32] Siegmann Daniel. "Investigation of the Detector Response to Electrons of the TRISTAN Prototype Detectors". Master's thesis. Technische Universität München, 2019.

[33] G. F. Knoll. *Radiation Detection and Measurement*. ISBN: 9780470131480. URL: https://www.wiley.com/en-us/Radiation+Detection+and+Measurement%2C+4th+Edition-p-9780470131480.

[34] Frank Hartmann. *Evolution of Silicon Sensor Technology in Particle Physics*. ISBN: 9783319644349. URL: https://doi.org/10.1007/978-3-319-64436-3.

[35] M. Riordan and L. Hoddeson. "The origins of the pn junction". In: *IEEE Spectrum* 34.6 (1997), pp. 46–51. DOI: 10.1109/6.591664.

[36] Emilio Gatti and Pavel Rehak. "Semiconductor drift chamber — An application of a novel charge transport scheme". In: *Nuclear Instruments and Methods in Physics Research* 225.3 (1984), pp. 608–614. ISSN: 0167-5087. DOI: https://doi.org/10.1016/0167-5087(84)90113-3. URL: https://www.sciencedirect.com/science/article/pii/0167508784901133.

[37] Peter Lechner et al. "Silicon drift detectors for high resolution room temperature X-ray spectroscopy". In: *Nuclear Instruments and Methods in Physics Research Section A: Accelerators, Spectrometers, Detectors and Associated Equipment* 377.2 (1996). Proceedings of the Seventh European Symposium on Semiconductor, pp. 346–351. ISSN: 0168-9002. DOI: https://doi.org/10.1016/0168-9002(96)00210-0. URL: https://www.sciencedirect.com/science/article/pii/0168900296002100.

[38] TRISTAN group. "Conceptual Design Report: KATRIN with TRISTAN modules". In: (2022). URL: https://www.katrin.kit.edu/downloads/TRISTAN_Technical_Design_Report%20(10).pdf.

[39] D Siegmann et al. "Development of a silicon drift detector array to search for keV-scale sterile neutrinos with the KATRIN experiment". In: *Journal of Physics G: Nuclear and Particle Physics* 51.8 (2024). ISSN: 1361-6471. DOI: 10.1088/1361-6471/ad4bf8. URL: http://dx.doi.org/10.1088/1361-6471/ad4bf8.

[40] Marc Korzeczek. "Sterile neutrino search with KATRIN - modeling and design-criteria of a novel detector system". 51.03.02; LK 01. PhD thesis. Karlsruher Institut für Technologie (KIT), 2020. 167 pp. DOI: 10.5445/IR/1000120634.

[41] Matteo Gugiatti. "Development of a Large-matrix SDD-based Radiation Detector for Beta-decay Spectroscopy in Neutrino Physics". PhD Thesis. Politecnico Milano, 2022.

[42] A Nava et al. "A Geant4-based model for the TRISTAN detector". In: *Journal of Physics: Conference Series* 2156.1 (2021), p. 012177. DOI: 10.1088/1742-6596/2156/1/012177. URL: https://dx.doi.org/10.1088/1742-6596/2156/1/012177.

[43] Meatteo Biassoni et al. "Electron spectrometry with Silicon drift detectors: a GEANT4 based method or detector response reconstruction". In: *The European Physical Journal Plus* 136.125 (2021). DOI: 10.1140/epjp/s13360-021-01074-y. URL: https://doi.org/10.1140/epjp/s13360-021-01074-y.

[44] S.Y.F. Chu; L.P. Ekström and R.B. Firestone. *The Lund/LBNL Nuclear Data Search*. URL: http://nucleardata.nuclear.lu.se/toi/index.asp.

[45] Spreng Daniela. "Electron Backscattering on Silicon Drift Detectors and Its Impact on a Sterile Neutrino Search with KATRIN". Master's thesis. Technische Universität München, 2023.

[46] Pahlke Andreas. "Influence of oxide quality on the stability of semiconductor detectors under X-ray irradiation". PhD thesis. Technical University of Munich (TUM), 2004.

[47] R. Wunstorf et al. "Damage-induced surface effects in silicon detectors". In: *Nuclear Instruments and Methods in Physics Research Section A: Accelerators, Spectrometers, Detectors and Associated Equipment* 377.2 (1996). Proceedings of the Seventh European Symposium on Semiconductor, pp. 290–297. ISSN: 0168-9002. DOI: https://doi.org/10.1016/0168-9002(96)00218-5. URL: https://www.sciencedirect.com/science/article/pii/0168900296002185.

[48] W. Füssel et al. "Defects at the Si/SiO2 interface: Their nature and behaviour in technological processes and stress". In: *Nuclear Instruments and Methods in Physics Research Section A: Accelerators, Spectrometers, Detectors and Associated Equipment* 377.2 (1996), pp. 177–183. ISSN: 0168-9002. DOI: https://doi.org/10.1016/0168-9002(96)00205-7. URL: https://www.sciencedirect.com/science/article/pii/0168900296002057.

[49] Krzysztof Iniewski. "Radiation Effects in Semiconductors". In: 2016. ISBN: 978-1-4398-2694-2.

[50] F.M. Li, N. O, and A. Nathan. "Degradation behavior and damage mechanisms of CCD image sensor with deep-UV laser radiation". In: *IEEE Transactions on Electron Devices* 51.12 (2004), pp. 2229–2236. DOI: 10.1109/TED.2004.839758.

[51] Edward H. Nicollian and John Brews. "Mos (Metal Oxide Semiconductor) Physics and Technology". In: 1982. URL: https://api.semanticscholar.org/CorpusID:108930934.

[52] D. J. DiMaria. "Defect generation under substrate-hot-electron injection into ultrathin silicon dioxide layers". In: *Journal of Applied Physics* 86.4 (1999), pp. 2100–2109. ISSN: 0021-8979. DOI: 10.1063/1.371016. eprint: https://pubs.aip.org/aip/jap/article-pdf/86/4/2100/19176568/2100_1_online.pdf. URL: https://doi.org/10.1063/1.371016.

[53] Paolo Trigilio et al. "ETTORE: a 12-Channel Front-End ASIC for SDDs with Integrated JFET". In: *2018 IEEE Nuclear Science Symposium and Medical Imaging Conference Proceedings (NSS/MIC)*. 2018. DOI: 10.1109/NSSMIC.2018.8824675.

[54] Siegmann Daniel. "Development of the TRISTAN Silicon Drift Detector Modules for the keV sterile Neutrino Search with the KATRIN Experiment". PhD Thesis. Technische Universität München, 2024.

[55] CAEN. *V2740 64 Channel 16 bit 125 MS/s Digitizer*. URL: https://www.caen.it/products/v2740/.

[56] Huo Junde. "Nuclear Data Sheets for A = 55". In: *Nuclear Data Sheets* 109.4 (2008), pp. 787–942. ISSN: 0090-3752. DOI: https://doi.org/10.1016/j.nds.2008.03.001. URL: https://www.sciencedirect.com/science/article/pii/S0090375208000197.

[57] Munawar Iqbal and Fazal-e-Aleem. "Theory And Design Of Thermionic Electron Beam Guns". In: *AIP Conference Proceedings* 748.1 (2005), pp. 376–386. ISSN: 0094-243X. DOI: 10.1063/1.1896511. eprint: https://pubs.aip.org/aip/acp/article-pdf/748/1/376/11780735/376_1_online.pdf. URL: https://doi.org/10.1063/1.1896511.

[58] K. Urban et al. "A thermionic electron gun to characterize silicon drift detectors with electrons". In: *Journal of Instrumentation* 19.06 (2024), P06004. DOI: 10.1088/1748-0221/19/06/P06004. URL: https://dx.doi.org/10.1088/1748-0221/19/06/P06004.

[59] W. M. Haynes. In: *CRC Handbook of Chemistry and Physics*. Vol. 95th edition. 2014. ISBN: 978-1-4822-0868-9.

[60] Fatemeh Akbari. "A comprehensive open-access database of electron backscattering coefficients for energies ranging from 0.1 keV to 15 MeV". In: *Medical Physics* 50.9 (2023), pp. 5920–5929. DOI: https://doi.org/10.1002/mp.16604. eprint: https://aapm.onlinelibrary.wiley.com/doi/pdf/10.1002/mp.16604. URL: https://aapm.onlinelibrary.wiley.com/doi/abs/10.1002/mp.16604.

List of Figures

List of Tables

Acknowledgements

I want to thank everyone who supported me during my master's thesis, especially:

- **Prof. Dr. Susanne Mertens:** Thank you for the opportunity to work on this interesting topic within your group. Your organized and supportive way of leading this group creates a positive working atmosphere that was a pleasure to work in. I am especially grateful for your encouragement and for helping me to recognize my strengths as a physicist.

- **Korbinian Urban:** Thank you for your great support as my supervisor. I was always amazed by your ability to answer any of my questions on the spot and down to the last detail. I learned a great deal from you over this past year, and every time you helped me in the lab, I made major progress.

- **Daniel Siegmann:** Thank you for your encouraging words throughout the year. You have a great sense of people and always knew how to calm my nerves. Your intuitive understanding and explanation of physics are remarkable and made complex topics more approachable and intuitive for me, too.

- **Daniela Spreng and Christian Forstner:** Thank you for being my go-to persons for many questions in the lab and with my code. Even if you were deeply covered in your own work, you took the time to help me out, and I truly appreciate this!

- **Markus Kandler:** Thank you for making my start in this group so easy. You were the best office colleague with great taste in music, and our chats in the office always made the days fly by.

- **The whole E47 Working Group:** Thank you all for being such fun and supportive colleagues. I really enjoyed my time with each of you!

- **My Family:** Thank you for both your emotional and financial support throughout my studies. It would not have been possible without you!